Scilight

*Physical Models and Application*
https://www.sciltp.com/journals/pma



*Article*

# Collective Spatiotemporal Wave Patterns in Complex Neuronal Networks under External Modulation and Implications for Brain Function

Arthur Brice Azangue [1,*], Elie Bertrand Megam Ngouonkadi [2,†], Cédric Talonang Noufozo [1,†], Theophile Fonzin Fozin [3,†], Zeric Tabekoueng Njitacke [2,†] and Hilaire Bertrand Fotsin [1,†]

[1] Department of Physics, University of Dschang, Dschang P.O. Box 96, Cameroon
[2] Department of Electrical and Electronic Engineering, College of Technology (COT), University of Buea, Buea P.O. Box 63, Cameroon
[3] Department of Telecommunication and Computer Engineering, National Polytechnic School, University of Douala, Douala P.O. Box 2701, Cameroon
* Correspondence: azangue.bricearthur@gmail.com; Tel.: (+237)-675-86-06-34
† These authors contributed equally to this work.

**How To Cite**: Azangue, A.B.; Megam Ngouonkadi, E.B.; Talonang Noufozo, C.; et al. Collective Spatiotemporal Wave Patterns in Complex Neuronal Networks under External Modulation and Implications for Brain Function. *Physical Models and Application* **2026**, *1*(1), 4.

Received: 19 September 2026
Revised: 29 October 2026
Accepted: 3 November 2026
Published: 26 November 2026

**Abstract:** Spatiotemporal wave patterns are fundamental to computational neurosciences, coordinating activities across cortical regions during perception, memory, and motor control. Their disruption underlies a broad spectrum of neurological disorders. Wave propagation across cortical regions is thought to modulate neuronal sensitivity to external stimuli. This paper investigates the generation and spatiotemporal propagation of collective wave patterns in a complex neuronal network composed of $200 \times 200$ extended Hindmarsh-Rose (*eHR*) neurons coupled through hybrid synapse under electromagnetic radiation (*EMR*). By systematically varying synaptic coupling strengths and modulation parameters, we identify four major dynamical regimes: traveling waves, spiral waves, concentric target waves, and chimera states. These patterns are rigorously characterized using phase gradient analysis, winding numbers, local order parameters, Electroencephalogram (*EEG*) signal reconstruction, Phase Locking Value (*PLV*), Transfer Entropy (*TE*), and an octagonal symmetry index ($D_8$). Many works have individually reported spiral waves, chimera states, or target waves in neuronal networks under electromagnetic induction. There give a systematic comparison of found patterns within a single two-dimensional lattice with hybrid electrical–chemical coupling. We demonstrate that an architecture of three mutually coupled networks, with two receiving external sinusoidal stimulation, reproduces brain-like inter-regional synchronization and directional information flow. We show how coupling composition, lattice geometry, and external modulation shape collective dynamics in the present computational model. Some of the resulting wave regimes are qualitatively reminiscent of patterns reported in experimental neuroscience. Also, the frequency and amplitude of the external stimulation can change the apparent direction of information flow between the hub and the peripheral networks. However, the present simulations do not directly model cognition, sleep, epilepsy, or neurodegenerative diseases which will be done in the future works.

**Keywords:** collective patterns; hybrid coupling; *EEG*-like population signal responses; electromagnetic radiation

**Copyright:** © 2026 by the authors. This is an open access article under the terms and conditions of the Creative Commons Attribution (CC BY) license (https://creativecommons.org/licenses/by/4.0/).
**Publisher's Note:** Scilight stays neutral with regard to jurisdictional claims in published maps and institutional affiliations.

## 1. Introduction

One of the central preoccupations of modern neuroscience is to understand how different brain regions communicate to coordinate complex cognitive and sensory motor functions. Multichannel recording technologies including multi-electrode arrays, electrocorticography (*ECoG*), voltage-sensitive dye imaging, magnetoencephalography (*MEG*), and high-density electroencephalography (*EEG*) have established that the brain is not a stationary organ but a dynamical system which continuously produces rich spatiotemporal patterns of activity through synaptic plasticities and network interactions [1,2]. Among these activities, propagating waves are thought to support neural communication. They are spatially organized patterns in which peaks and troughs of oscillatory activity travel across the cortex [3,4]. These waves can be spontaneously generated by recurrent synaptic circuits or evoked by external stimuli, and they can travel across brain networks at multiple scales, transiently modulating neuronal excitability and information routing [1,5]. Experimental findings have revealed traveling waves at single cortical area (mesoscopic) scales and at whole-brain (macroscopic) scales. These observations have guided the development of theoretical frameworks for understanding wave generation in recurrent networks [6,7]. A landmark example is the motor cortex of monkeys, where Rubino et al. [8] demonstrated that *beta*-band oscillations ($\approx [12-30]$ Hz) during motor preparation propagate as planar traveling waves across the motor cortex, encoding information the timing and target of the upcoming reach in the latency and amplitude of the evoked response. Subsequent studies confirmed similar traveling wave patterns in the human motor cortex [9], and showed that the topology of large-scale structural connectivity directly shapes the frequency and spatial organization of these waves [10]. In the hippocampus, *theta*-oscillations ($\approx [4-8]$ Hz) are known to propagate as traveling waves along the spatio-temporal axis [11], where they are hypothesized to coordinate hippocampal-entorhinal circuits for the memory encoding, the long-term potentiation, and the spatial navigation [11,12]. At the macroscopic scale, traveling waves in the alpha-band have been shown to propagate as perceptual echoes across the human visual cortex [13–17], rotating and radial traveling waves have been documented during working memory and memory encoding in human intracranial recordings [18–20]. Collectively , these findings establish traveling waves as a canonical organizational feature of cortical dynamics, directly linking local synaptic interactions to macroscopic brain function.

Beyond their role in healthy cognition, the generation, coherence, and disruption of spatio-temporal wave patterns are intimately tied to a broad spectrum of neurological disorders, making their computational study directly relevant to clinical neuroscience. The alpha-band traveling waves observed in the visual cortex [13,14,16,21,22] are disrupted in visual processing disorders, while traveling waves in the *theta* and *gamma* bands support memory consolidation and are altered in amnesic conditions [23–28]. Motor wave propagation is impaired in Parkinson's disease, where abnormal *beta*-oscillations the same waves characterized by Rubino et al., are sustained beyond the preparation phase and fail to terminate at movement onset [29–35]. In epilepsy, ictal wavefronts [36] propagate as expanding, and in some cases rotating spiral, waves across cortical tissue [37–44]: computational models have shown that once spiral wave activity is established, the system may enter an indefinitely self-sustaining state analogous to status epilepticus, which ending by a globally synchronizing stimulus [44]. Disruption of inter-areal wave synchronization has been linked to the cognitive deficits of schizophrenia and Alzheimer's disease [45–52]. Roberts et al. [53] showed that during neuronal activity, spatiotemporal patterns are metastable, encompassing traveling waves, spiral waves, sources, and sinks coexisting within the same network a finding consistent with the functional heterogeneity of cortical circuits. Similarly, Gu et al. [54] demonstrated coherent spontaneous wave structures across species in both *fMRI* recordings from humans and *ECoG* from monkeys, revealing a conserved hierarchical cortical organization. These observations highlight that the full diversity of wave pattern types traveling, spiral, target, and chimera must be studied together to build a complete picture of healthy and pathological brain dynamics. The transition from single-cell firing patterns to the rich variety of population-level wave behaviors observed in vivo requires a network-scale analysis that accounts for the geometry of connectivity, the balance between excitatory and inhibitory coupling, and the influence of external fields and stimuli.

At the macroscopic level, the *EEG* provides the primary non-invasive window into collective neural oscillations. The amplitude and spectral content of the *EEG* signal directly reflect the degree of synchrony among neuronal populations. High amplitude of *EEG* signal characterizes highly synchronized states such as deep slow-wave sleep [55,56] and pathological hyper-synchrony in epileptic seizures [57–59]. Low amplitude of *EEG*, reflects the desynchronized, high-frequency activity of wakefulness and alert cognition [60,61], as well as the rapid-eye-movement (*REM*) sleep state [62,63]. In pathological conditions, very low or absent of *EEG* amplitude signals critical brain states such as coma or brain death [64–68]. Because *EEG* amplitude is determined by the summed postsynaptic potentials of large neuronal populations, it serves as a direct macroscopic readout of the spatiotemporal wave organization within the underlying network. Linking the microscopic dynamics of individual neurons and synapses as modeled computationally to the *EEG* signal therefore provides a critical bridge between theory and

clinical observation, and constitutes one of the key objectives of the present work. More recently, Haigh et al. [2] have conducted experimental study where they used real-time *EEG*-triggered transcranial magnetic stimulation (TMS) to test whether sensorimotor *mu* (8–13 Hz) and *beta* (14–30 Hz) traveling waves modulate motor-cortex excitability. The results show that neuronal excitability reflects the natural patterns of sensorimotor traveling waves, providing important evidence of traveling waves modulating neural excitability in humans and then opens possibilities for more effective stimulation protocols aligned with intrinsic brain dynamics. This investigation reveals the importance of wave propagation in the brain during specific stimulation.

Capturing these rich dynamics computationally requires biophysically realistic neuronal models capable of reproducing the full repertoire of spiking and bursting behaviors observed in real neurons. Hodgkin and Huxley (*HH*) described action potential generation in 1952 by modeling the propagation of ionic currents ($Na^+, K^+, Ca^{2+}$) across the cell membrane [69], and their framework inspired a family of successively more tractable models [70–73]. Among these, the Hindmarsh-Rose (*HR*) model and Extended Hindmarsh-Rose (*eHR*) model [72] have emerged as particularly versatile. Its three- and four-dimensional formulations reproduce quiescence, tonic spiking, periodic bursting, and chaotic dynamics with biological plausibility comparable to conductance-based models, while remaining computationally tractable for large-scale network simulation. Using synaptic coupling, neurons exchange information through hybrid synapse (combination of electrical and chemical synapses), enabling the construction of large networks with emergent collective dynamics. Within such networks, a broad range of collective behaviors has been identified and studied, including synchronization [74–80], chimera states [81–91], pattern formation [92–94], spiral waves [95–98], and target waves [98, 99]. The study of bifurcations and multi-stabilities under external stimuli particularly magnetic flux and electromagnetic induction has further revealed how external fields modulate these collective behaviors [92, 96, 100–103]. The detailed connection between wave patterns in computational models and experimentally observed brain rhythms has established computational neuroscience as an indispensable tool for interpreting the mechanistic basis of brain function [18, 53, 54, 104–106]. Several studies have already established that electromagnetic induction can generate or modulate spiral waves, chimera states, target waves, and other collective behaviors in neuronal networks. Studies based on FitzHugh–Nagumo, Hindmarsh–Rose, and related neuronal oscillators have demonstrated that electromagnetic feedback can modify synchronization thresholds, suppress or sustain spiral activity, and promote transitions between coherent and incoherent states. Therefore, the occurrence of spiral waves or chimera states under electromagnetic induction is not, by itself, the principal novelty of the present study.

A major motivation for the present study is the incorporation of electromagnetic radiation (*EMR*) as a physically and biologically realistic perturbation of neuronal dynamics, capable of providing a unified and quantitatively validated framework for comparing multiple wave regimes in the same hybrid-coupled neuronal architecture and extend this framework to interacting networks. In biological tissue, time-varying electromagnetic fields generated by the collective ionic currents of neighboring cells or imposed externally (as in transcranial magnetic stimulation, *TMS*) induce membrane currents that modulate neuronal excitability. When neurons under electromagnetic radiation are coupled in a network, this modulation propagates across nodes and generates complex interference patterns that, depending on the radiation intensity and the coupling architecture, favor different wave regimes. Following the work of Lv and Ma [100, 101], this effect is captured mathematically by adding a magnetic flux variable coupled to the membrane potential through a memristive flux variable coupled to the membrane potential equation [107], which introduces a history-dependent modulation of the neuronal firing threshold analogous to the memristor circuit element [108, 109]. Ma and Tang provided an important review demonstrating that electromagnetic induction is a key element explaining membrane potential dynamics and wave modulation in the brain [96]. Takembo et al. [110] investigated *EMR* effects in a chain network of FitzHugh-Nagumo (*FN*) neurons coupled through memristive synapses, finding that strong electromagnetic radiation accompanies wave propagation with turbulent electrical activity with direct implications for neurodegenerative manifestations under high radiation exposure. They further showed that a large extracellular potential induces electromagnetic induction currents during action potential propagation, modifying intercellular communication [111]. However, the *FN* model employed lacks the full spiking and bursting repertoire of biological neurons, and the synaptic connections considered are limited to purely memristive coupling, precluding a realistic treatment of chemical synaptic transmission. Palkar et al. [112] developed a one-dimensional spiking network to study wave reliability and control in cortical tissue, demonstrating that traveling waves enhance the sensitivity of cortical networks to stimuli and providing insight into seizure transitions. The present work differs primarily in its use of a two-dimensional *eHR* lattice, hybrid electrical–chemical coupling, electromagnetic feedback, and a three-networks interaction motif. In addition, these studies do not examine how wave propagation affects information exchange between coupled networks, which limits their relevance to disorders of inter-regional communication. Qin et al. [92] presented a two-layers network

model with electromagnetic induction and demonstrated generation of square target waves in each layer through field coupling but, only electrical synaptic coupling was considered. Despite these considerations, the existing literature remains fragmented in three respects. First, most studies focus on one pattern family or one coupling mechanism rather than comparing traveling, spiral, chimera, and target-wave regimes within the same model and parameter framework. Second, many electromagnetic-induction studies consider purely electrical, memristive, or phenomenological coupling, whereas the combined influence of electrical gap junctions and excitatory–inhibitory chemical transmission remains less systematically characterized in large two-dimensional extended Hindmarsh–Rose lattices. Third, comparatively little attention has been paid to whether spatial wave organization is preserved when several such networks interact and receive distinct external inputs. The present work addresses these specific gaps rather than claiming the first observation of the individual wave patterns.

The observed model dynamics are compared qualitatively with wave phenomena reported in neuronal recordings and previous computational studies. These comparisons are intended to motivate possible neurophysiological interpretations rather than to establish direct mechanisms of cognition or neurological disease. No disease-specific physiological parameters, clinical recordings, or behavioral variables are included in the present model. Four specific contributions are illustrated : First, we characterize the influence of external sinusoidal modulation on the dynamics of a single *eHR* neuron under *EMR*, demonstrating frequency-dependent transitions between bursting regimes with direct correspondence to brain rhythms (*theta*, *alpha*, *beta*, *gamma*). Second, we investigate pattern formation in a $200 \times 200$ two-dimensional network with hybrid synaptic coupling combining electrical gap junctions and chemical (excitatory and inhibitory) synapses and show that the relative dominance of these coupling types determines which wave regime emerges like traveling waves, concentric target waves, localized spiral waves, or chimera states; Third, we provide a rigorous quantitative characterization of each pattern type using a suite of metrics like phase gradient and phase velocity (traveling and target waves), winding number and phase singularity detection (spiral waves), local order parameter (chimera states), *EEG* amplitude and spectral analysis, Phase Locking Value , Transfer Entropy, and a novel octagonal symmetry index ($D_8$) that captures the eight-fold anisotropic propagation geometry emerging from the network lattice. Fourth, we extend the analysis to an architecture of three mutually coupled networks where two peripheral networks receiving external sinusoidal stimulation drive a central hub and find that this configuration reproduces key signatures of large-scale brain network synchronization, including stable inter-regional phase locking, directional information flow, and high *EEG* coherence consistent with *fMRI*-derived functional connectivity [113]. Together, these results establish a unified framework linking neuronal-scale biophysics to macroscopic observables, with broad implications for understanding information processing, neural synchronization, and neurological disorders.

The remainder of this paper is organized as follows. Section 2 introduces the *eHR* neuron model under electromagnetic radiation and describes the network architecture, synaptic coupling equations, and numerical integration method. Section 3 analyzes the membrane potential dynamics of a single eHR neuron under external sinusoidal modulation at varying frequencies. Section 4 presents results on pattern formation and wave propagation in the single hybrid-coupled $200 \times 200$ network, with quantitative characterization of each observed pattern type. Section 5 extends the analysis to the three-network interacting architecture and investigates inter-network synchronization and information flow. Section 6 provides a discussion of the results in the context of brain function and neuroscience and in Section 7, a conclusion. Derivations of the hybrid synaptic current expressions, the eight-fold spatial symmetry condition, and other key quantitative metrics are provided in Appendix A–Appendix C.

## 2. Neuronal Model under Electromagnetic Radiation (EMR)

The computational neuroscience literature encompasses a wide range of oscillator models capable of reproducing the spiking and bursting dynamics of real neurons. Among all these neuronal models, the extended Hindmarsh-Rose *eHR* oscillator exhibits strong biological plausibility, as its formulation reproduces quiescence, tonic spiking, periodic bursting, and deterministic chaos behaviors characteristic of real cortical neurons. *EMR* is incorporated into the dynamics of *eHR* neuron to observe waves modulation of membrane potential of neuron and a new mathematical model is given by Equation (1).

$$\begin{cases} \dot{x} = ay + bx^2 - cx^3 - dz + I + m(x, \phi, t) + I_{mod}(t), \\ \dot{y} = e - fx^2 - y - gw, \\ \dot{z} = \mu[-z + s(x + h)], \\ \dot{w} = \upsilon[-k_w w + r(y + l)], \\ \dot{\phi} = k_\phi x - k_2 \phi, \end{cases} \tag{1}$$

where $x$ is membrane potential of neuron, $y$ describes fast currents, $z$ describes slow currents and $w$ is a slower dynamical variable representing calcium exchange between the intracellular store (endoplasmic reticulum) and the cytoplasm which is important to produce chaotic behaviors like in the case of stomatogastric ganglion neurons [69]. The fifth equation is associated to magnetic flux ($\phi$) defined in a function $m(x, \phi, t) = -k_1 x(\alpha + \beta\phi^2)$. Additional explanations of *EMR* are indicated in [101,114]. Parameter $k_1$ is feedback gain. The term $kx$ describes membrane potential induced changes on magnet flux and the term $k_2\phi$, the leakage of magnet flux. Parameter $I_{mod}(t)$ is periodic external modulating input applied on the membrane of neuron. Parameter $I_{mod}(t)$ is defined by a sinusoidal function with an amplitude $A$ and a frequency $\omega$. The *eHR* parameters are defined as follows : $a = 1.0$ S, $b = 3.0\ (\mathrm{mV})^{-1}$, $c = 1.0\ (\mathrm{mV})^{-2}$, $d = 0.99$ S, $e = 1.01$ mV, $f = 5.0128\ (\mathrm{mV})^{-1}$, $s = 3.966$, $h = 1.605$ mV, $l = 1.619$ mV, $\mu = 0.00215$, $\upsilon = 0.0009$, $g = 0.0278$ S, $r = 3.0$, $k_w = 0.9573$ and $I$ is an external current in mA. For MR, $\alpha = 0.1$, $\beta = 0.02$, $k_\phi = 0.9$, $k_1 = 1.0$ and $k_2 = 0.5$. The numerical integration uses fourth order Runge Kutta algorithm (*RK4*) with a time step of $0.01$. The number of iterations is $T/step$ where $T$ is the maximum time for each simulation. The initial conditions are taken randomly (because we assume that all nodes inside network cannot have same initial spatial configuration) all less than $0.1$ for all variables of Ordinary Differential Equations (*ODEs*) of Equation (1). All simulations were performed using *MATLAB* version 2020a. Results were verified across 5 independent simulations with different random initial conditions of Equation (1). Parameters were explored systematically over the ranges: $g_E \in [0.01, 4.0]$, $g_C \in [0.01, 6.0]$, $g_C \in [0.01, 6.0]$, $\omega \in [10^{-6}, 10^{-1}]$, and $\omega \in [10^{-6}, 10^{-1}]\ \mathrm{rad(ms)}^{-1}$. The 80:20 distribution of excitatory-inhibitory coupling is implemented numerically using $g_C^{\mathrm{exc}} = 0.8g_C$, and $g_C^{\mathrm{inh}} = 0.2g_C$. The number of iterations is $\frac{Total\ time}{timestep}$, with timestep ($\Delta t$) = 0.01. For $t_{max} = 200$ ms , we have 20,000 iterations and for $t_{max} = 5000$ ms we have 500,000 iterations. Sampling frequency 100 KHz unilateral, single-sided power spectrum.

## 3. Membrane Potential Dynamics of Neuron under External Sinusoidal Modulation

An external modulation signal is now injected inside membrane potential through a sinusoidal function defined by $I_{mod}(t) = A\cos(\omega t)$ (mA). Parameters $A$ (in mA) and $\omega$ (in $\mathrm{rad(ms)}^{-1}$) are amplitude and frequency of modulation signal respectively. Figure 1 illustrates dynamics of membrane potential before and after modulation and the detected spike times. Figure 2 shows the applied sinusoidal current together with the instantaneous neuronal phase, and Figure 3 presents the corresponding normalized membrane-potential power spectra. In Figures 1–3, panels (a–c) correspond to stimulus onset at $t_{\mathrm{on}} = 1500$ ms, whereas panels (d–f) correspond to $t_{\mathrm{on}} = 2500$ ms. The forcing frequencies are $\omega = 10^{-1}$, $10^{-2}$, and $10^{-5}\ \mathrm{rad(ms^{-1})}$ for panels (a, d), (b, e), and (c, f), respectively. Because the simulation time is expressed in milliseconds, the physical stimulus frequency is obtained from $f_{\mathrm{stim}} = \frac{1000\omega}{2\pi}$.

The three frequencies therefore correspond to 15.915, 1.592, and $1.592 \times 10^{-3}$ Hz. Before stimulus onset, the membrane-potential traces in Figure 1 display irregular bursting, characterized by groups of rapid spikes separated by comparatively long hyperpolarized intervals. The external input produces qualitatively different post-stimulus responses depending on its temporal scale:

- $\omega = 10^{-5}\ \mathrm{rad(ms)}^{-1}$ at $t_{\mathrm{on}} = 1500$ ms: For $\omega = 10^{-5}\ \mathrm{rad(ms)}^{-1}$, the stimulus frequency is only $1.592 \times 10^{-3}$ Hz and its period is approximately 628.3 s. The post-stimulus interval in Figure 1c contains only 0.00398 cycle. The applied sinusoidal current is therefore effectively constant over the displayed time interval. Following stimulus onset, Figure 1c shows an initial high-amplitude transient followed by sustained rapid neuronal firing. The amplitude envelope progressively relaxes toward a more stationary state, while the mean firing rate reaches approximately 117.20 spikes/second. Because the stimulus does not complete a measurable fraction of a cycle, this rapid activity cannot be interpreted as entrainment to the ultra slow forcing frequency. This interpretation is confirmed by Figure 2c, where the input remains almost constant while the instantaneous neuronal phase continues to evolve rapidly. Figure 3c displays a dominant output frequency of approximately 98.8 Hz, together with a secondary component close to 200 Hz. The latter is consistent with a harmonic of the rapid non-sinusoidal spiking waveform. The large separation between the input frequency and the dominant response frequency demonstrates that Figure 1c represents intrinsic fast neuronal activity induced by a quasi-static current shift rather than stimulus-frequency locking.
- $\omega = 10^{-1}\ \mathrm{rad(ms)}^{-1}$ at $t_{\mathrm{on}} = 2500$ ms: Figure 1d examines whether the response to the highest forcing frequency depends on the stimulus-onset time. Before $t_{\mathrm{on}} = 2500$ ms, the neuron undergoes a longer interval of spontaneous irregular bursting. After activation, the response again becomes periodically organized, with a mean firing rate of approximately 80.67 spikes/second. Figure 2d contains approximately 23.87 forcing cycles. Despite the shorter post-stimulus interval and the different neuronal state at stimulus onset, the phase dynamics remain regularly organized relative to the input. In Figure 3d, the dominant frequency is again approximately 16.02 Hz and is nearly superimposed on the applied frequency of 15.915 Hz. The agreement

between Figure 1a,d, between Figure 2a,d, between Figure 3a,d demonstrates that the forcing-locked response at $\omega = 0.1\ \mathrm{rad(ms)}^{-1}$ is reproducible for the two investigated onset times. The firing rates differ by only approximately (1.3%), while the same dominant frequency is recovered in both spectral analyses. This condition therefore provides the most robust evidence of externally organized neuronal dynamics.

- $\omega = 10^{-2}\ \mathrm{rad(ms)}^{-1}$ at $t_{\mathrm{on}} = 2500$ ms: For the later onset time, the interval between 2500 ms and 4000 ms contains only 2.39 cycle of the 1.592 Hz stimulus. Figure 1e consequently represents the response to a slowly varying segment of the external current rather than to several repetitions of a periodic stimulus. The observed post-stimulus transition may depend on both the instantaneous state of the neuron at $t_{\mathrm{on}} = 2500$ ms and the local amplitude and slope of the slowly varying input. Figure 2e should show the input beginning at its maximum value and decreasing gradually without completing even one quarter of a full oscillation. The associated phase evolution describes the rapid neuronal activity developed during this slow change of current, but it cannot establish a stable phase relationship with a periodic forcing signal. The 1.5 s post-stimulus window gives a nominal spectral resolution of approximately 0.667 Hz, which is more than four times the imposed frequency. Consequently, Figure 3e cannot resolve a spectral peak at 0.1592 Hz. Figures 1e, 2e, and 3e should therefore be interpreted as characterizing an onset-dependent transient response to slow modulation. A demonstration of entrainment at this frequency would require substantially longer simulations containing multiple complete forcing cycles.
- $\omega = 10^{-5}\ \mathrm{rad(ms)}^{-1}$ at $t_{\mathrm{on}} = 2500$ ms: In Figure 1f, the post-stimulus interval contains only 0.00239 cycle of the ultra slow input. As in Figure 1c, the stimulation is effectively equivalent to a quasi-static current shift. After an initial transient, the neuron develops rapid sustained firing, with a mean firing rate of approximately 130.67 spikes/second. Figure 2f confirms that the applied input changes negligibly between 2500 ms and 4000 ms, whereas the instantaneous neuronal phase evolves on a much shorter time scale. Figure 3f shows a dominant membrane-potential frequency of approximately 105.28 Hz. This frequency is not related to the ultra slow input frequency and instead characterizes the intrinsic fast neuronal response under the modified current level. The difference between the dominant frequencies in Figures 3c,f, approximately 98.8 Hz and 105.28 Hz, and between their firing rates, approximately 117.20 and 130.67 spikes/second, indicates sensitivity to the neuronal state at stimulus onset, the duration of the post-stimulus window, and the contribution of the initial transient. These variations show that the quasi-static condition is less onset-independent than the forcing-locked response obtained at $\omega = 10^{-1}\ \mathrm{rad(ms)}^{-1}$.

The joint analysis of Figures 1–3 identifies three different response regimes. At $\omega = 10^{-1}\ \mathrm{rad(ms)}^{-1}$, the temporal traces, phase evolution, and spectral peaks consistently indicate forcing-locked periodic bursting. At $\omega = 10^{-2}\ \mathrm{rad(ms)}^{-1}$, the available intervals contain less than one forcing cycle, and the results characterize a transient response to a slowly varying external current. At $\omega = 10^{-5}\ \mathrm{rad(ms)}^{-1}$, the stimulus is effectively quasi-static, while the neuron generates intrinsic fast spiking with dominant frequencies close to 100 Hz. The phase plots in Figure 2 provide qualitative information about the organization of the neuronal response. Similarly, because the spectra in Figure 3 are normalized independently, they permit comparison of peak frequencies but not direct comparison of absolute spectral powers across conditions. These results demonstrate that the neuronal response depends strongly on the temporal scale of the external modulation. Nevertheless, the present frequency set does not establish selective modulation of the canonical brain rhythms. Only the frequency of 15.915 Hz condition lies directly within one of these conventional ranges and demonstrates clear frequency locking. The slower conditions should instead be interpreted as slowly varying and quasi-static controls.

Specifically, this single-neuron response suggests that external periodic inputs, whether from thalamo-cortical feedback, sub-cortical drive, or transcranial alternating current stimulation (*tACS*), can selectively gate a neuronal population to resonate within specific frequency bands (*theta*, *alpha*, *beta*, or *gamma*) if these frequencies fall within the acceptable physiological bands [115–117]. Accordingly, references to memory encoding, visual attention, motor preparation, and sensory binding are treated here as literature-based contextual examples and not as cognitive functions directly reproduced by the present single-neuron simulation. Crucially, the neuron exhibits stable, self-sustained oscillations after stimulus onset (Figure 1), which is a dynamical property consistent with intrinsically generated neural oscillations observed in cortical networks as opposed to purely evoked responses. This single neuron result therefore establishes the biophysical substrate for the frequency selective propagation dynamics observed at the network level, in Sections 4 and 5.

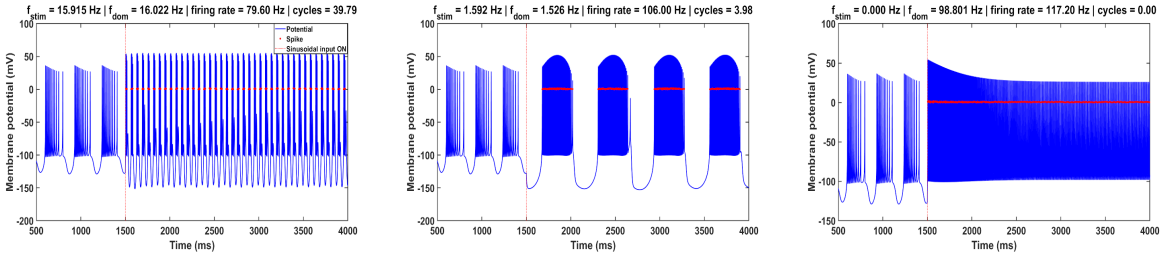


**(a)** $\omega = 10^{-1}$ rad(ms)$^{-1}$. **(b)** $\omega = 10^{-2}$ rad(ms)$^{-1}$. **(c)** $\omega = 10^{-5}$ rad(ms)$^{-1}$.

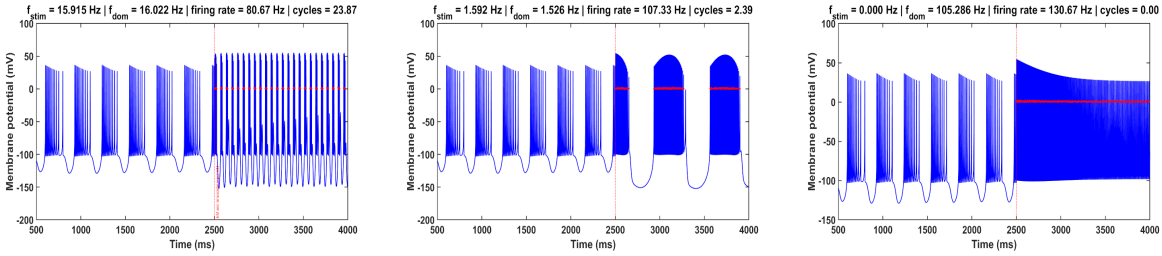


**(d)** $\omega = 10^{-1}$ rad(ms)$^{-1}$. **(e)** $\omega = 10^{-2}$ rad(ms)$^{-1}$. **(f)** $\omega = 10^{-5}$ rad(ms)$^{-1}$.

**Figure 1.** Membrane-potential dynamics of the isolated *eHR* neuron before and after the onset of external sinusoidal modulation. Panels (**a**–**c**) correspond to stimulus onset at $t_{\mathrm{on}} = 1500$ ms, and panels (**d**–**f**) correspond to $t_{\mathrm{on}} = 2500$ ms. The angular forcing frequencies are $\omega = 0.1$ rad(ms)$^{-1}$ in (**a**,**d**), $\omega = 0.01$ rad(ms)$^{-1}$ in (**b**,**e**), and $\omega = 10^{-5}$ rad(ms)$^{-1}$ in (**c**,**f**). The corresponding physical frequencies are 15.915, 0.1592, and $1.592 \times 10^{-3}$ Hz. The red dotted line indicates stimulus onset, while the red markers indicate the spike times used to estimate the mean firing rate. The modulation amplitude is $A = 2$ mA and the bias current is $I = 3.0249$ mA. The corresponding applied inputs, instantaneous phases, and membrane-potential spectra are presented in Figures 2 and 3.

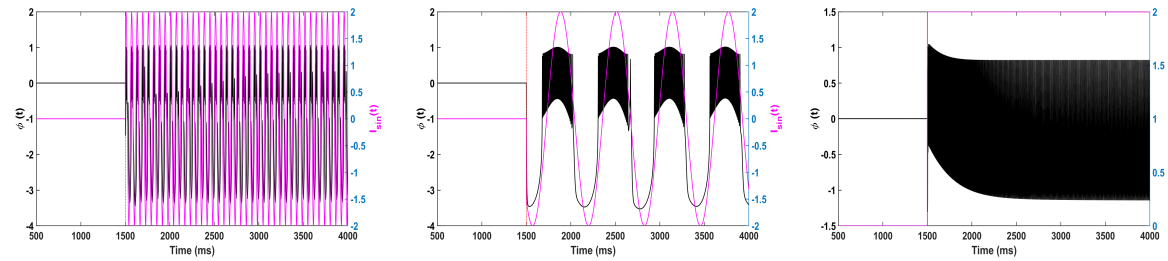


**(a)** $\omega = 10^{-1}$ rad(ms)$^{-1}$. **(b)** $\omega = 10^{-2}$ rad(ms)$^{-1}$. **(c)** $\omega = 10^{-5}$ rad(ms)$^{-1}$.

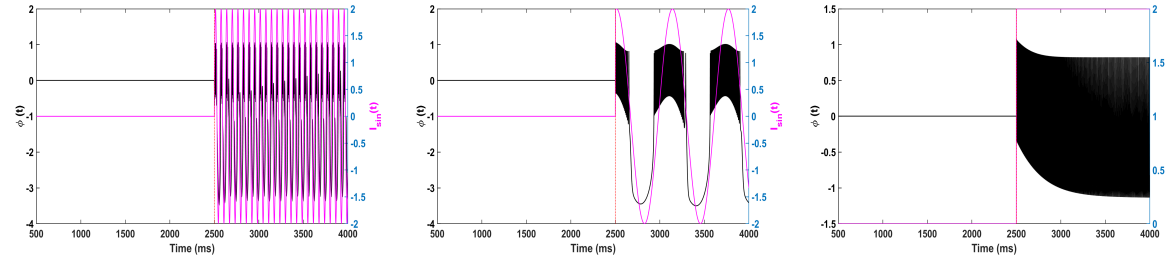


**(d)** $\omega = 10^{-1}$ rad(ms)$^{-1}$. **(e)** $\omega = 10^{-2}$ rad(ms)$^{-1}$. **(f)** $\omega = 10^{-5}$ rad(ms)$^{-1}$.

**Figure 2.** Applied sinusoidal input and instantaneous neuronal phase corresponding to the membrane-potential responses in Figure 1. Panels (**a**–**c**) correspond to $t_{\mathrm{on}} = 1500$ ms, and panels (**d**–**f**) correspond to $t_{\mathrm{on}} = 2500$ ms. The angular forcing frequencies are $\omega = 10^{-1}$, $10^{-2}$, and $10^{-5}$ rad(ms)$^{-1}$ for panels (**a**,**d**), (**b**,**e**), and (**c**,**f**), respectively. The magenta curves show the applied current $I_{\mathrm{mod}}(t)$, and the black curves show the instantaneous neuronal phase $\theta_x(t)$, obtained from the analytic representation of the membrane-potential signal. The red dotted line denotes stimulus onset. The intervals contain 39.79, 3.98, and 0.00398 forcing cycles in (**a**–**c**), and 23.87, 2.39, and 0.00239 cycles in (**d**–**f**), respectively.

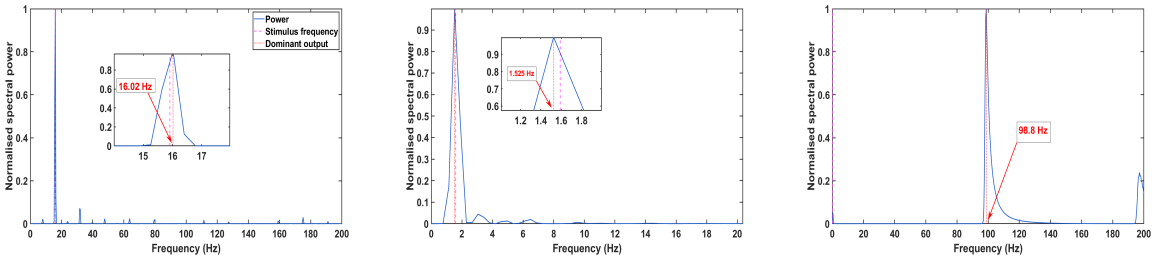


**(a)** $\omega = 10^{-1}$ rad(ms)$^{-1}$. **(b)** $\omega = 10^{-2}$ rad(ms)$^{-1}$. **(c)** $\omega = 10^{-5}$ rad(ms)$^{-1}$.

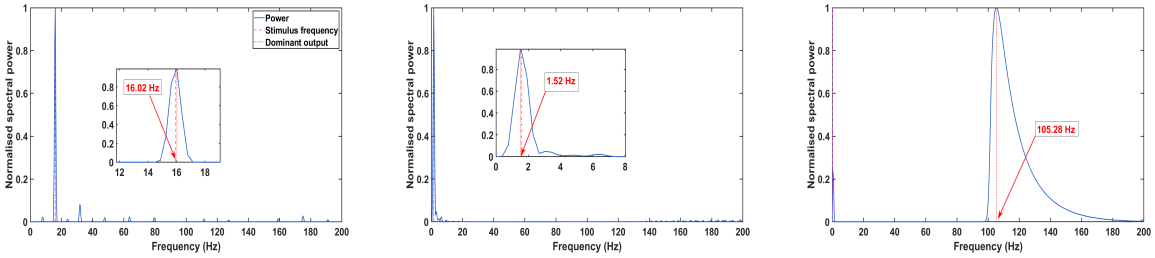


**(d)** $\omega = 10^{-1}$ rad(ms)$^{-1}$. **(e)** $\omega = 10^{-2}$ rad(ms)$^{-1}$. **(f)** $\omega = 10^{-5}$ rad(ms)$^{-1}$.

**Figure 3.** Normalized membrane-potential power spectra (in decibel (dB)) corresponding to the post-stimulus responses presented in Figure 1. Panels (**a–c**) correspond to stimulus onset at $t_{\text{on}} = 1500$ ms, and panels (**d–f**) correspond to $t_{\text{on}} = 2500$ ms. The magenta dashed lines indicate the applied stimulus frequencies, and the red dotted lines indicate the measured dominant output frequencies. For $\omega = 10^{-1}$ rad(ms)$^{-1}$, the dominant frequency is approximately 16.02 Hz for both onset times and closely matches the applied frequency of 15.915 Hz. For $\omega = 10^{-2}$ rad(ms)$^{-1}$, the available windows contain less than one forcing cycle and cannot resolve the applied frequency of 0.1592 Hz. For $\omega = 10^{-5}$ rad(ms)$^{-1}$, the dominant frequencies are approximately 98.8 and 105.28 Hz; these peaks characterize intrinsic fast neuronal firing under effectively quasi-static forcing and do not indicate entrainment to the ultra slow input. Spectral powers are normalized independently within each panel. Sampling frequency 100 KHz unilateral.

## 4. Patterns Formation and Waves Propagation in Hybrid Network

In Section 2, we introduced effect of *EMR* on *eHR* neuron showing how dynamics of membrane potential is affected under external stimuli. *EMR* systematically modulates neuronal excitability and thereby gates the frequency band and spatial organization of network waves. Let consider a layer made with a grid structure and indexing of nodes as described on Figure 4. Node $(i, j)$ at the center interacts with its four nearest neighbors through a hybrid connection comprising both electrical and chemical synapses, as indicated by the green dotted lines in Figure 4. The human brain contains roughly 86 billion neurons and on the order of $10^{14}$ synapses; we simulate $4 \times 10^4$ neurons (intra/inter connections) inside the network. However, for the computational analysis, a small fraction of this quantity is used. This consideration cannot generalized global dynamics but may significantly contribute to better understand functioning of some hidden areas of brain. A regular network is constructed by $200 \times 200$ nodes. Neurons are placed on nodes uniformly with nearest-neighbor connection, and no-flux boundaries conditions are applied. Electrical and chemical connections are defined by Equations (2) and (3) respectively.

$$I_{elect} = g_E\Big(x_{post}(t) - x_{pre}(t)\Big), \tag{2}$$

$$\begin{cases} I_{chem} = g_C R^{'}(t)\Big(E_{rev} - x_{post}(t)\Big) \\ and \\ \beta_e \frac{dR^{'}(t)}{dt} = \frac{R_\infty(x_{pre}(t)) - R^{'}(t)}{R_0 + R_\infty(x_{pre}(t))}, \end{cases} \tag{3}$$

with

$$R_\infty(x_{pre}) = \begin{cases} \tanh\Big(\frac{x_{pre} - x_{th}}{x_{slop}}\Big) & if \;\; x_{pre} > x_{th} \\ 0 & if \;\; x_{pre} \leq x_{th} \end{cases} \tag{4}$$

$x_{pre}(t)$ and $x_{post}(t)$ represent membrane potential of presynaptic and postsynaptic neuron respectively. In Equations (7) and (8), $x_{post}(t)$ is associated to node $x(i,j)$ while $x_{pre}(t)$ is associated to neighboring nodes in the grid. $g_E$ and $g_C$ are electrical and chemical synaptic coupling strengths respectively, $R^{'}(t)$ is scaled synaptic activation, $R_\infty(x)$ is a sigmoid function which represents steady-state synaptic activation defined in Equation (4) and $R_0$ a positive constant ($R_0 \geq 1$). $E_{rev}$ is reversal potential and is selected such that injected current is always negative for inhibitory synapses and positive for excitatory synapses. For analysis, we take $E_{rev} = -2$ for inhibitory synapses and $E_{rev} = 2$ for excitatory synapses. $\beta_e$ is neurotransmitter parameter. Other parameters are taken as $x_{th} = -0.8$ and $x_{slop} = 1.0$. Because cortical circuits contain both excitatory and inhibitory synapses, we split the chemical coupling as $g_C^{exc} = 0.8g_C$ and $g_C^{inh} = 0.2g_C$ [118–122]. This balance is crucial to maintain good functioning of the brain and nervous system because for biological neuron, inhibition is more important than excitation. Notice that the balance between $g_C^{exc}$ and $g_C^{inh}$ refers only to functional significance as considered in neuroscience and do not, by themselves, establish the relative functional influence of the two synaptic pathways. Predominance of excitation over inhibition in neuronal networks reflects the need for stability (preventing over-excitation), precision, and efficient processing in brain's complex and dynamic systems. However this balance may weakly change depending on the brain behavior such as in presence of some neuronal diseases [121–130]. Hence, for our analysis we set $g_C = g_C^{inh} + g_C^{exc}$, because both inhibitory and excitatory behavior are necessary during chemical exchanges and held modeling chemical balance of neuron. Equation (5) presents mathematical model of a network in a grid field with *EMR*. Parameters $I_{mod}(t)$ and $I_{hyb}(i,j)$ are respectively external stimulation and a combination of electrical and chemical junctions.

$$\dot{X}_{(i,j)} = F(X_{(i,j)}, t) + I_{mod}(t) + I_{hyb}(i,j), \tag{5}$$

with the vector field $F$

$$\mathbf{F}(\mathbf{X}) = \begin{pmatrix} ay + bx^2 - cx^3 - dz + I - k_1 x(\alpha + \beta\phi^2) \\ e - fx^2 - y - gw \\ \mu[-z + s(x+h)] \\ \nu[-k_w w + r(y+l)] \\ k_\phi x - k_2 \phi \end{pmatrix},$$

and sigmoid function is

$$\dot{R}^{'}_{(i,j)} = \frac{1}{\beta_e} \frac{R_\infty(x_{(i,j)}) - R^{'}_{(i,j)}}{R_0 + R_\infty(x_{(i,j)})}, \tag{6}$$

where vector field is $X = (x, y, z, w, \phi)$, $F$ is associated to *ODEs* of Equation (1) and $I_{hyb}(i,j)$ of Equation (9) is the total contribution of electrical and chemical synaptic connection of network Figure 4 defined by Equations (7) and (8) respectively. Notice that both $I_{elect}(i,j)$ and $I_{chem}(i,j)$ combine postsynaptic neuron potential $x_{(i,j)}$ which is the central node in red color Figure 4, and presynaptic neurons $x_{(i+1,j)}$, $x_{(i-1,j)}$, $x_{(i,j+1)}$ and $x_{(i,j-1)}$ in blue color. For $I_{elect}(i,j)$, the coupling strength $g_E$ affected both on presynaptic and postsynaptic nodes, while for $I_{chem}(i,j)$, the coupling strength affect only the presynaptic neurons. This is because electrical connection is bidirectional while chemical connection is unidirectional, where transmission is from presynaptic to postsynaptic neighbors neurons (nodes blue in Figure 4). More details to obtain these Equations are given in Appendix A.

$$I_{elect}(i,j) = g_E\Big(x_{(i+1,j)} + x_{(i-1,j)} + x_{(i,j+1)} + x_{(i,j-1)} - 4x_{(i,j)}\Big), \tag{7}$$

$$\begin{aligned} I_{chem}(i,j) = R^{'}_{(i,j)}\Big[4\Big(g_C^{inh}E_{rev}^{inh} + g_C^{exc}E_{rev}^{exc}\Big) - \\ \Big(g_C^{inh} + g_C^{exc}\Big)\Big(x_{(i,j+1)} + x_{(i,j-1)} + x_{(i-1,j)} + x_{(i+1,j)}\Big)\Big], \end{aligned} \tag{8}$$

and

$$I_{hyb}(i,j) = I_{elect}(i,j) + I_{chem}(i,j). \tag{9}$$

Some key metrics are used to analyze global network dynamics modeled where more explanations of these

tools are given in Appendices. Electromagnetic radiation oscillates at the frequency of $\Omega_1$, which modulates the membrane potential through the memristive magnetic flux term $m(x, \phi, t)$, and Sinusoidal modulation at the frequency of $\Omega_2$, applied as $I_{mod}(t)$. By considering a neuron at a position $r_(i, j)$ in the lattice receiving the two periodic driving signals ( $\Omega_1$ and $\Omega_2$), the total forcing [131,132] $F_{(i,j)}$ at node $(i, j)$ is given in Equation (10).

$$F_{(i,j)}(t) = A_1 \cos(\Omega_1 t - k_1 \cdot r_{(i,j)}) + A_2 \cos(\Omega_2 t - k_2 \cdot r_{(i,j)}) + A_{\text{mix}} \cos((\Omega_2 - \Omega_1)t - (k_2 - k_1)), \quad (10)$$

where the third term arises from the mixing (memristive) nonlinearity inherent in the *EMR* coupling. For constructive interference to occur simultaneously along all eight propagation directions, the wavevectors $k_1$ and $k_2$ must satisfy the phase-matching condition $k_2 = 8k_1$ (modulo reciprocal lattice vectors). Since the lattice dispersion relation for small perturbations is approximately linear in the long-wavelength limit ($\Omega \propto \|k\|$), this phase-matching condition implies the ratio given in Equation (11).

$$\frac{\Omega_2}{\Omega_1} = \frac{\|k_2\|}{\|k_1\|} \approx 8. \quad (11)$$

Physically, this means that eight wavelengths of the high-frequency wave fit exactly into one wavelength of the low-frequency wave. The emergence of waves patterns follows specific rule. When several magnetically sensitive neurons are coupled together, the *EMR* acts as a control parameter that dictates how the neurons synchronize. Because the *EMR* effect adds a memory effect (like memristor) to every neuron, it prevents them from resetting instantly. This delay and modulation create complex interference patterns across the network. Depending of the intensity of the radiation and the type of coupling, several wave behaviors emerge. *Spiral Waves*: Instead of firing in unison, the neurons fire in a rotating spiral. *EMR* can effectively break or suppress these spirals, pushing the system from chaotic turbulence into a synchronized state. *Target Waves*: Concentric rings of activity radiating outward from a central pacemaker neuron. *EMR* modulation can change the frequency of these waves or cause the center to shift. *Chimera States*: A strange state where one part of the neural network is fully synchronized (firing together) while another physically identical part is completely incoherent (chaotic). *EMR* often triggers the transition into or out of these states. For a detailed analysis of these patterns, some key quantifiers are employed: The phase gradient and phase velocity for traveling waves, phase gradient and phase singularities (winding number) for spiral waves, phase gradient and phase velocity for target waves, and local order parameter for chimera. More information over these metrics are given in Appendix A.2.

We consider hybrid interaction ($I_{elect}(i, j) \neq 0$ and $I_{chem}(i, j) \neq 0$) of central node $(i, j)$ with neighboring nodes made with electrical (linear) coupling and chemical (non-linear) coupling. This interaction is more interesting because it takes into consideration both electrical and chemical synapse, more close to real biological synaptic neuronal cells behavior. Figure 5 illustrate snapshots of behavior of membrane potential inside the *(i,j)-grid*, where we observe a successive generation of different patterns in the layer over the time for constant values of $\omega = 10^{-6}$ $\text{rad(ms)}^{-1}$, $I$ = 2 mA and $g_E = 0.1$.

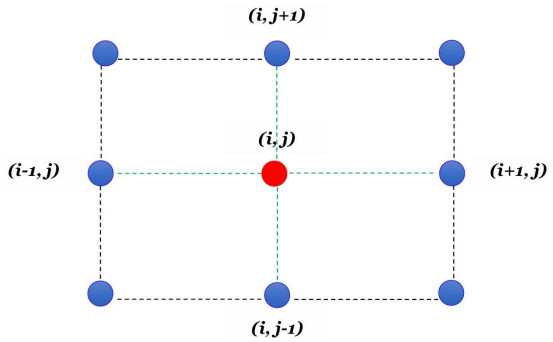


**Figure 4.** Scheme of network with a grid structure. Node $(i, j)$ in red color at center interacting with 4 neighbors nodes indicated in blue color.

From Figure 5a–f, we set $g_C = 1.5$ and from Figure 5g–l, we set and $g_C = 6$. The snapshots of the membrane-potential dynamics of Figure 5 reveal a progressive transition from traveling-wave turbulence to chimera-mediated self-organization and finally to coherent spiral-wave activity of neuronal activity across the network. Figures 6 and 7 illustrate some key metrics use to interpret patterns of Figure 5. At early times ($t$ = 10 ms to 100 ms) in Figure 5a,b,g,l the network exhibits fragmented propagating waves and turbulent islands reflecting weak synchronization and

multiple competing propagation fronts. That are similar to the distribute information processing observed in cortical traveling waves. During the intermediate stage ($t = 1000$ ms to $t = 2000$ ms) in Figure 5c,d,i,j, labyrinthine structures and vortices emerge, indicating strong interactions and the coexistence of coherent and incoherent domains characteristic of chimera states indicating that neuronal populations coexist in the network. At later times ($t = 3000$ ms to $t = 5000$ ms) in Figure 5e,f,k,l, these complex structures collapse into stable spiral waves organized around topological singularities with nonzero winding number, resulting in highly coordinated neuronal activity governed by a dominant topological attractor. At $t = 3000$ ms and 5000 ms display a comparable multispiral-wave morphology. This observation demonstrates the presence of multispiral structures at the two sampled late times, but it does not establish persistent topological-core dynamics throughout the interval $[3000 - 5000]$ ms. Accordingly, the state is classified as a late-time multispiral-wave morphology rather than as a persistent multispiral-wave regime. The simultaneous evolution of phase-gradient fields in Figures 6a and 7a, winding number in Figures 6b and 7b where at early state ($t$ = 10 ms), $n \approx 0$, at intermediate state ($t$ = 100 ms to 1000 ms) local fluctuations occur and spiral state $n \pm 1$ as observe a zooming area, chimera regions in Figures 6c and 7c where at early state we have large incoherent (majority area in red color) fraction, at intermediate state we observe mixed domains (balance between areas in red and blue color) and lather most neurons become coherent (majority area in blue color) except near the spiral core. Spiral-core detection in Figures 6d and 7d where at early state no spiral core, after transient cores appear, and later state persistent spiral core are detected. Local order parameter in Figures 6e and 7e where at early state we observe extreme weak value $< 0.2$ (domination of blue area), at intermediate state we observe strong spatial heterogeneity or chimera $\approx [0.5 - 0.6]$ (balance between the blue and red areas), and later state very close to 1 (domination of red area). Phase direction in Figures 6f and 7f where at early state we observe multiple propagation directions, at intermediate state we observe competing directional domains, and later continuous rotational direction. Radial phase gradients in Figures 6g and 7g where at early state we observe weak radial organization, at intermediate state we observe Irregular radial structure and later radial symmetry breaks and rotational gradients dominate. *2D* spatiotemporal *EEG*-like population signal activity in Figures 6h and 7h where we observe alternating coherent and incoherent bands and later high regular oscillatory bands as shows the zooming areas.

Thus, for the set $(g_C, g_E) = (1.5, 0.1)$, the early snapshots in Figure 5a,b display a highly fragmented traveling-wave regime with numerous irregular interfaces and no identifiable dominant rotation center. At $t = 1000$ and 2000 ms, Figure 5c,d show the spatial coexistence of extended regular domains and irregular fragmented wave fronts. This morphology is consistent with a transient chimera-like regime, although phase-based local-order measurements are required for a quantitative classification. At later times, Figures 5e,f exhibit increasingly connected and curved fronts, supporting the emergence of a persistent spiral-like or multispiral organization. For the set $(g_C, g_E) = (6, 0.1)$, the transition toward organized rotating structures is more pronounced. After the fragmented transient shown in Figure 5g,h, extended domains emerge in Figure 5i. Multiple well-developed curled wave fronts are subsequently observed in Figure 5j,l. Their large-scale spatial organization remains similar from $t = 2000$ ms to 5000 ms, providing morphological evidence of a persistent multispiral-wave regime. Nevertheless, the persistence of individual topological cores must be established separately through winding-number-based core tracking. A brief summary is given in Table 1.

**Table 1.** Classification of the observation from Figure 5.

| Coupling | Early Stage | Intermediate Stage | Late Stage |
|---|---|---|---|
| $g_C = 1.5$ | Fragmented traveling-wave transient, (Figure 5a,b). | Transient chimera-like coexistence, (Figure 5c,d). | Persistent spiral-like or multispiral organization, (Figure 5e,f). |
| $g_C = 6$ | Fragmented wave transient, (Figure 5g,h). | Short chimera-like or coarsening transition, (Figure 5i). | Late-time multispiral-wave morphology, (Figure 5j–l). |

All this demonstrates a continuous increase of synchronization and spatial organization, culminating a robust spiral-wave attractor that governs the collective dynamics of the entire network. Such behavior parallels mechanisms believed to underlie sensory integration, cognitive coordination, rhythm generation, and, under extreme synchronization conditions, pathological brain states such as seizure-like activity. The emergence of spiral waves under chemical dominance (Figure 5) is particularly significant because it suggests that the intrinsic excitatory-inhibitory balance without any structural heterogeneity is sufficient to seed pathological spiral activity, providing a mechanistic basis for focal seizure initiation in structurally normal tissue. These persistent rotating structures are classified as spiral-like states when they exhibit a stable phase singularity and a nonzero winding number like in the case of seizure propagation. Nevertheless, the present model does not include disease-specific ionic alterations,

seizure thresholds, clinical *EEG* recordings, or patient-derived parameters. The comparison with epilepsy should therefore be interpreted as a qualitative dynamical analogy rather than evidence that the simulated spiral states reproduce focal seizures.

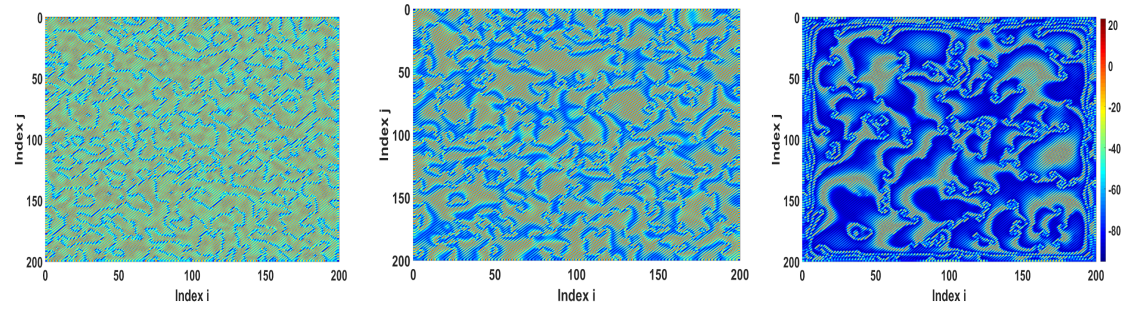


**(a)** $t$ = 10 ms. **(b)** $t$ = 100 ms. **(c)** $t$ = 1000 ms.

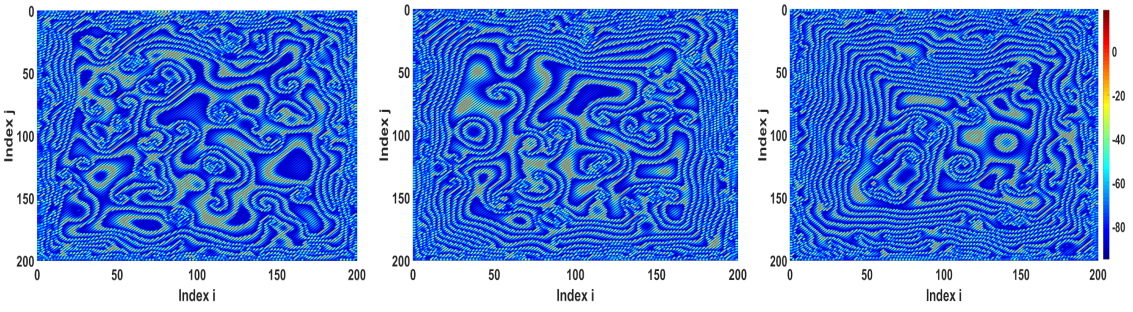


**(d)** $t$ = 2000 ms. **(e)** $t$ = 3000 ms. **(f)** $t$ = 5000 ms.

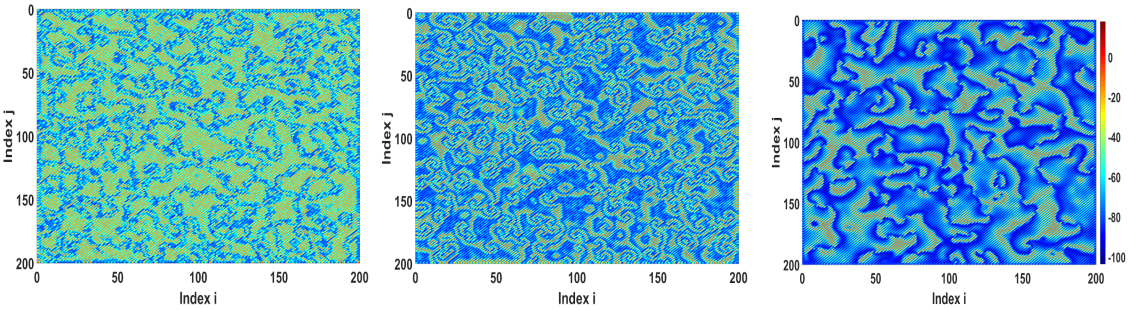


**(g)** $t$ = 10 ms. **(h)** $t$ = 100 ms. **(i)** $t$ = 1000 ms.

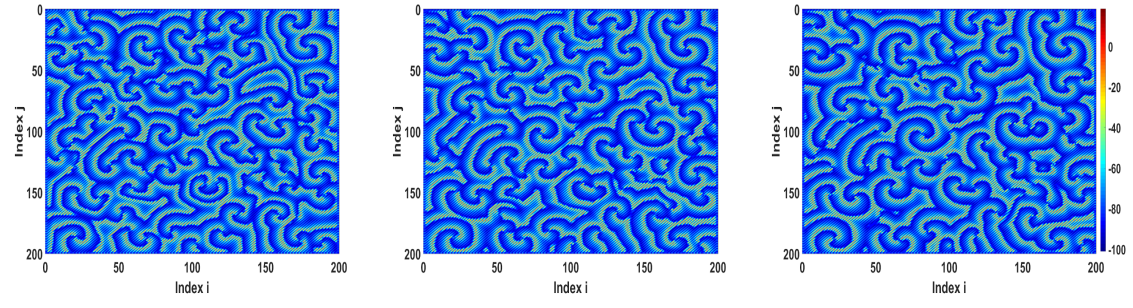


**(j)** $t$ = 2000 ms. **(k)** $t$ = 3000 ms. **(l)** $t$ = 5000 ms.

**Figure 5.** Spatiotemporal evolution of the membrane potential under chemical-coupling dominance for (**a**–**f**) $g_C = 1.5$ and (**g**–**l**) $g_C = 6$. The early states at $t = 10$ and $100\,\mathrm{ms}$ are characterized by fragmented wave activity. At $t = 1000$ and $2000\,\mathrm{ms}$, extended regular domains coexist with irregular wave fronts, producing a transient chimera-like morphology. At $t = 3000$ and $5000\,\mathrm{ms}$, the dynamics develops persistent spiral-like or multispiral spatial organization, particularly for $g_C = 6$. The terms "chimera-like" and "spiral-like" refer here to the observed morphology; quantitative temporal persistence requires local-order-parameter and winding-number analyses. Parameters: $\omega = 10^{-6}\,\mathrm{rad(ms)}^{-1}$, $A$ = 4 mA, $I$ = 2 mA and $g_E = 0.1$.

The resulting transitions among these wave-patterns transitions is explained by a hierarchical cascade of symmetry breakings, where each pattern has a longer characteristic time and a larger coupling range than the previous one, so that the system can only reach global order (target rings) after passing through local order (spiral) and mixed order (chimera). The sequence corresponds to a cascade of bifurcations where each bifurcation prepares the next one. The spiral only requires phase instability and including a lowest threshold. The chimera also requires an amplitude instability associated with a non-local coupling and including an intermediate threshold. Target rings require spatial instability (Turing) associated with frequency locking and including the highest threshold. In the simulations, increasing $g_C$ changes the regime from traveling waves to chimera-like states and then to spirals in Figure 5 describes how the brain shifts from local, flexible information processing (spirals) to an optimal cognitive state (chimera) and then to a rigid global state (target rings); any disruption to this sequence manifests clinically as neurological or psychiatric disorders. We do not claim that this sequence corresponds to a cognitive trajectory or to a clinical disorder. Parkinson disease exemplifies a forced transition from the chimera to beta target rings (motor blockade), whereas epilepsy represents an explosive transition to target rings (generalized seizure). In both cases, treatment aims to restore the healthy chimera or prevent the transition.

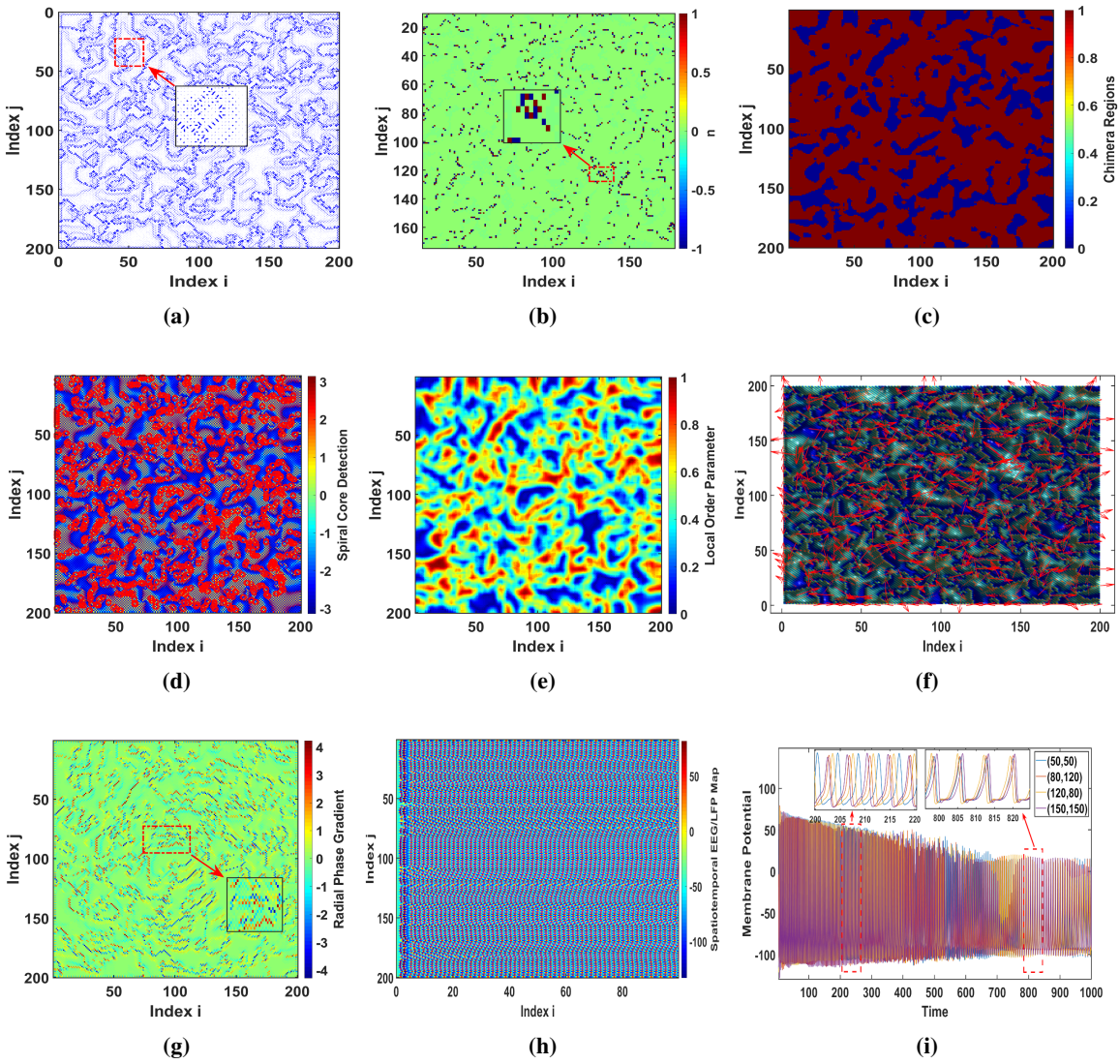


**Figure 6.** Characterization of key metric at $t = 100$ ms of snapshot of Figure 5b. (**a**) Gradient Phase direction; (**b**) winding number; (**c**) Chimera Regions; (**d**) Spiral Core Detection; (**e**) Local Order Parameter; (**f**) Phase Direction; (**g**) radial Phase Gradient; (**h**) *2D* Spaciotemporal *EEG*-like population signal and (**i**) Temporal evolution of four nodes. Parameters: $\omega = 10^{-6}\ \mathrm{rad(ms)}^{-1}$, $I$ = 2 mA $g_C = 1.5$ and $A$ = 4 mA and $g_E = 0.1$.

Figure 8 illustrates snapshots of hybrid connection when parameters $g_C$ and $g_E$ are such that $g_E > g_C$. For Figure 8a–h, we set $(g_E, g_C) = (1.5, 0.1)$ and for Figure 8i–p, we set $(g_E, g_C) = (3, 0.1)$. We observe significantly an alternation of color of the membrane potential where areas in red-yellow color (positive value of potential)

indicate depolarization phase of neuron, and areas in blue color (negative value of potential) indicates the resting or refractory state of neuron. The waves propagate step by step from node to node through electrical (gap-junction) coupling. For both setting of $g_E$, we have a similar traveling and a target wave patterns well organized and structured locking like Octagon Target Rings (*OTRs*) shapes. As time increases, waves are generated from the four corners of layer and propagate by reducing their size gradually to the center of square area of layer. Initially, we have sharp and regular propagation, indicating coherent activation. This introduces spatial asymmetry and anisotropic propagation due to the *EM* radiation, which have key interpretations on raster plotting nodes organization and *EEG*-like population signal description. For a large period of time, center of square area become also a source of waves generation, then producing interference and later disturbances which destroy coherence of traveling waves inside the layer. The octagonal target-ring geometry arises from the interplay between the discrete lattice structure of the network and the *EM* radiation and sinusoidal forcing. The lattice imposes eight preferred propagation directions (along the cardinal and diagonal axes), while the *EM* ($\approx \Omega_1$) and sinusoidal inputs ($\approx \Omega_2$) induce a directional resonance condition ($\Omega_2/\Omega_1 \approx 8$, as derived in Appendix A.2) that selects and locks these eight propagation modes, breaking the continuous rotational symmetry of an isotropic medium. Figure 9 illustrates temporal analysis of the global dynamics, which represent a resonant $D_8$-symmetric propagating mode unique to the discrete lattice architecture.

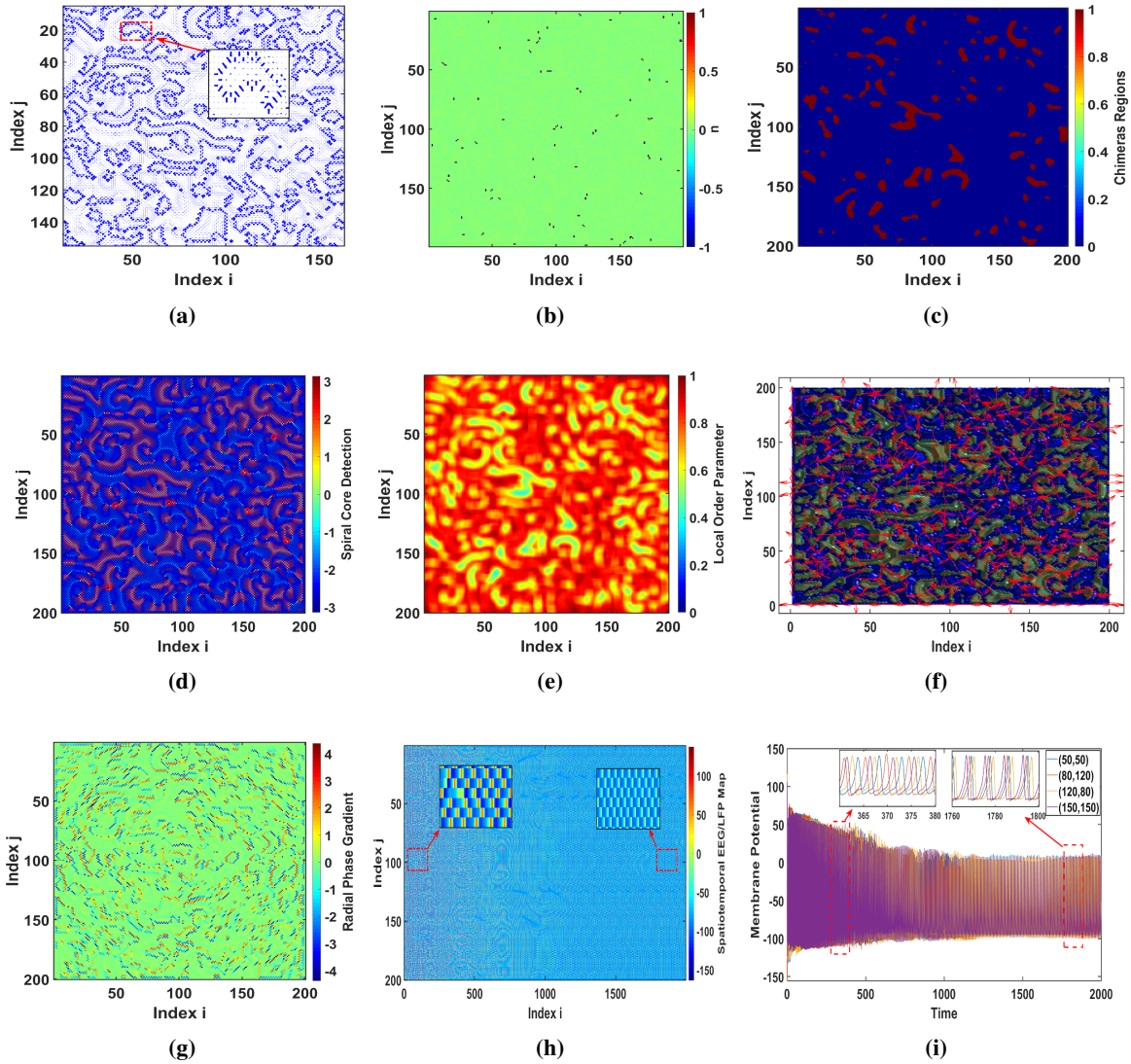


**Figure 7.** Characterization of key metric at $t = 2000$ ms of snapshot of Figure 5j. (**a**) Gradient Phase direction; (**b**) winding number; (**c**) Chimera Regions; (**d**) Spiral Core Detection; (**e**) Local Order Parameter; (**f**) Phase Direction; (**g**) radial Phase Gradient; (**h**) *2D* Spaciotemporal *EEG*-like population signal and (**i**) Temporal evolution of four nodes. Parameters: $\omega = 10^{-6}$ rad(ms)$^{-1}$, $I$ = 2 mA $g_C = 6$ and $A$ = 4 mA and $g_E = 0.1$.

Initially, we set $g_E = 1.5$ and $g_C = 0.1$ for the first analysis. Figure 10a illustrates temporal evolution of membrane potential of four nodes, $node - (50, 50)$, $node - (80, 120)$, $node - (120, 80)$, and $node - (150, 150)$,

where all exhibit common periodic oscillations, nearly identical dominant frequency close to *EEG*-like population signal frequency, since it reflects the global collective activity of the network. Initially, for $t \in [0-120]$ ms, the four nodes are strongly synchronized. After, we observed pair- synchronization for $t \in [120-170]$ ms and further a complete desynchronization of all nodes. A zooming is indicated for each time slot for a better observation. This desynchronization is due to the phase-shifted activity depending on its distance from the center of node indexes. Initially, we have smallest phase lag, which explain the synchronization of nodes, an further, continuous generation of outgoing wave-fronts. However, for $t \approx 200$ ms we observe weak-amplitude change of neurons indicating a weak disorganization of waves propagation, which also explain the very low incoherent patterns of Figure 8h at the center of the grid. The corresponding *EEG*-like population signal map of Figure 10b shows propagation of concentric wavefronts indicating oscillations of network. Gradually, after a period of $t = 60$ ms, a distortion with specific geometric shape appear until approximately period of $t = 150$ ms indicating a breaking of symmetry, due to the changing of local frequency or the velocity of the waves. Neurons locate at the corners are activated differently comparing to neurons at the centers, generating phase spatial gradient and traveling waves. For $t > 200$ ms, we observe that simple geometric patterns disappear gradually, intertwined structures, undulating, and fragmented. This behavior indicates that the global dynamics of network becomes chaotic with complex local desynchronization, which may explain the transitions of the brain from normal state towards some crisis state. Similar geometric shape is illustrate in Figure 10d by large *EEG*-like population signal amplitude decreasing over the time with stable oscillatory activity characterized by a dominant spectral component as indicated in Figure 9a with peak power of 17.37 dB. The raster plot of Figure 10c displays periodic and highly structured neuronal firing sequences forming diagonal activation bands associated with successive wavefront propagation. Figure 10e illustrates the temporal Eight-Fold Symmetry Index ($D_8(t)$ in blue color) where the different position of $D_8(t)$ at a specific time indicates the degree of symmetric pattern generated. The characterization of that degree are indicated with horizontal dotted line at specific threshold, described in Table A2. The thresholds reported in that table were applied to a calibrated eighth-order index. The background value $B_8$ was estimated as the median $D_8$ obtained from control simulations performed on the same square lattice without imposed octagonal organization. The ideal-reference value $I_8$ was estimated from noisy synthetic patterns containing eight equally weighted directions separated by $45°$. The calibrated index is calculated using Equation (A59). The limits 0.2, 0.5, and 0.7 represent approximately 20%, 50%, and 70% of the calibrated range between the lattice-dependent background and the ideal octagonal reference. The thresholds are not universal theoretical constants. They become meaningful only after the measured index has been normalized using the same numerical conditions as the neuronal simulations. These conditions include the lattice size, spatial resolution, boundary conditions, angular discretization, spectral band, preprocessing operations, and noise level. detailed description is given in Appendix A.8.8. The different nodes in red color indicate at specific time points, *t* = 20 ms, *t* = 60 ms, *t* = 100 ms, *t* = 130 ms, *t* = 150 ms, *t* = 160 ms, *t* = 180 ms and *t* = 200 ms where *(i,j)*-patterns are illustrated in Figure 8a–h when set $g_E = 1.5$, and at specific time points *t* = 20 ms, *t* = 60 ms, *t* = 100 ms, *t* = 120 ms, *t* = 130 ms, *t* = 140 ms, *t* = 150 ms and *t* = 160 ms in Figure 8i–p when set $g_E = 3$. The illustration shows that initially, the $D_8 \in [0.2-0.5[$ and further $D_8 \in [0.5-0.7[$ indicating transition between weak and strong structure. This is the case for $t \approx 20$ ms and $t \approx 50$ ms with $D_8 \approx 0.43$ and $D_8 \approx 0.51$ respectively. A square-grid-aligned target-wave state with an eighth-order angular component emerges at $t \approx 60$ ms as illustrating in Figure 8j where square pattern emerges. Further, octagonal target waves start emerge at $t \approx 100$ ms and become more visible at $t \approx 130$ ms, $t \approx 150$ ms and $t \approx 160$ ms as illustrated in Figure 8c–f respectively.

The temporal evolution of the calibrated eighth-order index in Figure 10e shows that $D_8^{\mathrm{cal}}$ (From Table A2) exceeds 0.7 ($D_8 \geq 0.7$) after approximately $t = 100$ ms and reaches $D_{8,\max}^{\mathrm{cal}} \approx 0.776$ at approximately $t = 160$ ms. This result demonstrates the presence of a strong eighth-order angular component in the phase-gradient distribution. However, $D_8^{\mathrm{cal}} \geq 0.7$ is not, by itself, sufficient to establish robust octagonal symmetry because a square-lattice pattern may also generate a large eighth-order harmonic. A robust octagonal classification additionally requires $D_8^{\mathrm{raw}} > T_{\mathrm{sig}}$, $D_8^{\mathrm{raw}} - D_4^{\mathrm{raw}} > T_\Delta$ together with eight resolved angular maxima whose successive circular separations are approximately $\Delta\theta_j \simeq \frac{\pi}{4} = 45°, j = 1, \ldots, 8$. Because these supplementary quantities have not been reported for the present simulation, the observed state is conservatively classified as a square-lattice-aligned target-wave pattern with a pronounced eighth-order angular component, rather than as confirmed robust octagonal symmetry. For the purpose of visualization, we set the time limit at 200 ms (for the parameter set $g_C = 0.1$ and $g_E = 1.5$); beyond this temporal threshold, the waves converge toward the center with an amplitude that progressively diminishes until they vanish. These results in a constant periodicity in the propagation, characterized by a single frequency as shown in the power spectrum in Figure 9a, which displays a prominent peak $\approx 17.37$ dB. Similar observation are illustrated from Figure 8i–p where 2D evolution of membrane potential show interesting patterns from a square-grid-aligned target-wave state with an eighth-order angular component to effective octagonal

symmetry shape. Analysis are observed for $t \in [20 - 160]$ ms, and comparing from the previous case where we observe big similarity, a resonance-enhanced lattice-anisotropic target-wave state is reached faster. From the $D_8$ curve of Figure 11e, the maximum symmetry is obtained when $t \approx 120$ with $D_{8,max} \approx 0.7$.

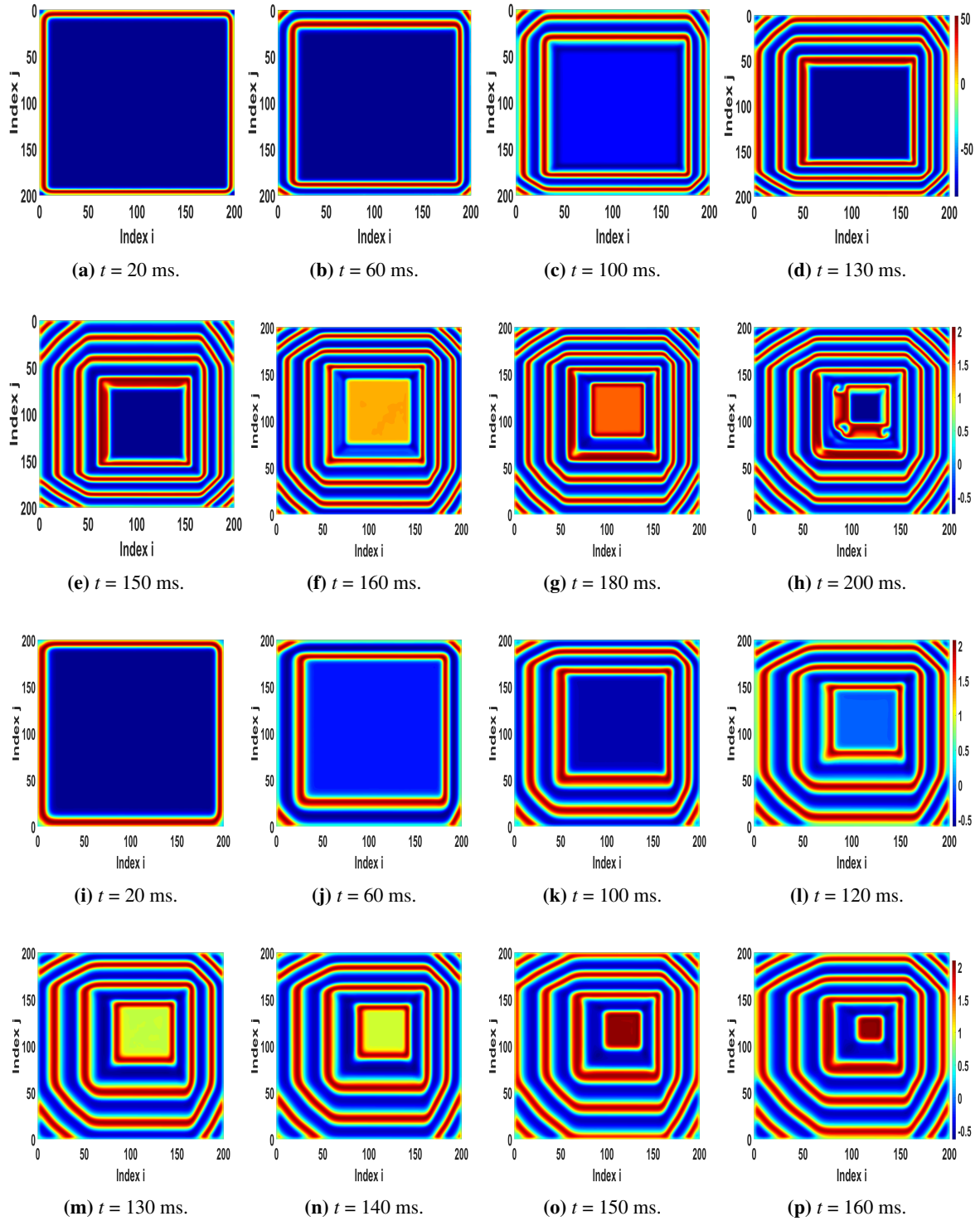


**(a)** $t$ = 20 ms. **(b)** $t$ = 60 ms. **(c)** $t$ = 100 ms. **(d)** $t$ = 130 ms.

**(e)** $t$ = 150 ms. **(f)** $t$ = 160 ms. **(g)** $t$ = 180 ms. **(h)** $t$ = 200 ms.

**(i)** $t$ = 20 ms. **(j)** $t$ = 60 ms. **(k)** $t$ = 100 ms. **(l)** $t$ = 120 ms.

**(m)** $t$ = 130 ms. **(n)** $t$ = 140 ms. **(o)** $t$ = 150 ms. **(p)** $t$ = 160 ms.

**Figure 8.** Spatiotemporal evolution of membrane potential under electrical coupling dominance ($g_E > g_C$) for two electrical coupling strengths: (**a**–**h**) $g_C = 0.1$ and $g_E = 1.5$; (**i**–**p**) $g_C = 0.1$ and $g_E = 3$. Development of concentric rectangular (target-like) patterns of membrane potential in a layer at different periods as time increases. Parameters: $\omega = 10^{-6}\ \mathrm{rad(ms)}^{-1}$, $I$ = 2 mA and $A$ = 4 mA.

The validation of *OTRs* patterns is also observed by illustration of key metrics in Figures 9 and 12. The spatiotemporal activity observed approximately at $t$ = 150 ms of Figure 8e exhibits all the characteristic signatures of a well-developed *OTRs* patterns as showed snapshots in Figures 9 and 12. The *EEG*-like population signal

frequency analysis in Figures 9a (*1D*) and 9b (*2D*) respectively, reveals a dominant spectral peak power around 17.37 dB, indicating the presence of a stable oscillatory regime. The persistence of this dominant frequency in both the *1D* temporal representation and the *2D* spatial-frequency map suggests that the network dynamics are governed by a coherent oscillatory mode rather than a broadband or chaotic activity. Such a dominant spectral component is consistent with resonant wave propagation and provides evidence that the network supports a stable large-scale oscillation capable of organizing the observed octagonal structure.

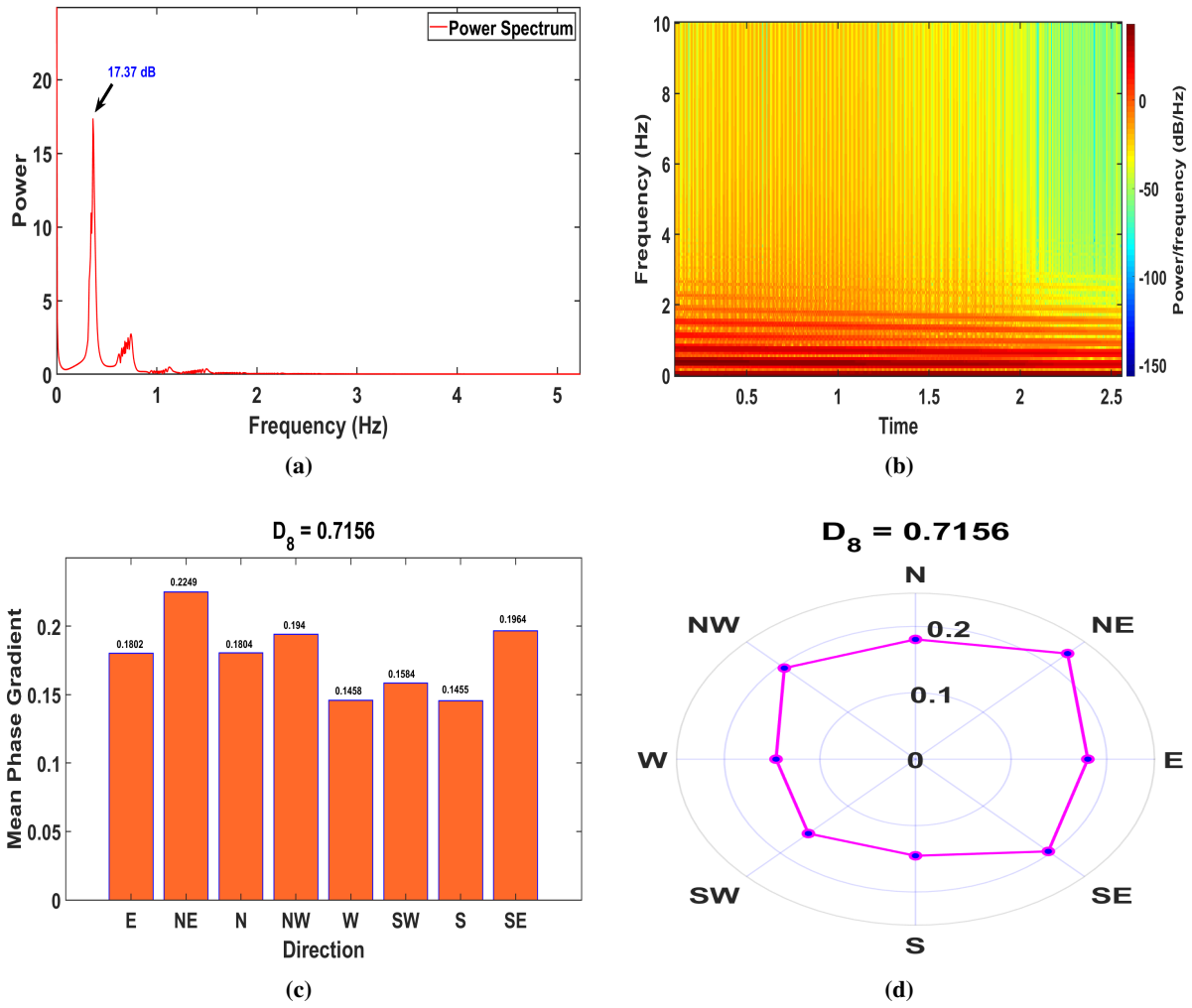


**Figure 9.** Dynamical Quantifiers pattern at $t = 150$ ms of Figure 8e. (**a**) *EEG*-like population signal peak power over the frequency; (**b**) 2D *EEG*-like population signal temporal signal at; (**c**) $D_8$ histogram indicating Directional Strength and (**d**) polar Octagonal symmetry. Parameters: $g_E = 1.5$, $g_C = 0.1$, $\omega = 10^{-6}$ rad(ms)$^{-1}$, $I$ = 2 mA and $A$ = 4 mA.

The $D_8$ Directional Strength analysis in Figure 9c demonstrates the existence of eight preferred propagation sectors corresponding to the directions East (*E*), Northeast (*NE*), North (*N*), Northwest (*NW*), West (*W*), Southwest (*SW*), South (*S*), and Southeast (*SW*). The histogram of mean phase gradients measured along these directions indicates that wave propagation is not isotropic but instead exhibits a distinct octagonal organization. This observation is further confirmed by the polar representation of the $D_8$ symmetry index in Figure 9d, where the angular distribution forms an approximately regular octagon. The eight preferred directions are not arbitrary but emerge from the square lattice topology. In a continuous medium, target waves would propagate as perfect circles with uniform radial phase gradients. However, in our discrete network, the nearest-neighbor coupling (Equation (7)) introduces an inherent anisotropy: propagation along the cardinal axes (horizontal/vertical) and diagonal axes follows different effective path lengths, generating an angular ($\cos(4\theta)$) modulation in the dispersion relation. When the *EM* frequency $\Omega_1$ and the sinusoidal driving frequency $\Omega_1$ satisfy the resonance condition ($\Omega_2/\Omega_1 \approx 8$, the nonlinear memristive coupling mixes these modes and produces constructive interference along all eight channels simultaneously. This phase-locking mechanism locks the wavefront geometry into the observed octagonal pattern,

with the $D_8$ index providing a quantitative measure of this symmetry. A large $D_8$ index ($> 0.7$) indicates that the phase-gradient field possesses strong eight-fold rotational symmetry, which is the defining geometric feature of Octagonal Target Rings.

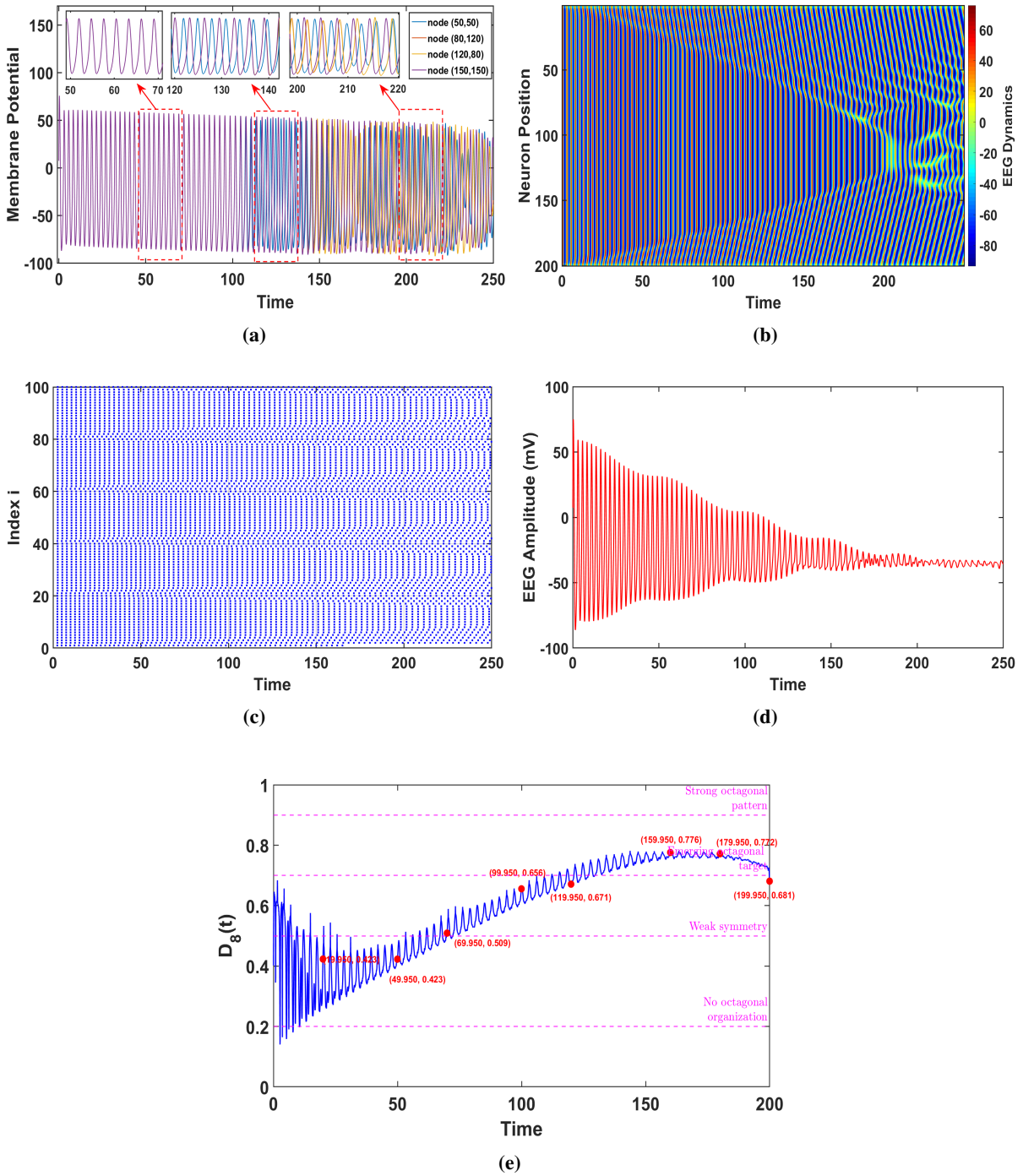


**Figure 10.** Dynamical Quantifiers pattern of Figure 8a–h: (**a**) Temporal evolution of membrane potential of four nodes; (**b**) Spatiotemporal *EEG*-like population signal Dynamics; (**c**) Raster plot of neuron *index i*; (**d**) *EEG*-like population signal temporal signal and (**e**) Temporal evolution of octagonal symmetry. Parameters: $g_E = 1.5$, $g_C = 0.1$, $\omega = 10^{-6}$ rad(ms)$^{-1}$, $I$ = 2 mA and $A$ = 4 mA.

The phase-gradient map and its enlarged view on a specific area illustrates in Figure 12a reveal a highly organized radial arrangement of phase contours. The gradients originate from a central pacemaker-like region and propagate outward along eight preferential directions. Unlike ordinary circular target waves, where phase gradients are uniformly distributed in all directions, the *OTR* exhibits alternating regions of enhanced propagation corresponding to the vertices of the octagon. This confirms that the underlying wave-fronts are modulated by a $D_8$ spatial mode.

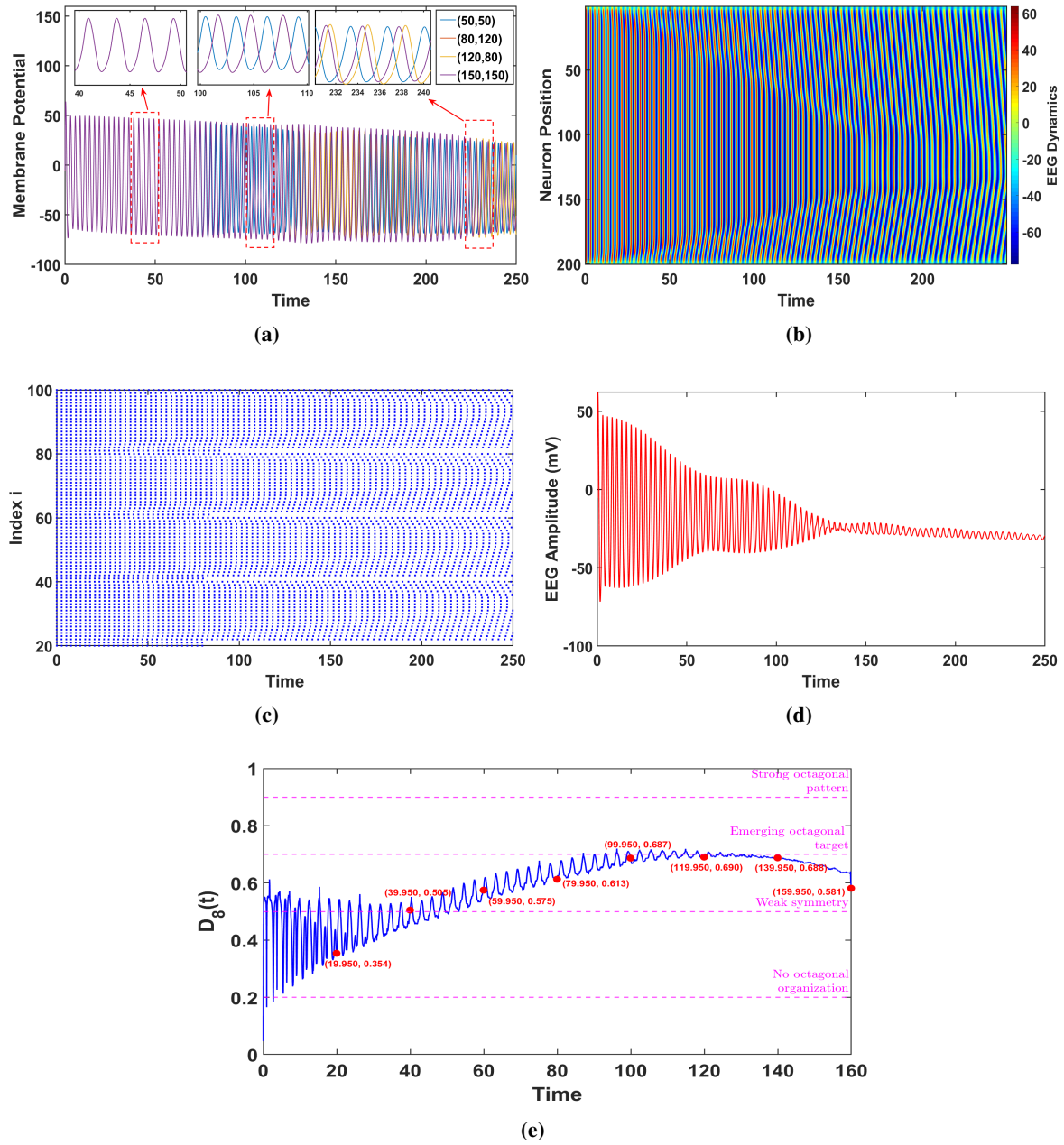


**Figure 11.** Hybrid interaction: Quantifiers parameters of Figure 8i–p. (**a**) Temporal evolution of membrane potential of four nodes; (**b**) Spatiotemporal *EEG*-like population signal Dynamics; (**c**) Raster plot of neuron *index i*; (**d**) *EEG*-like population signal temporal signal and (**e**) Temporal evolution of octagonal symmetry. Parameters: $g_E = 3$, $g_C = 0.1, \omega = 10^{-6}$ rad(ms)$^{-1}$, $I$ = 2 mA and $A$ = 4 mA.

The winding number analysis yields a value close to zero ($n \approx 0$) as illustrated with uniform green surface in Figure 12b, indicating the absence of phase singularities. This result is crucial because it distinguishes the observed pattern from spiral waves. Spiral waves are characterized by non-zero winding numbers ($n = \pm 1, \pm 2, \cdots$) and contain a rotating singular core. The near-zero winding number therefore confirms that the observed structure is a genuine target-wave pattern rather than a hidden or fragmented spiral wave. The chimera analysis shows a uniform coherent region (in dark blue color) illustrated in Figure 12c rather than a coexistence of coherent and incoherent domains. This observation indicates that the network has evolved beyond a chimera state toward a globally organized wave pattern. The local order parameter illustrated in Figure 12d indicates a range $R_{local}(t) \in [0.8 - 1]$, demonstrating high level of local phase synchronization. Neighboring neurons oscillate almost in phase, allowing the wave-fronts to propagate smoothly without fragmentation. Such a high local coherence is a prerequisite for maintaining stable octagonal wave structures over large spatial scales. The radial phase-gradient analysis illustrates in Figure 12e reveals outward propagation from a central source, which is the hallmark of target waves. The phase gradient vectors point away from the center and maintain a highly ordered configuration, confirming that

the pattern is generated by a central pacemaker mechanism. However, unlike classical circular target waves, the propagation speed and gradient magnitude vary periodically with direction, producing the octagonal deformation of the wave-fronts. The spiral-core detection analysis illustrated in Figure 12f does not identify any stable phase singularity or rotating core. This observation is fully consistent with the winding-number result and further supports the conclusion that the pattern belongs to the target-wave family rather than the spiral-wave family.

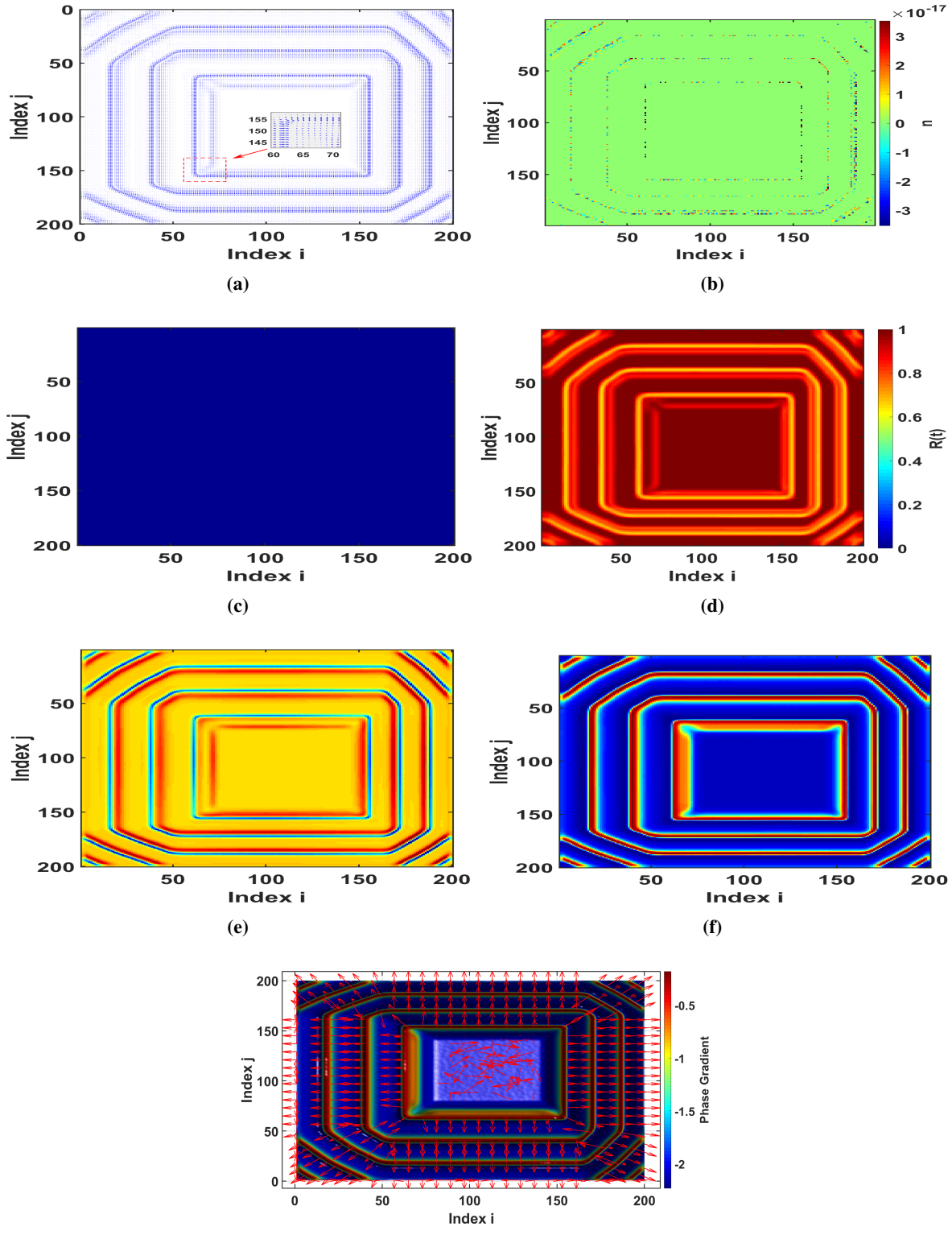


**Figure 12.** Dynamical Quantifiers pattern at $t = 150$ ms of Figure 8e. (**a**) Phase Gradient; (**b**) Winding Number; (**c**) Chimera Regions; (**d**) Local Order Parameter; (**e**) Radial Phase Gradient (Target Waves); (**f**) Spiral Core Detection; and (**g**)Wave Propagation Direction. Parameters: $g_E = 1.5$, $g_C = 0.1$, $\omega = 10^{-6}\ \mathrm{rad(ms)}^{-1}$, $I = 2$ mA and $A = 4$ mA.

The propagation-vector field (indicate with arrow of red color) superimposed on the phase map illustrated in Figure 12g clearly shows eight dominant propagation channels aligned with the $D_8$ symmetry axes. These vectors provide direct evidence of anisotropic wave transmission within the network. The propagation is strongest along the eight principal directions, producing a spatial organization that closely matches the geometry of an octagon. These observations collectively demonstrate the existence of a stable Octagonal Target Ring (*OTR*) state. The large $D_8$ ($\approx 0.7156$) symmetry index quantifies the degree of octagonal organization, while the near-zero winding number confirms the target-wave nature of the pattern.

We set $(g_E, g_C) = (3, 0.1)$ for the first analysis, and Figure 8i–p illustrate the snapshots of membrane potential where we observe target waves propagation for different position of the node indexes at the same periods of time as analyzed previously. Similar analysis was performed to validation patterns generated in Figures 11, 13 and 14. Temporal analysis of the global dynamics show similar behaviors as study previously. The temporal evolution of the membrane potential in Figure 11a shows periodic oscillations with effective synchronization of the four nodes, later the synchronization is effective two by two and further each node oscillate independently as illustrated by the zooming areas. As time increases, phase-shifted is observed, which explain the desynchronization. The oscillations of each node is similar with an approximate lock frequency close to the dominant *EEG*-like population signal frequency illustrated on Figure 13a with a peak power of 13.23 dB while maintaining spatially organized phase delays determined by their position within the target-ring structure. The illustration of raster plot, *EEG*-like population signal dynamics of Figure 11b–d respectively have similar dynamics as observed on Figure 10b–d. However, for $t > 200$ ms, the patterns generated are coherent suggesting self-sustaining wave structures.

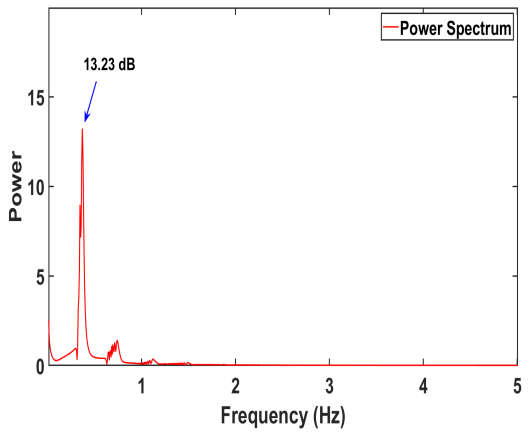


**(a)** *EEG* signal at $t$ = 130 ms.

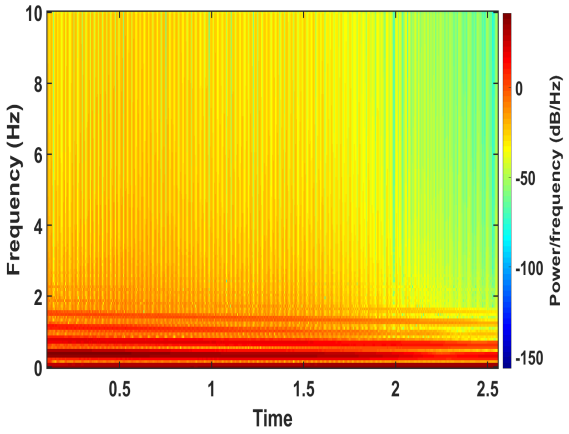


**(b)** *2D EEG* Temporal signal at $t$ = 130 ms.

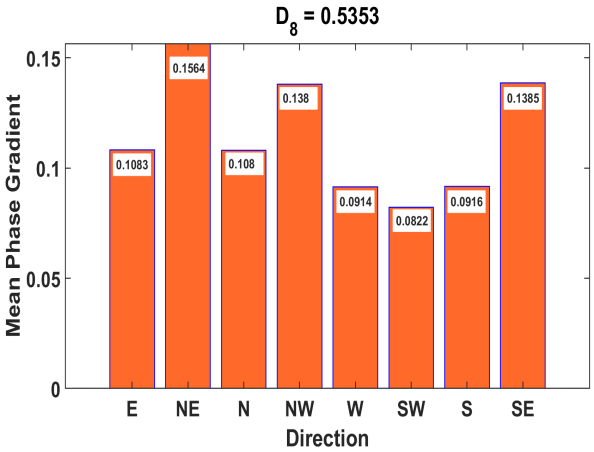


**(c)** $D_8$ Directional Strength at $t$ = 130 ms.

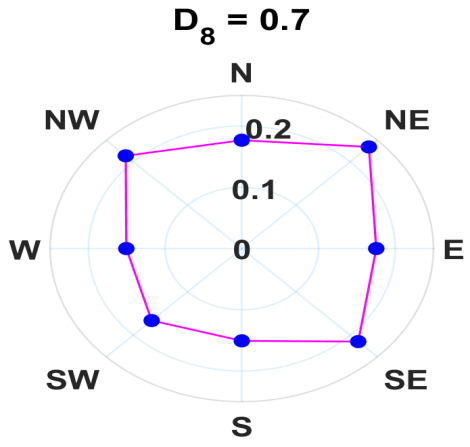


**(d)** Octagonal symmetry at $t$ = 130 ms.

**Figure 13.** Dynamical Quantifiers pattern at $t$ = 130 ms of Figure 8m. (**a**) *EEG*-like population signal peak power over the frequency; (**b**) *2D EEG*-like population signal temporal signal at, (**c**) $D_8$ histogram indicating Directional Strength and (**d**) polar Octagonal symmetry. Parameters: $g_E = 3$, $g_C = 0.1$, $\omega = 10^{-6}$ rad(ms)$^{-1}$, $I$ = 2 mA and $A$ = 4 mA.

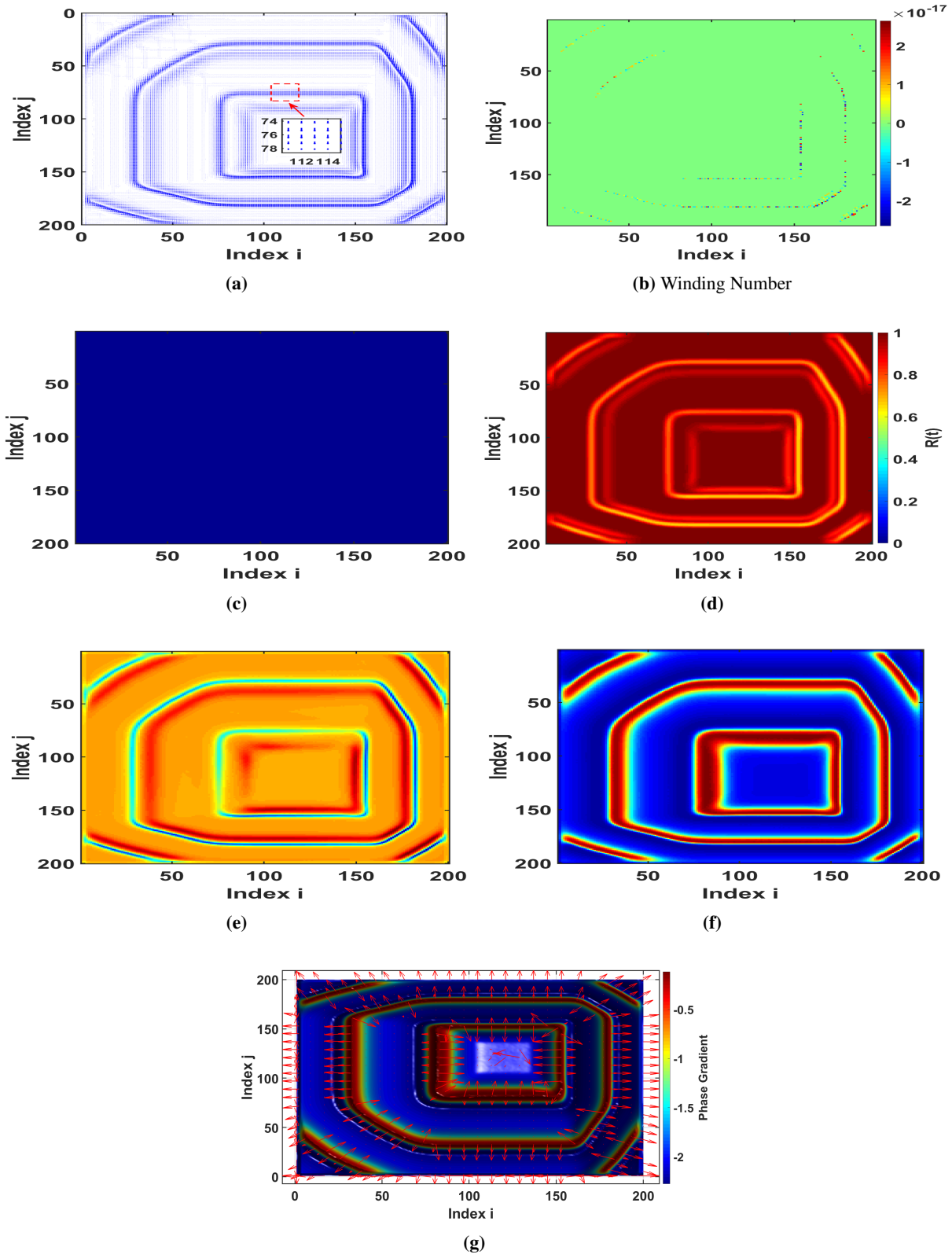


**Figure 14.** Dynamical Quantifiers pattern at $t = 130$ ms of Figure 8m. (**a**) Phase Gradient; (**b**) Winding Number; (**c**) Chimera Regions; (**d**) Local Order Parameter; (**e**) Radial Phase Gradient (Target Waves); (**f**) Spiral Core Detection; and (**g**) Wave Propagation Direction. Parameters: $g_E = 3$, $g_C = 0.1$, $\omega = 10^{-6}$ rad(ms)$^{-1}$, $I$ = 2 mA and $A$ = 4 mA.

The $D_8(t)$ index in Figure 11e demonstrates weak symmetric as a maximum of the eight preferred propagation sectors for $t \approx 100$ ms ( Figure 8k), and later a complete absence of octagonal organization. For $t = 130$ ms, we estimate $D_8$ ($t = 130$ ms) $\approx 0.7$, the corresponding histogram of mean phase gradients of Figure 13c and the polar representation of Figure 13d show that The phase velocity is close to isotropic across the eight sectors (report the

min–max spread); this is hard to reconcile with an eight-fold anisotropic pattern.

For a better prediction of snapshots illustration in Figures 5 and 8 for hybrid connection, we investigate *SF* and *SE*, and results are given on Figure 15. Parameters considered during simulation are given on Table 2. Figure 15a illustrates summary of patterns illustrated on Figure 5a–f where *SF*-parameter and *SE*-parameter are close to 0 and 1 respectively when $t \in [0 - 500]$ ms for $(g_C, g_E) = (1.5, 1)$. Gradually, the dynamics grows to a steady state above a threshold of 1000 ms with a threshold $\approx 0.3$ and $\approx 0.91$ for *SF* and *SE* respectively where dynamics remains constant. After we set $(g_C, g_E) = (1.5, 0.1)$ and $(g_C, g_E) = (6, 0.1)$, for Figure 15b,c illustrate *SF* and *SE* respectively, where the temporal patterns history are given on Figure 5a–f and Figure 5g–l where we better observe the generation of multiple patterns in spaciotemporal. Later we set $(g_C, g_E) = (0.1, 1.5)$ and $(g_C, g_E) = (0.1, 3)$, Figure 15d,e illustrate summary of Figure 8a–h respectively. The temporal evolution of *SF* and *SE* reveals that the network crosses a sequence of dynamical states from initial desynchronization (disordered network, high *SE*) through transient partial synchrony (chimera formation) to either sustained chimera (chemical dominance) or organized wave propagation (electrical dominance) before settling into a statistically stationary regime.

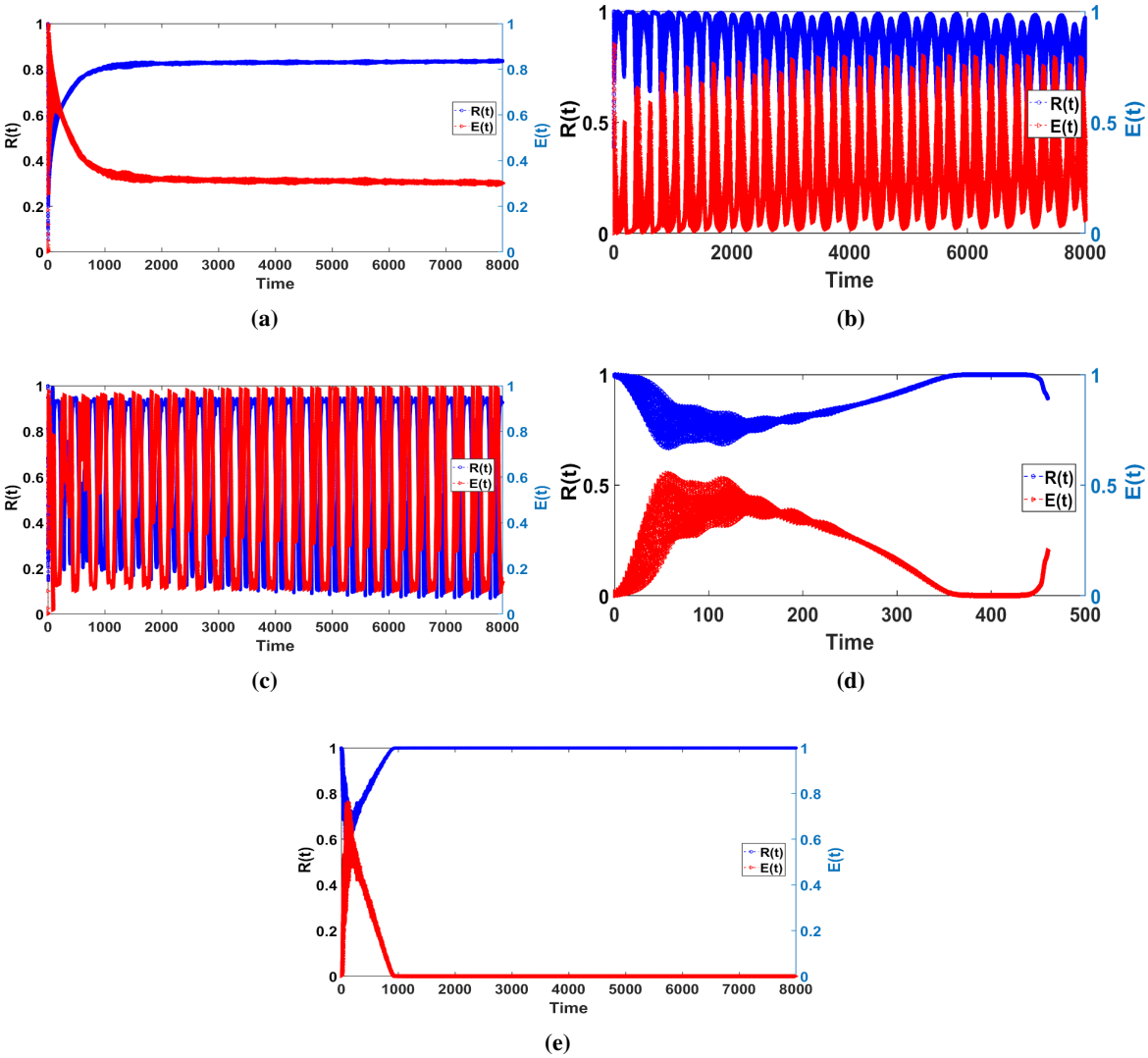


**Figure 15.** Temporal evolution of the global synchronization factor $R(t)$ (SF, blue curves; left vertical axis) and the corresponding synchronization error $E(t)$ (SE, red curves; right vertical axis) for different combinations of electrical and chemical coupling strengths indicating the degree of synchronization state and a prediction for networks to generate interesting patterns (spiral, target or chimera patterns) as seen in Figures 5 and 8. Keys parameters are given in Table 2: (**a**) $g_E = 0.1$, $g_C = 1$; (**b**) $g_E = 0.1$, $g_C = 1.5$; (**c**) $g_E = 0.1$, $g_C = 6$; (**d**) $g_E = 1.5$, $g_C = 0.1$; and (**e**) $g_E = 3$, $g_C = 0.1$. In all panels, $A = 4$ mA, $I = 2$ mA, and $\omega = 10^{-6}$ rad ms$^{-1}$; the remaining parameters are unchanged. Values $R(t) \to 1$ and $E(t) \to 0$ indicate increasing global phase synchronization, whereas $R(t) \to 0$ and $E(t) \to 1$ indicate global desynchronization. Persistent oscillations or intermediate values represent time-dependent partial synchronization.

It is important to notice that target waves observed when we have dominance of electrical connection $g_E > g_C$ have fast generation and propagation period $\approx 250$ ms and successive patterns when we have dominance of chemical connection $g_E < g_C$ have slow generation and propagation period $\approx 5000$ ms, since each pattern requires significant time to properly observe it shape. This is because electrical synapse establish a faster and direct connection during a coupling with neighboring nodes compared to chemical synapse indirect, involving migrations of neurotransmitters from one node to another through synaptic cleft.

**Table 2.** Parameters used to illustrate *SF* and *SE* for hybrid interaction illustrated on Figures 5 and 8.

| $A$ (mA) | $I$ (mA) | $g_E$ | $g_C$ | $\omega\ (\mathrm{rad(ms)}^{-1})$ | Figure |
|---|---|---|---|---|---|
| 4 | 2 | 0.1 | 1 | $10^{-6}$ | Figure 15a |
| 4 | 2 | 0.1 | 1.5 | $10^{-6}$ | Figure 15b |
| 4 | 2 | 0.1 | 6 | $10^{-6}$ | Figure 15c |
| 4 | 2 | 1.5 | 0.1 | $10^{-6}$ | Figure 15d |
| 4 | 2 | 3 | 0.1 | $10^{-6}$ | Figure 15e |

The novelty of this analysis lies in applying the same classification framework to all observed pattern regimes. Spiral-like states are distinguished from target waves by persistent nonzero winding numbers and stable phase singularities. Chimera-like states are identified by the persistent coexistence of high- and low-local-order domains, whereas traveling and target waves exhibit coherent phase-gradient organization without stable topological cores.

## 5. Interaction of Three Networks under Sinusoidal Stimulation

An interesting phenomenon observed in the brain is the capacity of interactions for different neural regions that synchronize their activities to perform a specific task [16, 133–137]. Figure 16 illustrates an architecture of three networks interacting together, all submitted to sinusoidal stimulation. Unlike previous studies that mainly characterize wave formation within a single layer, the present architecture examines whether spatial wave organization and population-level synchrony persist across three interacting networks when only the peripheral networks receive direct external stimulation. The middle network therefore serves as a topological integration node. This stimulation is similar of some brain particularities such as binaural synchronization behaviors like binaural beats which are an auditory illusion that happens when you listen to two slightly different frequencies in each ear at the same time. The brain hears a third pulsing rhythm corresponding to the difference between the two frequencies. some experimental investigation illustrate possibilities to use this mechanism to assist care of patient trough sound waves stimulation [138–141] or control specific brain region in the aim to improve cognitive and motor functions [142–146].

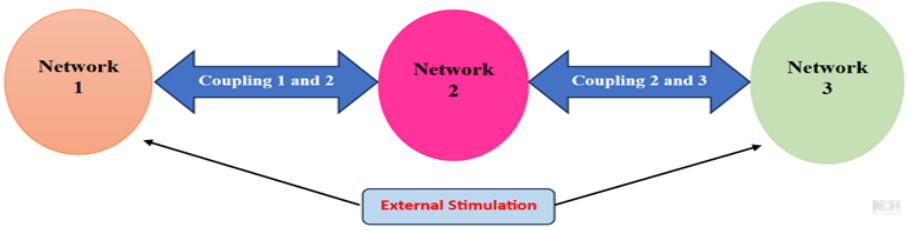


**Figure 16.** Scheme of three networks interacting together through coupling (magnetic and electrical). Networks 1 & 3 are submitted to external sinusoidal stimulation and both interact with network 2.

The couplings between networks are combination of inter-electrical coupling and magnetic field. Network 2 is influenced simultaneously by Networks 1 & 3, both receiving external sinusoidal stimuli, in the purpose to observe similarities degree and information exchanges of the global dynamics behavior between networks. Thus, we link network 1 and network 3 to the left ear and right ear where an input sound is associated to sinusoidal stimulation illustrated in our study apply at each ear. Network 2 is the mid-network or hub which analyzes information from networks 1 and 3, adapt his functioning and establish global synchronization between them. The stimulation configuration should be interpreted as a minimal convergent-input motif rather than as a literal anatomical reconstruction of three specific brain regions. Networks 1 and 3 represent input populations receiving exogenous rhythmic drives, whereas Network 2 represents an undriven integrative population whose activity emerges exclusively through inter-network interactions. To evaluate the sensitivity of the pairwise directional asymmetry to the peripheral inputs, six combinations of stimulus-frequency and amplitude ordering were considered: $\omega_1 < \omega_3$ and $\omega_1 > \omega_3$, each combined with $A_1 > A_3$, $A_1 < A_3$, and $A_1 = A_3$.

The brain has the remarkable capacity to coordinate activity simultaneously across multiple cortical regions, depending on the nature of the information to be processed and the required action. When a region of the nervous system receives an external stimulus, the resulting neural signals are relayed to the cerebral cortex, which process and share the responses to specific others brain regions for execution [85, 135, 147–149]. This key part of brain is responsible for higher level processes, including language, memory, reasoning, thought, learning, decision making, emotion, intelligence and personality [150–157]. Frontal cortex is the main part of brain responsible of monitoring others parts of brain such that an action can be performed (eyes movements, displacement, arm movements) [158–164]. The activities of brain patterns are nowadays well known through functional magnetic resonance imaging (*fMRI*) involving traveling waves, where it is possible to easily identify the brain area [165–172] and estimate some key parameters (like oxygen level, energy consumption and others.) for different areas. To ensure an adequate exchanges between networks (Figure 16), it is important to set coupling parameters $(g_E, g_C, g_M)$ at the appropriate value range to maintain the correct flow (synchronization) of information over the time. The studies conduct by Azangue et al. in 2023 have showed that for two *eHR* neurons coupled with electrical coupling only, the synchronization is effective when the coupling strength is greater that a threshold of $g_E \approx 0.5$ [74]. In this analysis, we investigate the range of values that electrical coupling strength $g_E$ and magnetic coupling strength $g_M$ involve synchronization state for a fix value of $g_C$ of two *eHR* neurons and Equations (12) and (13) illustrate the coupling.

$$\dot{X}_1 = F(X_1) + g_E(x_2 - x_1) + g_C^{inh} R_{x_1}^{'}\left(E_{rev}^{inh} - x_2\right) + g_C^{exc} R_{x_1}^{'}\left(E_{rev}^{exc} - x_2\right) + g_M \phi_2, \tag{12}$$

and

$$\dot{X}_2 = F(X_2) + g_E(x_1 - x_2) + g_C^{inh} R_{x_2}^{'}\left(E_{rev}^{inh} - x_1\right) + g_C^{exc} R_{x_2}^{'}\left(E_{rev}^{exc} - x_1\right) + g_M \phi_1. \tag{13}$$

Figure 17a,b illustrate the Lyapunov Transverse ($\lambda_{max}^T$) indicating two main areas, area A and B indicating desynchronization and synchronization respectively of both neurons when varying the electrical coupling and magnetic coupling strengths ($g_E$ and $g_M$) and maintain constant chemical coupling strength ($g_C$) respectively. Figure 17c,d illustrate temporal evolution of membrane potential and asymptotic error respectively, indicating desynchronization state for the coupling strength parameters $(g_E, g_C, g_M) = (0.2, 0.2, 0.2)$ taken in area A, and Figures 17e,f illustrate temporal evolution of membrane potential and asymptotic error respectively which show synchronization state for the coupling strengths $(g_E, g_C, g_M) = (0.6, 0.2, 0.3)$ taken in area B. This analysis helps to choose $(g_E, g_C, g_M)-$ parameters accurately to ensure a good control of networks exchanges illustrated in Figure 16.

In the architecture of Figure 16, we assume that Network 2 is similar to cerebral or frontal cortex which receives and processes information, and assume that Networks 1 & 3 are similar to other areas of brain responsible of providing key inputs information like vision (occipital lobe), sound (auditory cortex) or touch (parietal lobe). An additional biological analogy is sound localization via binaural input: the auditory system integrates signals arriving independently at each ear (analogous to Networks 1 & 3 receiving independent stimulation) and computes their difference in the auditory cortex (analogous to the integrative processing of Network 2) [74, 138, 173–175], where each part of brain hemisphere receive an external stimulation. Brain processes and synchronizes both stimulus at a single frequency equivalent to difference between these frequencies from external stimulation. The three illustrations for our analysis networks are not intended to represent specific cortical regions of brain, and the model does not contain anatomical connectivity derived from specific network area (the frontal, auditory, visual, or somatosensory) systems. We wish to analyze effect of Networks 1 & 3 submitted to external stimulus over Network 2, where inter-coupling is made with gap and magnetic connections. The purpose is to observed patterns formation in Network 2 and compare these dynamics with patterns observed in Networks 1 & 3. For analysis, we define Equations (14)–(16) for Network 1, Network 2 and Network 3 respectively.

$$\begin{cases} \dot{X}_{(i,j,1)} = F(X_{(i,j,1)}) + I_{ext}(1) + I_{hyb}(i,j,1) \\ +C_{12} + g_M^{12}\phi_{(i,j,2)}, \\ \beta_e \dot{R}^{'}{}_{(i,j,1)} = \dfrac{R_\infty(x_{(i,j,1)}) - R^{'}_{(i,j,1)}}{R_0 + R_\infty(x_{(i,j,1)})}, \end{cases} \tag{14}$$

$$\begin{cases} \dot{X}_{(i,j,2)} = F(X_{(i,j,2)}) + I_{hyb}(i,j,2) \\ +C_{21} + C_{23} + g_M^{21}\phi_{(i,j,1)} + g_M^{23}\phi_{(i,j,3)}, \\ \beta_e \dot{R}^{'}{}_{i,j,2} = \dfrac{R_\infty(x_{i,j,2}) - R^{'}_{i,j,2}}{R_0 + R_\infty(x_{i,j,2})}, \end{cases} \tag{15}$$

$$\begin{cases} \dot{X}_{(i,j,3)} = F(X_{(i,j,3)}) + I_{ext}(3) + I_{hyb}(i,j,3) \\ +C_{32} + g_M^{32}\phi_{(i,j,2)}, \\ \beta_e \dot{R'}_{i,j,3} = \dfrac{R_\infty(x_{i,j,3}) - R'_{i,j,3}}{R_0 + R_\infty(x_{i,j,3})}, \end{cases} \tag{16}$$

$C_{12} = g_E^{12}(x_2 - x_1)$, $C_{21} = g_E^{21}(x_1 - x_2)$, $C_{23} = g_E^{23}(x_3 - x_2)$ and $C_{32} = g_E^{32}(x_2 - x_3)$. Sinusoidal stimulation is applied at membrane potential by $I_{ext}(1) = A_1 \cos(\omega_1 t)$ for Network 1 and $I_{ext}(3) = A_3 \cos(\omega_3 t)$ for Network 3. For the analysis, we set the different coupling strengths as $g_E^{12} = g_E^{21} = g_E^{23} = g_E^{32} = g_E$ and $g_M^{12} = g_M^{21} = g_M^{32} = g_M^{23} = g_M$.

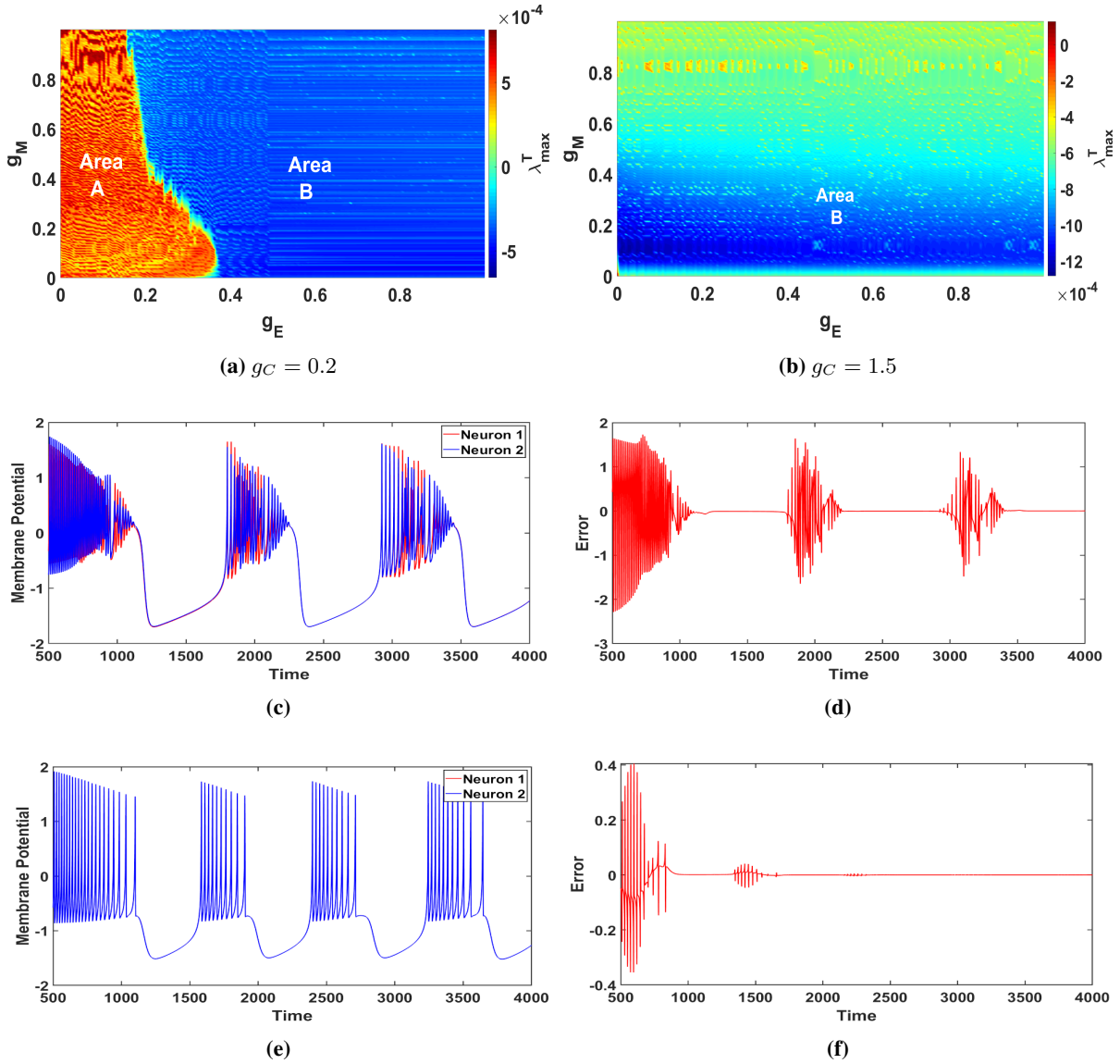


**(a)** $g_C = 0.2$ **(b)** $g_C = 1.5$

**(c)** **(d)**

**(e)** **(f)**

**Figure 17.** (**a**,**b**) *2D* illustration of Lyapunov Transverse indicating desynchronization in area A, and synchronization area B of two neurons. (**c**–**f**) temporal evolution of membrane potential and synchronization error of two neurons. The coupling strengths taken for illustration are for area A, $g_E = 0.2$, $g_C = 0.2$ and $g_M = 0.2$ in (**c**,**d**), for area B $g_E = 0.6$, $g_C = 0.2$ and $g_M = 0.3$ in (**e**,**f**).

Figure 18 illustrates patterns of membrane potential for different periods of time ($t$ = 50 ms, 100 ms, 150 ms, 200 ms, 250 ms) for the three networks where we observe a sequence of target waves generated. Coupling parameters are taken in area B of Figure 17 where synchronization is established. We observe that waves generated by each network are similar, and significantly coherent for each snapshot of different period of time. This evolution from ordered waves propagation to complex, multiscale irregular activity closely parallels to the oscillatory dynamics observed in the brain

during neurodegenerative disease progression. In Alzheimer's disease and Parkinson's disease, the degradation of inter-regional white matter connectivity which reduces the effective inter-network coupling is associated with the progressive loss of organized low-frequency oscillations and the emergence of high-dimensional, irregular network activity that no longer supports coherent information transfer [29,30,45–47]. For a detailed validation of this similarity and coherence, we compare the networks two-by-two, where some key metrics are illustrated on Figure 19. Figure 19a illustrates inter-network synchronization in a matrix form described by Equation (17) where the inter-Kuramoto parameters $R_{lk}$ $((lk) = 1, 2, 3)$ $l \neq k$, is close to 1, indicating a global coherence and synchronization between the networks. The present analysis does not incorporate disease-specific neuronal degeneration, neurotransmitter changes, anatomical connectivity loss, or patient data. The results therefore provide only a generic computational hypothesis about the consequences of weakened inter-network coupling and should not be interpreted directly as a model of either disease.

$$\text{Kuramoto Matrix} = \begin{bmatrix} 1 & R_{12} & R_{13} \\ R_{21} & 1 & R_{23} \\ R_{31} & R_{32} & 1 \end{bmatrix} \tag{17}$$

Figure 19b illustrates *PLV* two-by-two of networks where the value is also close to 1 ($PLV \approx 0.999$ between Networks 1 & 2; $PLV \approx 0.998$ between Networks 1 & 3; $PLV \approx 0.997$ between Networks 2 & 3.) indicating stable phase locking between networks, thus stable oscillatory relationship. Figure 19c compares shared oscillatory frequencies in the networks and indicates high *EEG*-like population signal coherence, thus high inter-network coherence among the networks. This observation is in good agreement with illustration of *EEG*-like population signal over the time of Figure 19g where all are similar. The trajectory of *EEG* illustrated has a direct similarity with brain: The sequence of *EEG* amplitude changes observed during the transition from wakefulness into non-REM sleep, in which the cortex progressively transitions from a high frequency, low-amplitude desynchronized state through intermediate sigma-band oscillation (sleep spindles, which are target-wave-like) into the high-amplitude, low-frequency synchronized slow-wave state of deep sleep [1,55,56].

Figure 19e,f illustrate the Transfer Entropy (*TE*) and Normalized Directional Index (*NDI*) which measures and indicates directional information flow characterized by Equations (A30) and (A31) and in matrix form by Equations (18) and (19) respectively, and a detailed summary of global interpretation is given in Table 3. Additional information from Transfer Entropy is given in Appendix A.8.5. An observation of Figure 19e (colorbar) shows that $TE \approx 0$ with accuracy of $10^{-2}$, indicating an approximate balance during exchange of information between networks. We agree that these low value of $TE$ cannot be interpreted as evidence of statistically significant directed information transfer which constitute a gap of our analysis, that is why we fix a threshold of $10^{-2}$ during our simulations. The values reported in the present study are raw plug-in $TE$ estimates calculated from finite-length simulation time series. The $TE$ results are presented only as exploratory and descriptive measures of directional asymmetry. The results in Table 3 are done from the detailed analysis of Figures 20 and 21 and show that it is possible to predict the direction information flow for the networks. However, the direction is not fixed when the parameters of the stimulation change. We use six trials for the values for frequency-amplitude of stimulation of Networks 1 and 3. We define Unilateral hierarchy when the direction is either Network 1 $\rightarrow$ Network 2 $\rightarrow$ Network 3 or Network 3 $\rightarrow$ Network 2 $\rightarrow$ Network 1; Divergence from the hub when the direction is Network 1 $\leftarrow$ Network 2 $\rightarrow$ Network 3 ; or Convergence toward the hub when the direction is Network 1 $\rightarrow$ Network 2 $\leftarrow$ Network 3. The raw *TE* and *NDI* matrices reveal a parameter-dependent reconfiguration of pairwise predictive asymmetry. The direction Network 3 $\rightarrow$ Network 2 $\rightarrow$ Network 1 ordering is recovered only for $\omega_1 < \omega_3$ and $A_1 > A_3$. For the same frequency ordering but $A_1 < A_3$, the physical-edge sequence is reversed to Network 1 $\rightarrow$ Network 2 $\rightarrow$ Network 3. Equal amplitudes produce a predominantly divergent tendency from Network 2 when $\omega_1 < \omega_3$, whereas reversing the frequency ordering generates either convergence toward Network 2 or a sequence directed toward Network 3, depending on the amplitude relation. Across the six tested conditions, reversal of the frequency ordering consistently reverses the Network 1 $\leftrightarrow$ Network 2 asymmetry. In contrast, the signs of the pairwise relations involving Network 3 are primarily associated with the amplitude ordering: Network 3 behaves descriptively as an upstream source for $A_1 > A_3$ and as a receiver for $A_1 \leq A_3$. These observations indicate stimulus-controlled routing rather than a fixed information-flow hierarchy. The Network 1 $\leftrightarrow$ Network 2 pair exhibits the largest normalized directional asymmetry despite having the smallest absolute *TE* values. Conversely, the pairs involving Network 3 exhibit larger raw *TE* values but substantially weaker directional indices. The *TE* magnitude and directional asymmetry therefore quantify different aspects of the pairwise dynamics and must be interpreted jointly. Because no surrogate-based significance test was applied, these results are reported as descriptive predictive tendencies rather than statistically validated information-flow directions.

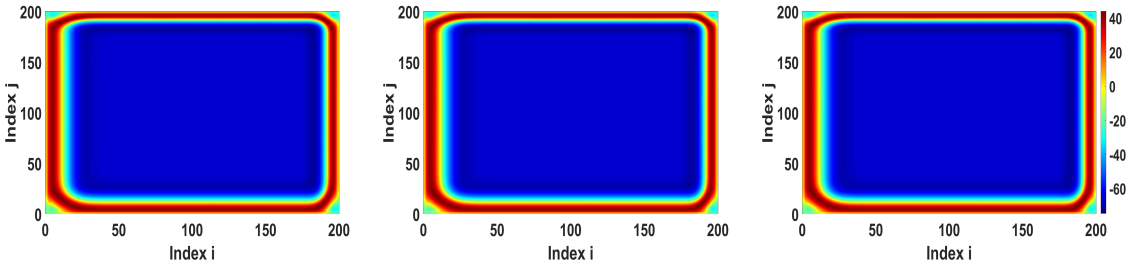


**(a)** Network 1, $t$ = 50 ms. **(b)** Network 2, $t$ = 50 ms. **(c)** Network 3, $t$ = 50 ms.

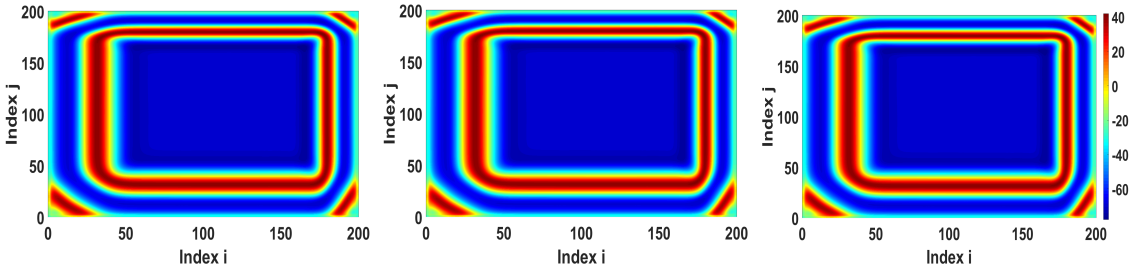


**(d)** Network 1, $t$ = 100 ms. **(e)** Network 2, $t$ = 100 ms. **(f)** Network 3, $t$ = 100 ms.

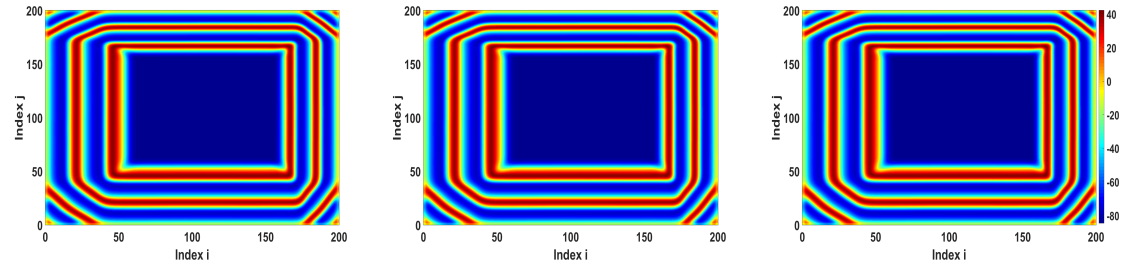


**(g)** Network 1, $t$ = 150 ms. **(h)** Network 2, $t$ = 150 ms. **(i)** Network 3, $t$ = 150 ms.

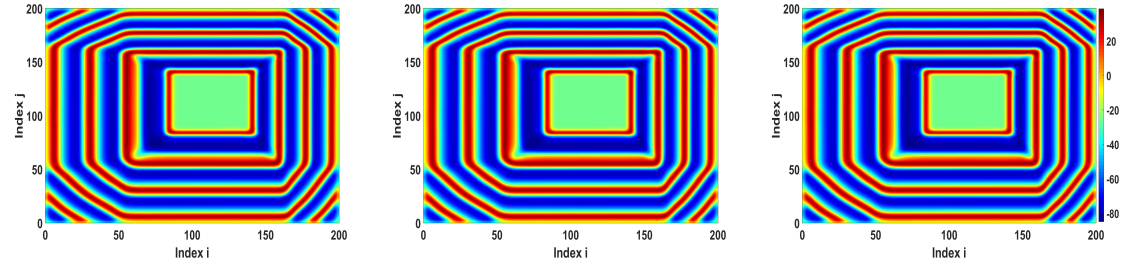


**(j)** Network 1, $t$ = 200 ms. **(k)** Network 2, $t$ = 200 ms. **(l)** Network 3, $t$ = 200 ms.

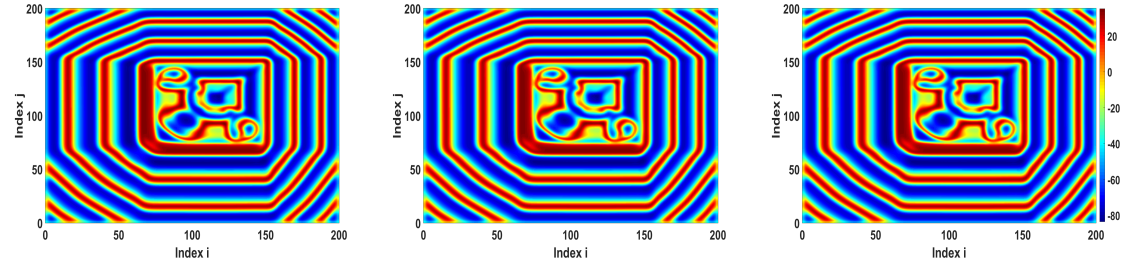


**(m)** Network 1, $t$ = 250 ms. **(n)** Network 2, $t$ = 250 ms. **(o)** Network 3, $t$ = 250 ms.

**Figure 18.** Development of patterns of membrane potential in a network for different time periods with coupling parameter taken in area B. Parameters: $g_E = 0.6$, $g_C = 0.2$, $g_M = 0.3$, $\omega = 10^{-6}\ \mathrm{rad(ms)}^{-1}$, $I$ = 2 mA and $A$ = 4 mA.

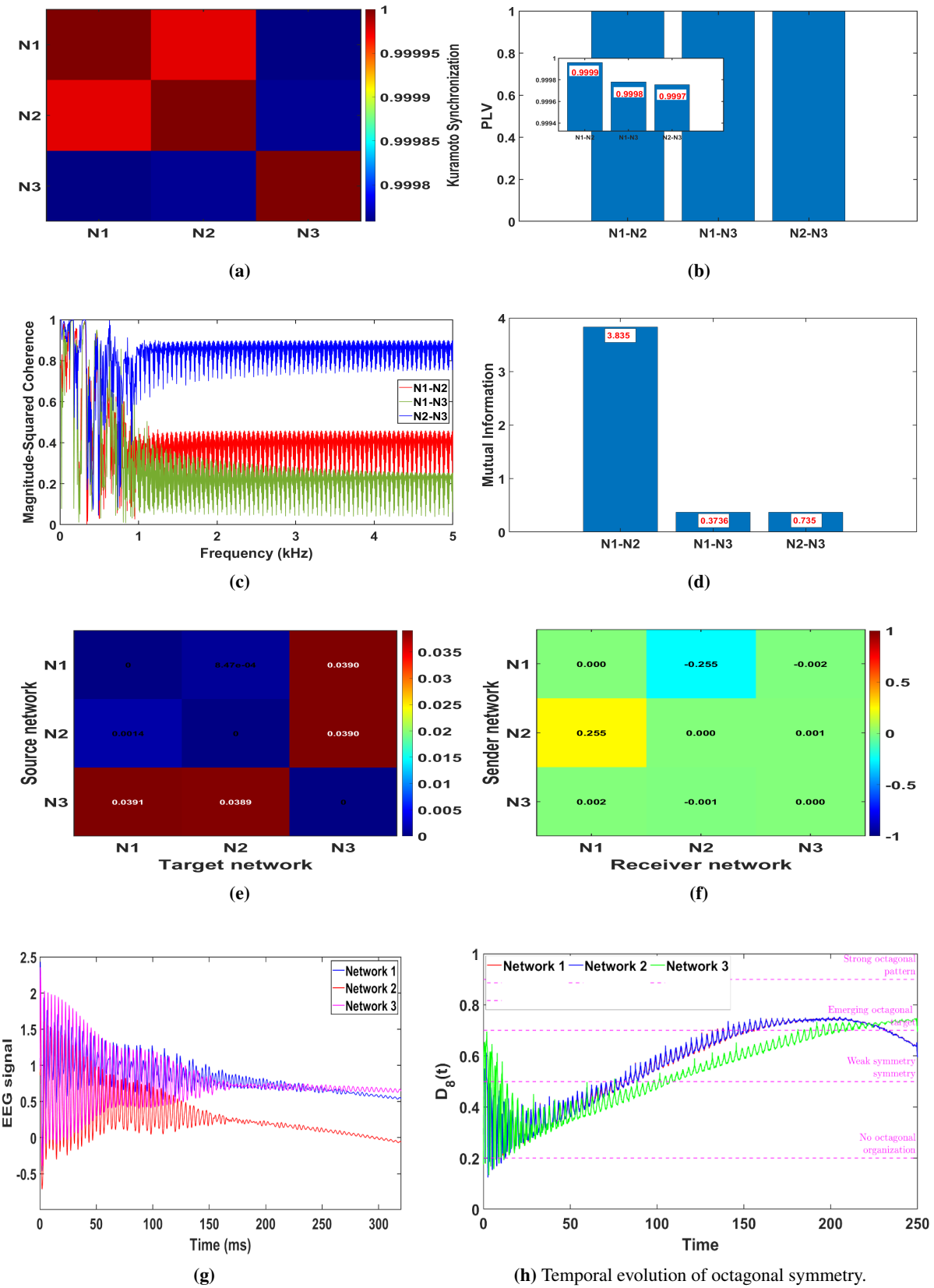


**(a)** **(b)** **(c)** **(d)** **(e)** **(f)** **(g)** **(h)** Temporal evolution of octagonal symmetry.

**Figure 19.** Key metrics illustration for the analysis of Figure 18. (**a**) Kuramoto parameter for inter-network synchronization; (**b**) Phase Locking Value; (**c**) Magnitude Coherence; (**d**) Mutual Information Shared; (**e**) Transfer Entropy (*TE*) with Sender in $y-axis$ and receiver in $x-axis$; (**f**) Normalized Directional Index *NDI*; (**g**) Temporal *EEG*-like population signal of networks and (**h**) $D_8$ illustration for all networks.

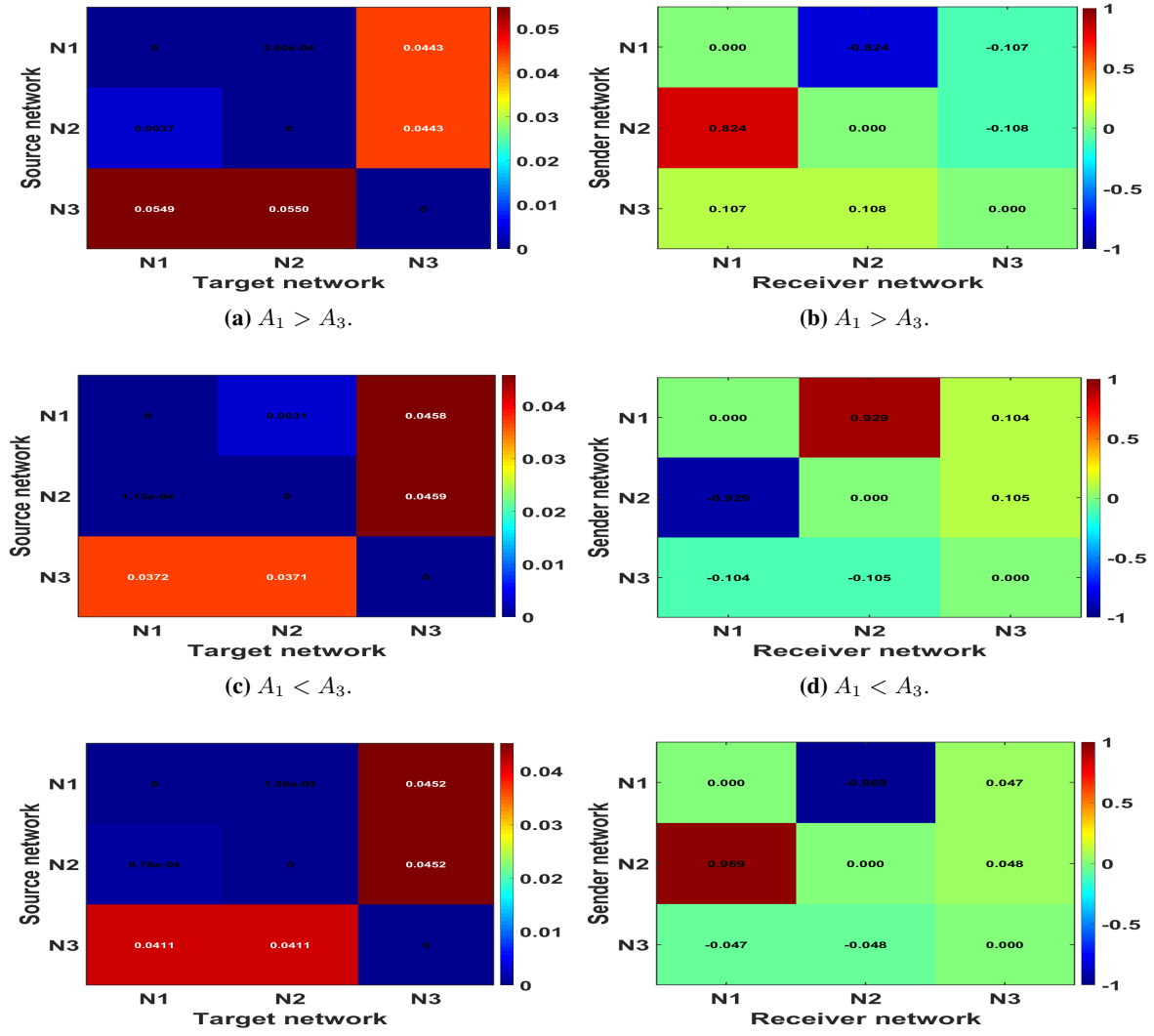


**(a)** $A_1 > A_3$. **(b)** $A_1 > A_3$.

**(c)** $A_1 < A_3$. **(d)** $A_1 < A_3$.

**(e)** $A_1 = A_3$. **(f)** $A_1 = A_3$.

**Figure 20.** Illustration of Transfer Entropy *TE* (**a**,**c**,**e**), and Normalized Directional Index (*NDI*) (**b**,**d**,**f**) for different combination of frequency and amplitude when $\omega_1 < \omega_3$ with $\omega_1 = 10^{-6}$, $\omega_3 = 10^{-4}$. (**a**,**b**) $A_1 = 4$ $A_3 = 2$, Directional hierarchy Network 3 $\rightarrow$ Network 2 $\rightarrow$ Network 1 ; (**c**,**d**) $A_1 = 2$ $A_3 = 4$, Directional hierarchy Network 1 $\rightarrow$ Network 2 $\rightarrow$ Network 3 ; (**e**,**f**) $A_1 = A_3 = 4$, Directional hierarchy Network 1 $\leftarrow$ Network 2 $\rightarrow$ Network 3. Matrix rows represent sender networks and columns represent receiver networks. A positive $NDI_{XY}$ indicates $TE_{X\rightarrow Y} > TE_{Y\rightarrow X}$, whereas a negative value indicates dominance of the reverse direction. Display threshold of detection is 0.01.

The asymmetric, directional information routing emerging from the coupling architecture and the external stimulation, without any plasticity or learning rule, mirrors a feed-forward information processing hierarchy documented in the primate visual and auditory cortical networks, in which sensory information flows from primary cortex to association cortex in a laminar, directional sequence [53,54,105]. Because *TE* values are small ($\approx 10^{-2}$) and no surrogate test was applied, these asymmetries are descriptive and do not by themselves support a directed hierarchy. These asymmetries are compatible with, but do not demonstrate, a hierarchy of directed interactions of the kind inferred from Granger-causality and *TE* analyses of human *EEG* and *fMRI* data [54,176–178].

$$TE = \begin{bmatrix} 0 & TE_{12} & TE_{13} \\ TE_{21} & 0 & TE_{23} \\ TE_{31} & TE_{32} & 0 \end{bmatrix}, \tag{18}$$

and

$$NDI = \begin{bmatrix} 0 & NDI_{12} & NDI_{13} \\ NDI_{21} & 0 & NDI_{23} \\ NDI_{31} & NDI_{32} & 0 \end{bmatrix}. \tag{19}$$

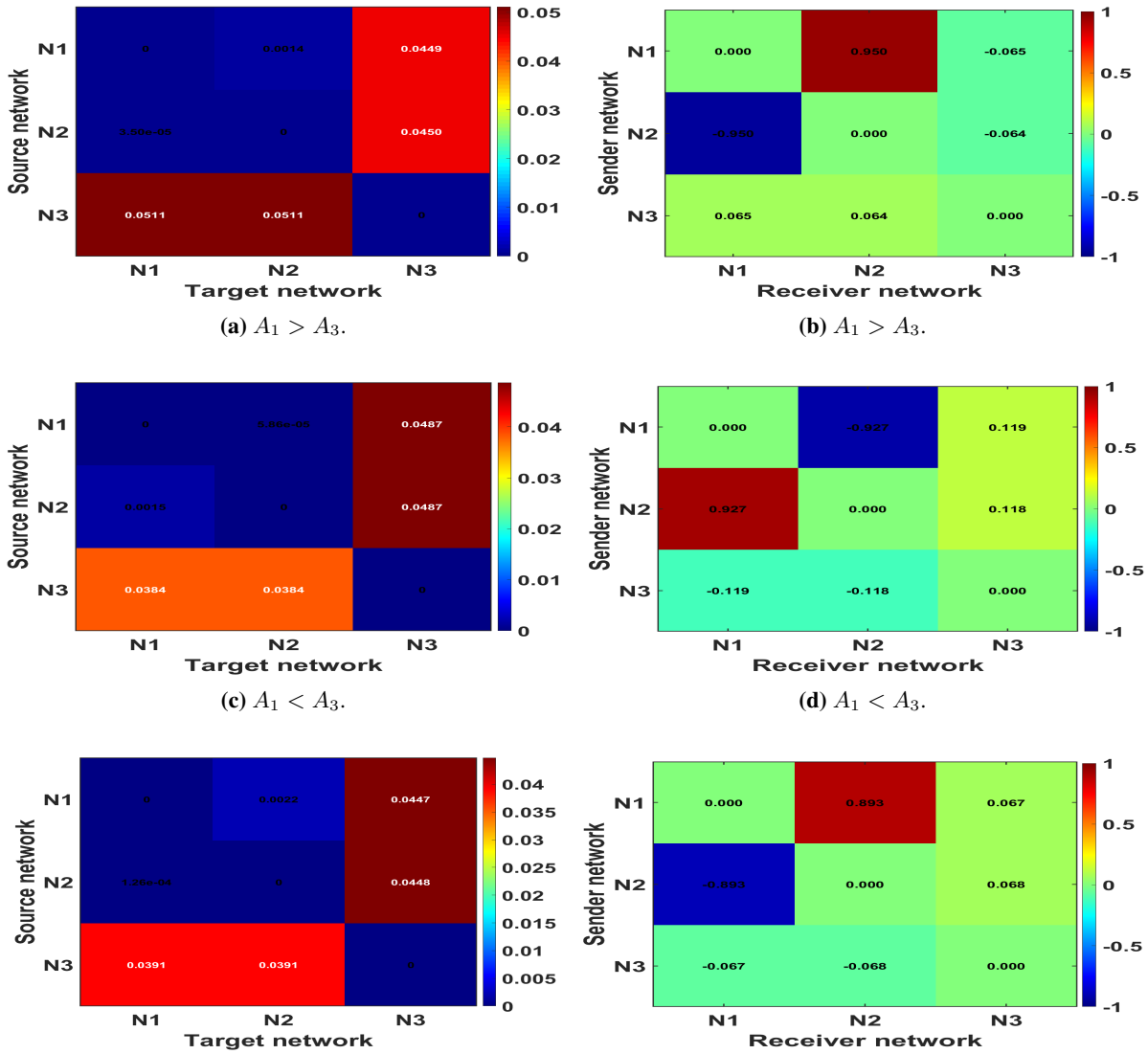


**(a)** $A_1 > A_3$. **(b)** $A_1 > A_3$.

**(c)** $A_1 < A_3$. **(d)** $A_1 < A_3$.

**(e)** $A_1 = A_3$. **(f)** $A_1 = A_3$.

**Figure 21.** Illustration of Transfer Entropy *TE* (**a**,**c**,**e**), and Normalized Directional Index (NDI) (**b**,**d**,**f**) for different combination of frequency and amplitude when $\omega_1 > \omega_3$ with $\omega_1 = 10^{-4}$, $\omega_3 = 10^{-6}$. (**a**,**b**) $A_1 = 4$ $A_3 = 2$, Direction detected Network 1 $\rightarrow$ Network 2 $\leftarrow$ Network 3; (**c**,**d**) $A_1 = 2$ $A_3 = 4$, Direction detected Network 1 $\leftarrow$ Network 2 $\rightarrow$ Network 3; (**e**,**f**) $A_1 = A_3 = 4$. $g_E = 0.6$, $g_C = 0.2$, $g_M = 0.3$, Direction detected Network 1 $\rightarrow$ Network 2 $\rightarrow$ Network 3. A positive $NDI_{XY}$ indicates $TE_{X\rightarrow Y} > TE_{Y\rightarrow X}$, whereas a negative value indicates dominance of the reverse direction. Display threshold of detection is 0.01.

Figure 19g illustrates amplitude of temporal *EEG*-like population signal over the time of the three networks. *EEG*-like population signal amplitude response illustrate sharp transient bursts, when many neurons fire synchronously early in the wave, when neurons are densely packed near corner and modulated amplitude as wave propagates decreasing toward center due to spatial dispersion or asynchronous arrivals. *EEG*-like population signal peak timing shows that we have constant waves speed and coherence. Peak width are weakly broad, which indicate that synchrony is dispersed (clusters). From the corner to the center, we observe progressive reduction of the amplitude of *EEG*-like population signal for all networks indicating the generation of waves with high synchrony that attenuate progressively as they converge toward the center of the array of *(i,j)-plane* of membrane potential as described of the illustration of Figure 18. Figure 19h illustrates temporal evolution of $D_8$ octagonal symmetry index across all three networks across all three networks shows two main outcomes: synchronization of $D_8$ trajectories, confirming that the octagonal wave geometry is preserved coherently across all three networks, and an emergent global structural order arising from purely local coupling. This hierarchical pattern organization shows the same eight-fold wave geometry appearing simultaneously in three spatially distinct network. This is functionally analogous to the cross-regional phase coherence and pattern regularity observed in the human brain

during states of high attentional engagement, in which large-scale cortical networks co-generate synchronized oscillatory patterns across multiple areas simultaneously [105,106]. Notice that the transfer of information between networks is similar to the primate brain, where sensory cortices (primary auditory, visual, or somatosensory areas) receive thalamic input and relay processed signals to higher-order association cortices and prefrontal regions, which in turn coordinate cross-modal integration and executive function [105]. Networks 1 and 3 in our model correspond to such primary sensory areas (receiving direct external drive), while Network 2 corresponds to the integrative hub (driven only indirectly, through inter-network coupling).

**Table 3.** Descriptive classification of raw pairwise *TE* asymmetries across the six tested stimulation conditions of Figures 20 and 21. Direction of arrow indicates network sender to receiver network receiver. The variation $\Delta TE_{k,l} = TE_{kl} - TE_{lk}$, with $(k,l) = 1,2,3$ and $k \neq l$ evaluate difference between two networks and indicate the final direction of how information flow between them. If $TE_{kl} > TE_{lk}$, this shows that show that activity in Network $N_k$ provides predictive information about future activity in Network $N_l$.

| Figure | Architectural Motif 1–2–3 | Complete Peer-to-Peer Order | Interpretation |
|---|---|---|---|
| Figure 20a,b | $N_3 \rightarrow N_2 \rightarrow N_1$ | $N_3 > N_2 > N_1$ | Unilateral hierarchy |
| Figure 20c,d | $N_1 \rightarrow N_2 \rightarrow N_3$ | $N_1 > N_2 > N_3$ | Unilateral hierarchy |
| Figure 20e,f | $N_1 \leftarrow N_2 \rightarrow N_3$ | $N_2 > N_1 > N_3$ | Divergence from the hub |
| Figure 21a,b | $N_1 \rightarrow N_2 \leftarrow N_3$ | $N_3 > N_1 > N_2$ | Convergence toward the hub |
| Figure 21c,d | $N_1 \leftarrow N_2 \rightarrow N_3$ | $N_2 > N_1 > N_3$ | Divergence from the hub |
| Figure 21e,f | $N_1 \rightarrow N_2 \rightarrow N_3$ | $N_1 > N_2 > N_3$ | Unilateral hierarchy |

Observing key patterns like traveling waves or spiral waves of neuronal networks can reveal the transitions occurring during the functioning of different areas of brain where these patterns are observed, mostly during a specific crisis. This is only possible if coherence and synchronization are found in the dynamics appearing at the right time, which involve a good exchanges of information.

## 6. Discussion

The capacity of the brain to coordinate activity across billions of neurons generating the rhythmic, spatially organized wave patterns that underlie perception, memory, motor control, and consciousness remains one of the most deep open questions in neuroscience. In this work, we have investigated the generation and spatiotemporal propagation of collective wave patterns in a complex neuronal network of 200 $\times$ 200 *eHR* neurons with hybrid synaptic coupling under electromagnetic radiation, and extended the analysis to a three-network hub architecture mimicking the inter-regional communication structure of the cerebral cortex. The results, considered together, provide a rich and biologically grounded overview of how local biophysical properties and synaptic connectivity determine the macroscopic dynamical regime of a neuronal population, and how that regime in turn maps onto observable brain states and functions.

The analysis of a single *eHR* neuron under external sinusoidal modulation (Figure 1) demonstrated that the application of a periodic stimulus at sufficiently low frequency ( $\omega = 10^{-1}, 10^{-2}, 10^{-5}$ rad(ms)$^{-1}$) drives a transition from chaotic bursting into rapid, regular spiking a regime characterized by higher instantaneous firing frequency within each burst envelope. This frequency-dependent transition carries a direct neurophysiological interpretation.

Furthermore, a grid structure is considered where a central neuron interact with four neighbors neurons (Figure 4) and is extended to a network of 200 $\times$ 200. When chemical (excitatory and inhibitory) synaptic coupling dominates electrical gap-junction coupling in the single hybrid network ($g_C > g_E$), the network spontaneously generates a rich coexistence of chimera states, localized spiral waves, and spatially inhomogeneous patterns (Figures 5–7). The quantitative metrics phase gradient, winding number (Figure 12a,b), and local order parameter (Figure 12d) confirm that synchronized and desynchronized neuronal domains coexist within the same network, defining signature of chimera states [81,82,116]. This result is of profound neuroscientific relevance. In the human brain, the cerebral cortex contains an estimated 80% excitatory (glutamatergic) and 20% inhibitory (GABAergic) synapses a ratio closely reproduced by our 80:20 excitatory-to-inhibitory chemical coupling partition. The competition between excitatory synchronization and inhibitory desynchronization is precisely the mechanism proposed to underlie chimera-like dynamics in biological neural circuits [116].

Chimera states have been proposed as the dynamical substrate of unihemispheric sleep (in which one hemisphere sleeps while the other remains awake), schizophrenia, and disorders of consciousness such as vegetative and minimally conscious states conditions in which some neural populations are synchronized while others remain

incoherent [81,88]. Our results demonstrate such coexistence within the present deterministic network under selected coupling conditions. They do not establish that the simulated chimera regime corresponds to these dynamical states. These associations remain hypotheses requiring model-specific and experimental validation. However, the present model does not include sleep-stage mechanisms, thalamocortical circuitry, neuromodulatory regulation, or experimentally calibrated sleep frequencies. The observed trajectory should therefore be interpreted as a generic synchronization transition rather than a reproduction of wakefulness, sleep spindles, or deep sleep.

The local order parameter map (Figure 12d) directly visualizes which neuronal sub-populations belong to the coherent domain and which to the incoherent domain, providing a quantity that could in principle be estimated from source-localized *EEG* or *MEG* recordings. The weak spiral wave activity partially located in the map at $t = 2000, 3000$, and $5000$ ms (Figure 5d,e,f) is particularly relevant to epilepsy research: in vivo voltage-sensitive dye and *ECoG* recordings have demonstrated that ictal wavefronts can organize as rotating spiral waves during focal seizures [37,38,117], and that the self-sustaining rotation of these spirals around a phase singularity (the spiral tip, identified here by the winding number $n$) is a key mechanism of seizure maintenance. The winding-number map in Figure 7b for the specific period of $t = 2000$ ms is dominated by zero-winding plaquettes, shown by the green background. Multiple localized positive and negative winding candidates $q = \pm 1$ are detected throughout the domain, which involves that the net topological charge is $Q(t) = \sum_p q_p(t) \simeq 0$, and must not be interpreted as evidence that the phase field contains no local singularities, and at the same time not confirm evidence of spiral wave. Our finding that spiral cores emerge spontaneously from the competition between excitatory and inhibitory (*E/I*) chemical coupling without requiring any structural heterogeneity in the network suggests that the intrinsic *E/I* imbalance of a cortical circuit is sufficient to seed persistent spiral-like activity, even in an otherwise homogeneous network. This has direct implications for understanding how focal seizures initiate in structurally normal tissue. We have mentioned that previous investigations have demonstrated spiral waves, chimera states, target waves, and synchronization transitions in neuronal systems subjected to electromagnetic induction. The present results should therefore not be interpreted as the first numerical observation of these individual phenomena. The contribution lies instead in their joint investigation within one large two-dimensional eHR lattice with hybrid electrical and excitatory–inhibitory chemical coupling. Compared with studies based on one-dimensional FitzHugh–Nagumo chains or purely electrical multilayer networks, the present framework combines richer single-neuron bursting dynamics, directed chemical transmission, electrical diffusion, and electromagnetic feedback. Moreover, the patterns are evaluated using a common quantitative framework involving phase gradients, topological singularities, local coherence, orientational order, and population-level synchronization. The *EEG*-like population signal associated with the chimera-wave coexistence regime (Figure 10) shows initially high amplitude reflecting the strong initial synchrony as wave seeds are established followed by progressive amplitude reduction as the network evolves toward spatially fragmented activity. This temporal trajectory is closely parallels the clinical *EEG* signature of seizure onset and termination: a high amplitude, high synchrony ictal discharge that gradually desynchronizes as the cortex returns to its baseline low-amplitude, high-frequency state [57–59]. However, the actual analysis of different states inside a single dynamics over the time only consider theoretical computation without considering robust clinical issue for real seizure mechanism.

When electrical gap junction coupling dominates chemical coupling ($g_E > g_C$), the network self-organizes into concentric square target waves propagating outward from multiple corner-initiated sources (Figures 8 and 9). The quantitative characterization confirms this interpretation: the radial phase gradient (Figure 12e) verifies outward propagation from source sites, the absence of winding number singularities (Figure 12b) excludes spiral wave cores, and the eight-fold ($D_8$) symmetry index (Figure 9 and Algorithm 1) captures the lattice-geometry-imposed octagonal propagation pattern. The occurrence of persistent spiral-like activity is relevant to the general study of excitable media because rotating waves have also been observed in several experimental and computational investigations of epileptiform propagation. In the present model, however, the winding number characterizes only the topology of the simulated phase field. It does not constitute a diagnostic marker of epilepsy. This finding of spiral-like population carries two major brain-relevant implications. First, concentric target waves in biological excitable media are the signature of a central pacemaker source driving periodic wavefronts outward into surrounding tissue. In the brain, the thalamo-cortical system operates precisely as such a pacemaker: thalamic nuclei generate rhythmic theta and alpha oscillations that propagate as expanding wavefronts into the overlying cortical layers, structuring the brain's resting-state alpha rhythm [13,18]. Our result that electrical coupling dominance in a homogeneous network is sufficient to generate stable, periodic, outward-propagating target waves suggests that the gap-junction connectivity prevalent in thalamic relay networks and cortical layer IV is a key determinant of pacemaker-driven wave propagation. The phase velocity characterization (Figure 12 radial gradient analysis) further shows that wave speed is constant across propagation fronts, consistent with the experimentally measured constant propagation speeds

of alpha and sleep spindle waves in the human cortex [55,56]. Secondly, the square geometry of the propagating wavefronts arising from the discrete lattice structure of the network rather than isotropic diffusion directly mirrors the anisotropic wave propagation observed in cortical tissue, where the columnar microarchitecture and the orientation of cortical layers impose preferred propagation axes on traveling waves [1]. The wave regimes obtained in our model may be used to formulate hypotheses about how coupling composition, external modulation, and spatial topology influence collective neuronal dynamics. Traveling and target-like waves may provide computational analogues of coordinated activity propagation, whereas spiral-like and chimera-like states illustrate how localized rotation or partial coherence can emerge in nonlinear neuronal media. Similar classes of patterns have been discussed in relation to sensory processing, sleep, epilepsy, and other brain states. Nevertheless, similarity at the level of wave geometry or population synchrony does not establish equivalence at the physiological or clinical level. The current model contains identical neurons, regular nearest-neighbor connectivity, phenomenological electromagnetic feedback, and no disease-specific or behavior-related variables. Consequently, the neurological interpretations presented here should be understood as qualitative hypotheses for future experimental investigation.

**Algorithm 1:** Step to compute $D_8$ index and octagon detection

1: Compute *FFT* and Frequency Filtering
- Compute *2D FFT* of membrane potential $V(x, y, t) \rightarrow \tilde{V}(k_x, k_y, \omega)$.
- Extract two frequency shells:
  Shell 1: $\mid k \mid \approx k_1$ (fundamental),
  Shell 2: $\mid k \mid \approx k_2$ where $k_2/k_1 \approx 8$,
- Isolate complex amplitude on each shell: $A_1(\theta)e^{i\phi_1(\theta)}, A_2(\theta)e^{i\phi_2(\theta)}$.

2: Phase Extraction
- Compute angular phase: $\Phi_1(\theta) = \arg(A_1(\theta))$ and $\Phi_2(\theta) = \arg(A_2(\theta))$.
- Compute relative phase: $\Delta\Phi(\theta) = \Phi_2(\theta) - 8\Phi_1(\theta) \pmod{2\pi}$

3: Compute Phase Gradient $\nabla_\theta \Delta\Phi(\theta)$, use finite difference: $\dfrac{\Delta\Phi(\theta+1) - \Delta\Phi(\theta-1)}{2\Delta\theta}$.

4: $D_8$ Symmetry Index Calculation with Fourier harmonic method
- Compute Fourier series of $e^{i\Delta\Phi(\theta)}$.

$$C_n = \frac{1}{2\pi}\int_0^{2\pi} e^{i\Delta\Phi(\theta)}e^{-in\theta}d\theta$$

- For $n = 8$, magnitude of $8^{\text{th}}$ harmonic: $|C_8|$.
- Compute Normalized $D_8$ index:

$$D_8 = \frac{|C_8|}{\sum_{k=1}^{8}|C_k|}$$

5: Compute Angular Spectrum
- Compute the power:

$$p(n) = \mid C_n \mid^2$$

- Check the peak at *n* = *8*.

6: Phase Velocity Lobes

7: Phase velocity: $v_\Phi(\theta) = \dfrac{\omega_2}{\mid \nabla_\theta \Delta\Phi(\theta) \mid}$

8: Plot $v_\Phi(\theta)$ versus $\theta$

9: Octagon detection. 8 distinct lobes (maxima in $v_\Phi$) at $\theta_k = k\pi/4$, $k = 0, \ldots, 7$.

10: **if** $D_8 \geq 0.7$ **then**

11: Octagon Detected $\rightarrow$ TRUE

12: **else if** $D_8 < 0.7$ **then**

13: Octagon Detected $\rightarrow$ FALSE

14: **end if**

The $D_8$ symmetry index introduced in this work provides a novel quantitative tool for detecting and measuring this anisotropy in both computational and experimental data: applied to multichannel *EEG* or *ECoG* recordings, this index could identify whether the propagation of a given brain oscillation is isotropic (consistent with diffuse cortical activation) or anisotropic (consistent with structurally constrained, directional wave propagation). The *EEG*-like population signal amplitude profile associated with target wave propagation (Figure 11) shows progressive attenuation from the corners toward the center, reflecting the spatial dispersion and arrival-time spread of the wavefronts a pattern directly analogous to the amplitude gradient of traveling alpha waves measured across the scalp [13,14]. The *EEG*-like population signal frequency spectrum (Figure 11) further confirms the stability of the oscillation frequency across the propagation episode, consistent with a pacemaker-driven rather than resonance-driven wave mechanism. Across all single-network coupling regimes, the Synchronization Factor (*SF*) and Synchronization Error (*SE*) metrics (Figure 15) provided a time-resolved measure of the network's collective synchrony. The temporal evolution of *SF* and *SE* reveals that the network traverses a sequence of distinct dynamical states from initial desynchronization through transient chimera formation to steady-state wave propagation a trajectory that closely parallels the *EEG* amplitude changes observed during the cortical transition from wakefulness into non-REM sleep.

We indicate that the index $D_8$ used in our study quantifies the magnitude of the eighth angular harmonic of the spatial activity distribution. It's interpreted as an eight-fold rotational anisotropy descriptor rather than, by itself, as proof of full dihedral symmetry. In particular, a fourfold pattern may also generates a non-zero or even large eighth harmonic. The square lattice used in the present simulations imposes an intrinsic fourfold anisotropy. The observed eighth-order component contain contributions from both the network geometry and the collective dynamics. On triangular or hexagonal lattices, a sixth-order component for instance is expected to become more prominent, whereas geometric disorder and spatially heterogeneous coupling should broaden the angular peaks and reduce the global value of $D_8$. A large value of $D_8$ can therefore be regarded as evidence of a robust eight-fold component only when it exceeds the corresponding surrogate distribution or a known threshold, remains dominant, and is supported by eight approximately equally spaced angular maxima. Direct application to experimental *EEG* or *ECoG* requires additional precautions. *EEG* is affected by volume conduction, irregular electrode sampling, referencing, and distortion caused by projecting the curved head surface onto a plane. *ECoG* provides improved spatial resolution but is generally limited to partial and non-uniform cortical coverage. For these datasets, the index should be estimated using the actual sensor coordinates or subject-specific cortical geometry, accompanied by spatial-sampling surrogates, channel-removal tests, and confidence intervals. Until such validation is performed, $D_8$ should be regarded as an exploratory descriptor of spatial anisotropy rather than a stand-alone physiological or clinical biomarker.

The extension to the three-network architecture (Figure 16) constitutes the most directly brain relevant outcome of this work and provides an additional level of analysis by examining the preservation of wave geometry and synchronization across interacting populations. The configuration in which two peripheral networks (Networks 1 & 3) receive independent external sinusoidal stimulation and drive a central hub network (Network 2) through combined electrical and magnetic inter-network coupling maps directly onto the hierarchical organization of the cerebral cortex. Its novelty concerns the architecture and combined analysis rather than the first use of transfer entropy or phase locking in neuronal systems. The results obtained at high inter-network coupling (area B, Figure 17) help to select appropriated coupling parameters $(g_C, g_E, g_M)$ for synchronized exchanges. In each networks analyzed, the initial wave birth is followed by progressive destabilization into random or chaotic patterns as networks begin to interact (Figure 18), by using coupling parameters in area B. The inter-network Kuramoto synchronization matrix (Figure 19a) shows $R_{lk} \to 1$ for all network pairs, confirming global inter-regional phase coherence directly analogous to the large-scale gamma-band synchrony observed between cortical areas during sensory binding, working memory maintenance, and conscious awareness [105,106]. The Phase Locking Value ($PLV \approx 0.997 - 0.999$ across all pairs, Figure 19b) confirms that the three networks maintain stable, frequency-locked oscillatory relationships throughout the simulation a result consistent with the high *PLV* values documented between cortical areas engaged in coordinated sensorimotor tasks [179–181]. The high Kuramoto-order and *PLV* values indicate stable phase relationships among the simulated network-level signals. Such inter-population synchronization is often discussed as a possible mechanism for neural integration, but synchronization alone does not demonstrate perception, attention, memory, sensory binding, or conscious awareness. The high *EEG*-like population signal coherence across all three networks (Figure 19c) and the high shared information (Figure 19d) together indicate that the peripheral stimulation, once relayed through the inter-network coupling, produces nearly identical macroscopic oscillatory signatures in all three regions, a computational analogue of the phenomenon of cortical entrainment, in which rhythmic sensory stimulation (visual flicker, auditory beat) drives synchronized oscillations across large cortical territories [115].

The Transfer Entropy and Directional Index analyzed reveals one of the most significant result of the three-network study. The directed hierarchy of information flow depends on the stimulation parameters of frequency-amplitude of the external stimulation. In Figures 19e,f, identical values of frequency and amplitude is considered and it shows a Convergence toward the hub Network 1 $\rightarrow$ Network 2 $\leftarrow$ Network 3. In Figures 20 and 21, six frequency-amplitude conditions are analyzed and the observation show that we may have unilateral hierarchy, Convergence toward the hub or Divergence from the hub as summarized in Table 3. However, additional statistical analysis can better validated biological plausible.

The temporal evolution of the $D_8$ octagonal symmetry index across all three networks (Figure 19h) shows synchronized $D_8$ trajectories, confirming that the octagonal wave geometry is preserved coherently across all networks. This coherent transfer of the anisotropic wave geometry across the three-network architecture suggests that the $D_8$ symmetry, while originating from the local lattice topology, is descriptive directional tendency to inter-network coupling and propagates as a global organizational feature. Importantly, the specific resonance condition $\Omega_2/\Omega_1 \approx 8$ that generates the octagonal pattern in each network is preserved across the hub architecture, indicating that the inter-network electrical and magnetic coupling does not disrupt the phase-locking mechanism but rather reinforces it through cross-network constructive interference. The temporal evolution of the $D_8$ octagonal symmetry index across all three networks (Figure 19h) shows synchronized $D_8$ trajectories, confirming that the octagonal wave geometry is preserved coherently across all networks.

## 7. Conclusions

Taken together, the results of this study establish several general principles with broad implications for computational and clinical neuroscience. Synaptic balance as a pattern selector, which suggests neurological conditions associated with synaptic imbalance, like in the case of epilepsy (excess excitation), schizophrenia (*E/I* imbalance), and autism spectrum disorder (altered gap-junction connectivity) which may be understood in part as shifts between the wave pattern regimes identified in this work. The present study establishes model-specific relationships among hybrid synaptic coupling, external modulation, lattice geometry, and collective wave organization. Considering *EMR* as a neuromodulator provides a theoretical framework for understanding both the neural effects of environmental electromagnetic exposure and the therapeutic mechanisms of non-invasive brain stimulation techniques (*TMS*, *tACS*, *tDCS*) [115]. The four pattern types identified, traveling waves, spiral waves, target waves, and chimera states do not represent distinct pathological or healthy states in isolation, but rather a continuum of dynamical regimes that the brain navigates in response to changing internal (synaptic, modulatory) and external (sensory, electromagnetic) conditions. The observed regimes provide computational examples of distinct forms of spatiotemporal organization. Their resemblance to patterns reported in experimental neuroscience motivates further investigation but does not demonstrate specific mechanisms of sleep, cognition, epilepsy, or neurodegenerative disease.

The octagonal symmetry index introduced in this work is a potentially generalization tool for quantifying anisotropic wave propagation in cortical recordings, and its temporal evolution could serve as a exploratory descriptor of cortical state transitions in clinical *EEG* monitoring. The physical basis of this index rooted in the square lattice geometry and the resonance condition $\Omega_2/\Omega_1 \approx 8$ provides a mechanistic interpretation of why certain cortical areas exhibit directional propagation biases. The network architecture analyzed in this work cannot directly explain the complexity of biological brain-network exchange, but it describes potential mechanism and behavior for specific cases. The three-network analysis does not reveal a unique information-flow hierarchy. Instead, the raw *TE* and *NDI* results suggest that the relative frequency and amplitude of the peripheral inputs reconfigure the apparent direction of pairwise predictive information. Depending on the tested condition, the structural pathway exhibits serial propagation, convergence toward the central network, or divergence from it. Notice also that more trials can be performed through inter-network coupling, weak, intermediate and strong. However, our analysis already reveal that these trials can also affect the direction of information flow. In the brain, these coupling are regulated through chemical reaction of neurotransmitters (Glutamate ,GABA , Dopamine and others), and that regulation can significantly affected information flow.

Several important directions remain open for future investigation. The incorporation of synaptic plasticity (spike-timing-dependent plasticity, *STDP*) into the network coupling rules would allow the wave patterns to evolve with experience, providing a model for how memory consolidation and learning reshape the spatial organization of cortical oscillations. The use of heterogeneous coupling with spatially varying $g_E/g_C$ ratios mimicking the laminar variation of gap-junction and chemical synapse density across cortical layers could reproduce the layer-specific wave propagation observed experimentally. Extension of the three-network architecture to larger hub-spoke configurations would enable modeling of full-scale resting-state network dynamics and could be validated against functional

connectivity data from human *fMRI* and *EEG*. Finally, the integration of noise models with biologically realistic noise spectra (Poisson shot noise from spontaneous synaptic release) would bring the model closer to the stochastic dynamics of real cortical tissue and allow direct comparison with experimental recordings. Future work should include heterogeneous neuronal populations, physiologically calibrated time scales, conduction delays, anatomical connectivity, and electrophysiological forward models.

## Author Contributions

A.B.A.: writing original draft preparation, conceptualization of the study, analysis, validation, methodology, software; E.B.M.N.: supervision, revision, analysis, validation; C.T.N.: analysis, validation; T.F.F.: supervision, validation; Z.T.N.: supervision, revision, validation; H.B.F.: supervision, validation. All authors have read and agreed to the published version of the manuscript.

## Funding

This research received no external funding.

## Institutional Review Board Statement

Not applicable. This study was entirely theoretical and computational and did not involve human participants, human-derived data, animals, or biological specimens.

## Informed Consent Statement

Not applicable. This study did not involve human participants, patients, human-derived data, or identifiable personal information.

## Data Availability Statement

Data will be made available on request.

## Acknowledgments

The authors thank the anonymous reviewers for their constructive comments.

## Conflicts of Interest

The authors declare no conflict of interest.

## Use of AI and AI-Assisted Technologies

No AI tools were utilized for this paper.

## Appendix A. Mathematical Tools and Methods for the Global Analysis

### *Appendix A.1. Calculus of Hybrid Synaptic Model for Membrane Potential*

Figure 4 defined a star configuration of how central presynaptic node $(i, j)$ interacts with 4 neighbors postsynaptic nodes $(i-1, j)$, $(i, j-1)$, $(i+1, j)$ and $(i, j+1)$. Equation (2) indicates mathematical expression of electrical connection between presynaptic and postsynamptic node. Hence, by considering contribution of neighbors nodes, and the fact that coupling strength is uniform, expression of total electrical current is given by Equation (A1).

$$I_{elect}(i,j) = g_E\big(x_{(i-1,j)} - x_{(i,j)}\big) + g_E\big(x_{(i,j-1)} - x_{(i,j)}\big) + g_E\big(x_{(i+1,j)} - x_{(i,j)}\big) + g_E\big(x_{(i,j+1)} - x_{(i,j)}\big). \quad \text{(A1)}$$

After expanding Equation (A1), we obtain Equation (A2).

$$I_{elect}(i,j) = \quad g_E\Big(x_{(i+1,j)} + x_{(i-1,j)} + x_{(i,j+1)} + x_{(i,j-1)} - 4x_{(i,j)}\Big). \quad \text{(A2)}$$

Equations (3) and (4) indicate mathematical expressions of chemical connection. Similarly, total contribution of neighbors nodes can be found.

$$\begin{aligned} I_{chem}(i,j) = g_C R'_{(i,j)}(t)\Big(E_{\text{rev}} - x_{(i,j+1)}\Big) + g_C R'_{(i,j)}(t)\Big(E_{\text{rev}} - x_{(i,j-1)}\Big) \\ + g_C R'_{(i,j)}(t)\Big(E_{\text{rev}} - x_{(i-1,j)}\Big) + g_C R'_{(i,j)}(t)\Big(E_{\text{rev}} - x_{(i+1,j)}\Big) \end{aligned} \tag{A3}$$

Expanding Equation (A3), we have

$$I_{chem}(i,j) = \quad g_C R'_{(i,j)}(t)\Big[4E_{rev} - \Big(x_{(i,j+1)} + x_{(i,j-1)} + x_{(i-1,j)} + x_{(i+1,j)}\Big)\Big]. \tag{A4}$$

Thus for inhibitory and excitatory behavior of chemical coupling, we have Equations (A5) and (A6) respectively.

$$I^{inh}_{chem}(i,j) = g^{inh}_C R'_{(i,j)}\Big[4E^{inh}_{rev} - \Big(x_{(i,j+1)} + x_{(i,j-1)} + x_{(i-1,j)} + x_{(i+1,j)}\Big)\Big], \tag{A5}$$

and

$$I^{exc}_{chem}(i,j) = g^{exc}_C R'_{(i,j)}\Big[4E^{exc}_{rev} - \Big(x_{(i,j+1)} + x_{(i,j-1)} + x_{(i-1,j)} + x_{(i+1,j)}\Big)\Big]. \tag{A6}$$

Add Equations (A5) and (A6), we obtain expression of total chemical synapse $I_{chem}(total)$ given by Equation (A7)

$$I_{chem}(i,j) = I^{inh}_{chem}(i,j) + I^{exc}_{chem}(i,j). \tag{A7}$$

This summation is rewritten and given by Equation (A8).

$$I_{chem}(i,j) = R'_{(i,j)}\Big[4\Big(g^{\text{inh}}_C E^{\text{inh}}_{\text{rev}} + g^{\text{exc}}_C E^{\text{exc}}_{\text{rev}}\Big) - \Big(g^{\text{inh}}_C + g^{\text{exc}}_C\Big)\Big(x_{(i,j+1)} + x_{(i,j-1)} + x_{(i-1,j)} + x_{(i+1,j)}\Big)\Big] \tag{A8}$$

*Appendix A.2. 8-Fold Spatial Symmetry*

An octagon corresponds to an 8-fold spatial symmetry, often emerges when the network develops eight preferred propagation directions, corresponding to a phase $\theta_k = k\frac{\pi}{4}$, with $k = 0, 1, \cdots, 7$. The location in a plane are approximately known, East, Northeast, North, Northwest, West, Southwest, South and Southeast. Under *EM* radiation and sinusoidal forcing, higher harmonics appear and we have sequence of frequencies $f$, $2f$, $3f$, and $4f$, where $f$ is the resonant frequency of the global network. The octagonal target-ring pattern is characterized by (i) a dominant spectral resonance satisfying $\frac{\Omega_2}{\Omega_1} \approx 8$, where $\Omega_2$ and $\Omega_1$ are associated to the frequency of *EM* and sinusoidal input signal; (ii) an eight-fold angular modulation of the phase-gradient field quantified by the symmetry index $D_8 = \left|\langle e^{i8\theta}\rangle\right|$; The range of $D_8$ are detailed in Table A2; and (iii) an eight-lobed phase-velocity distribution. Together these metrics demonstrate the emergence of a resonant $D_8$-symmetric propagating mode induced by the interaction between electromagnetic coupling and sinusoidal forcing.

*Appendix A.3. Key Quantitative Metrics for Spatiotemporal Pattern Characterization*

Spatiotemporal wave patterns are widely observed in neuronal systems, oscillatory media, reaction-diffusion systems, *EEG/LFP* recordings, and coupled oscillator networks. Important dynamical patterns include: Traveling waves, spiral waves, target waves, chimera states. To characterize these patterns quantitatively, several mathematical descriptors are commonly used: Phase gradient and phase velocity for traveling waves, phase singularities, winding number for spiral waves, local order parameter and Kuramoto order parameter.

Appendix A.3.1. Instantaneous Phase Extraction

Most quantifiers are based on the instantaneous phase field $\phi(t)$ obtained from neuronal activity signals such as membrane potentials, *EEG*, or *LFP*. Using the Hilbert transform of Equation (A9), where $s(t)$ is the original signal and, $\mathcal{H}[s(t)]$ is the Hilbert transform. The instantaneous phase is given by Equation (A10).

$$z(t) = s(t) + i\mathcal{H}[s(t)]. \tag{A9}$$

$$\phi(t) = \arg(z(t)). \tag{A10}$$

Appendix A.3.2. Traveling Waves

Traveling waves correspond to coherent propagation of activity across the network. Typical characteristics by Parallel wavefronts, Stable propagation direction and Spatial coherence. The phase gradient is defined by Equation (A11), and helping to characterizes the propagation direction where a parallel gradient vectors indicate coherent traveling waves; The Spatial coherence where smooth gradients imply stable propagation, and irregular gradients indicate fragmentation or turbulence; The wavelength with the magnitude given by $|\nabla\phi|$, is inversely related to wavelength, where the large gradients correspond to shorter wavelengths.

$$\nabla\phi = \left(\frac{\partial\phi}{\partial x}, \frac{\partial\phi}{\partial y}\right) \tag{A11}$$

The phase velocity is defined by Equation (A12).

$$v_p = \frac{\omega}{|\nabla\phi|}. \tag{A12}$$

where $\omega = \frac{\partial\phi}{\partial t}$. Phase velocity characterizes: The Propagation Speed where the high velocity indicates rapid information transmission and the low velocity indicates slow cortical waves; The wave stability, where uniform velocity indicates stable traveling waves and, velocity fluctuations indicate disturbances or instability; The information transport to transport neuronal information and the velocity reflects communication efficiency.

Appendix A.3.3. Spiral Waves

Spiral waves are rotating wave structures centered around a phase singularity. They are frequently observed in epileptic dynamics, cardiac fibrillation or cortical turbulence. In spiral waves, the phase gradient rotates continuously around the spiral core, the gradient vectors form circular structures, near the spiral core the curvature becomes very large, and spiral waves exhibit rotational phase organization. The phase singularities and the winding Number given by Equation (A13) indicates spiral core detection where nonzero winding numbers identify phase singularities, rotation direction where $n = +1$ indicates counterclockwise rotation and $n = -1$ indicates clockwise rotation. Numerous singularities indicate turbulent activity.

$$n = \frac{1}{2\pi}\oint \nabla\phi \cdot d\mathbf{l}. \tag{A13}$$

Appendix A.3.4. Target Waves

Target waves are concentric wavefronts generated by a pacemaker source. The typical features are a circular symmetry,an outward radial propagation and a stable wave emission. The phase gradient points radially outward revealing the source center, characterizes wave spreading, and the symmetric gradients indicate isotropic propagation. The phase velocity characterizes radial propagation speed and the efficiency of radial communication. The faster velocities indicate highly excitable media and the constant velocities indicate stable oscillatory sources.

Appendix A.3.5. Chimera States

Chimera states correspond to coexistence of the synchronized regions and the desynchronized regions within the same network. The local order in a two-dimensional parameter given by Equation (A14), where $N_j$ and $N_k$ are the local neighborhood and $\phi_k$ are neighboring phases. $Z_{jk} \approx 1$ indicates strong synchronization, while $Z_{jk} \approx 0$ indicates incoherent activity. The coexistence of high and low values identifies chimera states. The local order parameter reveals transitions between coherent and incoherent regions.

$$Z_{jk} = \left| \frac{1}{N_j}\frac{1}{N_k} \sum_{n\in N_j} \sum_{m\in N_k} e^{i\phi_{n,m}} \right| \tag{A14}$$

Appendix A.3.6. Topological Detection of a Spiral Core

For each elementary $2 \times 2$ plaquette $p$, the discrete winding number is computed by following its four vertices counterclockwise:

$$q_p(t) = \frac{1}{2\pi}\sum_{m=1}^{4} \mathrm{wrap}[\phi_{m+1}(t) - \phi_m(t)], \qquad \phi_5 \equiv \phi_1. \tag{A15}$$

A plaquette is classified as a core candidate when its winding is within $\varepsilon_q = 0.20$ of $+1$ or $-1$; equivalently,

$$|q_p(t) - \mathrm{round}(q_p(t))| \le 0.20, \qquad |\mathrm{round}(q_p(t))| = 1. \tag{A16}$$

Adjacent candidate plaquettes are merged into one core, and detections within two lattice sites of the boundary are excluded to reduce boundary artefacts. Successive detections with the same topological charge are linked into a core trajectory when their displacement is no more than five lattice sites per analyzed frame; one missing frame may be bridged.

### *Appendix A.4. Persistence Decision*

Let $I_{\mathrm{sp}} = [3000 - 5000]$ ms denote the late-time interval highlighted by the present Figure 5. If the available simulation ends at 4000 ms, the corresponding interval must be shortened explicitly (for example, $[3000 - 4000]$ ms); no result should be extrapolated to 5000 ms. For a tracked core $k$, define

$$P_{\mathrm{core}}^{(k)} = \frac{1}{N_{\mathrm{sp}}} \sum_{t_n \in I_{\mathrm{sp}}} \mathbf{1}(k \text{ is detected at } t_n), \qquad P_{\mathrm{core}} = \max_k P_{\mathrm{core}}^{(k)}. \tag{A17}$$

The pattern is classified as a persistent spiral-wave regime only if all of the following conditions are met:

(1) a dominant core with charge $q = +1$ or $q = -1$ is detected in at least $90\%$ of the analyzed frames in $I_{\mathrm{sp}}$, i.e. $P_{\mathrm{core}} \ge 0.90$;
(2) the sign of the dominant core is conserved and the net topological charge does not exhibit repeated, unresolved sign reversals;
(3) the tracked core remains inside the domain and its trajectory is bounded. As a practical diagnostic, report its root-mean-square displacement normalized by the smaller lattice dimension, $d_{\mathrm{rms}}/\min(N_x, N_y)$; a value below approximately $0.10$ supports a localized core, although this displacement is reported rather than used as a universal cutoff;
(4) phase fronts rotate continuously around the detected singularity. A nonzero winding number without surrounding rotational propagation is not sufficient; and
(5) the conclusion is reproducible across the five independent initializations. Report every run separately and the success fraction. A useful robustness rule is that at least four of five runs satisfy the complete criterion.

The stronger term stable spiral attractor should be used only if the late-time regime is also invariant under a longer integration, modest perturbations, and different initial conditions. Without those additional tests, persistent spiral-wave regime is the defensible term.

### *Appendix A.5. Direct Relationship to the Spatial Figures*

Figure 5e,f,k,l, at $t = 3000$ and $5000$ ms, contains the visual candidates for a late spiral regime. The proposed test replaces the inference from these four images by a frame-by-frame demonstration: a winding map is calculated at every stored time, the same signed core is tracked, and its residence and trajectory are displayed. A revised metric figure should therefore contain $N_{\mathrm{core}}(t)$, the net charge $Q(t) = \sum_p q_p(t)$, the dominant-core trajectory, and the core-residence map over $I_{\mathrm{sp}}$.

The present Figure 6 is evaluated at $t = 100$ ms with $g_C = 1.5$, whereas Figure 7 is evaluated at $t = 2000$ ms with $g_C = 6$. Because both time and coupling strength change, these two figures cannot be treated as successive stages of one trajectory. For a valid temporal comparison, the metrics must be recomputed at all relevant times for each fixed parameter set separately. Furthermore, Figure 7 is an intermediate-time snapshot and cannot by itself support the claimed persistence during $3000 - 5000$ ms. The same caution applies to visually spiral-like contours in Figure 5: their topology and persistence must be verified by Equations (A15)–(A17).

### *Appendix A.6. Local Coherence and Spatial Coexistence*

For a square neighbourhood $\mathcal{N}_{(ij)}$ of radius $r = 3$ (a $7 \times 7$ window away from boundaries), define the local complex order parameter

$$Z_{(i,j)}(t) = \frac{1}{|\mathcal{N}_{(i,j)}|} \sum_{(k,l) \in \mathcal{N}_{(i,j)}} e^{\mathrm{i}\phi_{kl}(t)}, \qquad R_{(i,j)}(t) = |Z_{(i,j)}(t)|. \tag{A18}$$

Nodes are assigned to three classes:

$$\begin{aligned} R_{ij}(t) \geq R_{\mathrm{coh}} = 0.80 \quad &\Rightarrow \text{ coherent,} \\ R_{ij}(t) \leq R_{\mathrm{inc}} = 0.40 \quad &\Rightarrow \text{ incoherent,} \\ 0.40 < R_{ij}(t) < 0.80 \quad &\Rightarrow \text{ intermediate/ chimera.} \end{aligned} \tag{A19}$$

Tiny isolated clusters are removed before the area fractions are measured. A recommended minimum connected-component area is $\max(4, 0.001 N_x N_y)$ nodes. Let $f_{\mathrm{coh}}(t)$ and $f_{\mathrm{inc}}(t)$ be the fractions occupied by the retained coherent and incoherent components. The instantaneous coexistence indicator is

$$C(t) = \mathbf{1}[f_{\mathrm{coh}}(t) \geq 0.05]\mathbf{1}[f_{\mathrm{inc}}(t) \geq 0.05]. \tag{A20}$$

This connected-domain requirement prevents sparse noisy pixels or a narrow wavefront from being misidentified as an incoherent population.

*Appendix A.7. Temporal Persistence Decision*

For the intermediate interval used in the manuscript, $I_{\mathrm{ch}} = [1000 - 2000]$ ms, define

$$P_{\mathrm{ch}} = \frac{1}{N_{\mathrm{ch}}} \sum_{t_n \in I_{\mathrm{ch}}} C(t_n). \tag{A21}$$

The pattern is classified as a transient chimera-like state when $P_{\mathrm{ch}} \geq 0.80$, the coherent and incoherent components remain spatially distinguishable, and the low-$R$ domain cannot be explained solely by the moving interface of an otherwise coherent traveling wave. The latter condition can be checked by plotting coherent- and incoherent-residence maps over $I_{\mathrm{ch}}$ and, where possible, by confirming larger local frequency dispersion in the low-$R$ region.

Because the manuscript proposes that the intermediate pattern subsequently evolves into a spiral, the appropriate label is transient chimera-like coexistence, not an asymptotically stable chimera. For each of the five initializations, report $P_{\mathrm{ch}}$, the time-averaged values of $f_{\mathrm{coh}}$ and $f_{\mathrm{inc}}$, their variability, and the largest connected-domain fractions. A robust claim should again be supported by at least four of five runs satisfying the complete operational criterion.

*Appendix A.8. Direct Relationship to the Spatial Figures*

Figure 5c,d,i,j, at $t = 1000$ and 2000 ms, shows labyrinthine or mixed spatial structures that are reasonable candidates for chimera-like coexistence. Their classification requires the fractions in Equation (A20) at every stored time, not a visual estimate of the relative colour areas. The chimera-region and local-order maps in Figure 5c,e are relevant to this intermediate interval, but one map at $t = 2000$ ms cannot demonstrate $P_{\mathrm{ch}} \geq 0.80$. Conversely, Figure 6c,e at $t = 100$ ms belongs to the early transient and should be used as an early-time reference, not as evidence for the intermediate chimera state.

The revised figure should add the time series $f_{\mathrm{coh}}(t)$, $f_{\mathrm{inc}}(t)$, and $\langle R_{ij}(t) \rangle_{ij}$, shade the interval $[1000 - 2000]$ ms, and show the coherent- and incoherent-residence maps. If either retained fraction falls below 5% for more than 20% of this interval, the operational chimera criterion is not satisfied, even when an individual snapshot appears spatially heterogeneous.

Appendix A.8.1. Global Kuramoto Order Parameter and Global Error

In order to characterize synchronization state of network, we introduce synchronization factor (*SF*). By using Mean-Field Theory (*MFT*), synchronization factor denoted $R(t)$ across a two-dimensional grid network $N \times N$ where each node of network with membrane potential $x_{(i,j)}$ represents an oscillator with a phase $\theta_{(i,j)}$, can be estimated based on Equation (A22) [182–185].

$$R(t)e^{i\phi} = \frac{1}{N^2} \sum_{i=1}^{N} \sum_{j=1}^{N} e^{i\theta_{i,j}(t)}, \tag{A22}$$

where $\phi$ is the average phase of network, $e^{i\theta_{(i,j)}}$ represents each oscillator's position on the unit circle in complex plane. The magnitude of *SF* is found by using Equation (A23). It is also possible to find *SF* in two-dimensional arrays using statistical approach as described in references [186–189].

$$R(t) = \Big|\frac{1}{N^2}\sum_{i=1}^{N}\sum_{j=1}^{N} e^{i\theta_{(i,j)}(t)}\Big|. \tag{A23}$$

Parameter $R(t)$ measures how in phase elements are across the array. For $R \approx 1$, we observe global synchronization where all nodes are in phase, while for $R \approx 0$ global desynchronization where all nodes are randomly distributed. The evaluation of synchronization error (*SE*) denoted $E(t)$ is computed using *SF* as given in Equation (A24).

$$E(t) = 1 - \big(R(t)\big)^2. \tag{A24}$$

For $E(t)$ close (resp. equal) to 0, nodes are highly (resp. perfectly) synchronized and when $E(t)$ is close to 1, nodes are desynchronized.

For the inter-network, we evaluate the Kuramoto synchronization between two networks using Equation (A25).

$$R_{ij}(t) = \Big|\frac{1}{N^2}\sum_{i=1}^{N}\sum_{j=1}^{N} e^{i(\theta_i(t)-\theta_j(t))}\Big|, \tag{A25}$$

where $\theta_i(t)$ and $\theta_j(t)$ are the phase angle of both networks.

Appendix A.8.2. Gradient

To characterize wave patterns in the array (network), calculating evolution of gradient can help detect local spatial variations. The gradient captures local variations, which are key indicators of wave behavior in the array. If gradient is non-zero, this indicates structured wave-like propagation rather than synchronization or randomness. Additionally if waves is progressive and structured with respect the time, gradient will increase gradually or decrease, and in otherwise when patterns are not organized, waves are in disorder and gradient just fluctuating with a constant variation with respect the time. To find gradient of membrane potential $x_{(i,j)}$, we could define spatial derivatives in two dimension by $\frac{\partial x_{(i,j)}}{\partial x_i}$ and $\frac{\partial x_{i,j}}{\partial x_j}$. The expression of magnitude denoted $G(t)$ is given in Equation (A26). We define a parameter $G_m$ indicating an interval where amplitude of $G(t)$ is constant in time. In this case, no disorder waves occur, otherwise we observe waves propagation.

$$G(t) = \mid \nabla x_{(i,j)} \mid = \Big((\frac{\partial x_{(i,j)}}{\partial x_i})^2 + (\frac{\partial x_{(i,j)}}{\partial x_j})^2\Big)^{\frac{1}{2}}. \tag{A26}$$

Appendix A.8.3. Population Mean-Field Signal

To obtain a macroscopic summary of the simulated network activity over time a *t*, we define an *EEG*-like population signal as the spatial average of the neuronal membrane potentials for a network ($N \times N$) of $N^2$ neurons by using Equation (A27) [57, 190].

$$EEG = \frac{1}{N^2}\sum_{i=1}^{N}\sum_{j=1}^{N} V_{i,j}(t), \tag{A27}$$

where $V_{i,j}(t)$ is membrane potential of neuron at position *(i,j)* at time *t*. This quantity measures the collective activity of the computational network. It is not a biophysical reconstruction of scalp *EEG* because the model does not include neuronal dipole orientation, extracellular conductivity, head geometry, volume conduction, or electrode placement. *EEG frequency response* is estimated using Equation (A28).

$$P(f) = \Big|FFT(EEG)\Big|^2, \tag{A28}$$

where $FFT(.)$ is Fast Fourier Transform of *EEG signal* and $P(f)$ is power spectrum at frequency *f*. The peak in $P(f)$ shows dominant oscillation frequency (Hz).

Appendix A.8.4. PLV

To characterize degree of similarity between different networks grid, we have quantify phase consistency across networks at specific *EEG* frequencies by using Phase Locking Value (*PLV*) [191–193]. If *PLV* is close to 1, waves propagate with fixed phase differences, then synchronized otherwise *PLV* is close to O involving no phase relationship, then desynchronization of networks. Equation (A29) defines expression to compute *PLV* between two signals $x_1(t)$ and $x_2(t)$.

$$PLV = \left| \frac{1}{N} \sum_{t=1}^{N} e^{i\left(\phi_{x_1}(t) - \phi_{x_2}(t)\right)} \right|. \tag{A29}$$

For *M* signals, we define *PLV* matrix as $M \times M$ symmetric matrix where each entry *PLV* quantifies phase locking between signals $x_1(t)$ and $x_2(t)$.

Appendix A.8.5. Transfer Entropy (TE)

Transfer entropy (*TE*) is a non-parametric measure that captures directed, nonlinear information transfer. It is computed per pair of groups and summed across links to estimate network-level transfer. *TE* from process *X* to process *Y* is given by Equation (A30).

$$TE_{(X \to Y)} = \sum p\left(y_{t+1}, y_t^k, x_t^l\right) \log \frac{p\left(y_{t+1} \middle| y_t^k, x_t^l\right)}{p\left(y_{t+1} \middle| y_t^k\right)}, \tag{A30}$$

$TE_{X \to Y}$ quantifies the reduction in uncertainty about the future of $Y$ provided by the past of $X$, beyond the information already contained in the past of $Y$

Appendix A.8.6. Directional Index

Let $TE_{X \to Y}$ denote the transfer entropy from Network $X$ to Network $Y$. The normalized directional index between two networks is defined as

$$NDI_{X,Y} = \frac{TE_{X \to Y} - TE_{Y \to X}}{TE_{X \to Y} + TE_{Y \to X} + \varepsilon}, \tag{A31}$$

where $\varepsilon$ is a small positive constant that prevents division by zero. The index is bounded by

$$-1 \leq NDI_{X,Y} \leq 1 \tag{A32}$$

and satisfies

$$NDI_{Y,X} = -NDI_{X,Y}. \tag{A33}$$

Its interpretation is as follows:

- $NDI_{X,Y} > 0$: the dominant predictive information flow is $X \to Y$;
- $NDI_{X,Y} < 0$: the dominant predictive information flow is $Y \to X$;
- $NDI_{X,Y} \simeq 0$: the two directions are approximately balanced, or both transfer-entropy values are too small to establish a direction.

For a proposed three-network architecture hierarchy,

$$\text{Network 3} \to \text{Network 2} \to \text{Network 1} \tag{A34}$$

requires

$$NDI_{3,2} > 0 \qquad \text{and} \qquad NDI_{2,1} > 0. \tag{A35}$$

The overall hierarchy score is therefore defined as

$$H = \min(NDI_{3,2}, NDI_{2,1}). \tag{A36}$$

A positive value of $H$ indicates that both links have the direction required by the proposed hierarchy. A negative value indicates that at least one link is reversed, whereas a value close to zero indicates weak or balanced directionality.

Validation Criteria

The sign of $NDI_{X,Y}$ alone is not sufficient to establish directed information flow. The following criteria should be satisfied.

(a) Transfer-Entropy Significance

Each observed transfer entropy must exceed a surrogate null distribution. An empirical probability can be calculated as

$$p_{X\to Y} = \frac{1 + \sum_{s=1}^{N_s} \mathbf{1}\Big[TE_{X\to Y}^{(s)} \geq TE_{X\to Y}^{\text{obs}}\Big]}{N_s + 1}, \tag{A37}$$

where $N_s$ is the number of surrogate realizations. A directed link is considered significant when $p_{X\to Y} < 0.05$, after correction for multiple comparisons when required. The finite-sample bias may also be removed using effective transfer entropy,

$$ETE_{X\to Y} = TE_{X\to Y}^{\text{obs}} - \Big\langle TE_{X\to Y}^{(s)} \Big\rangle_s, \tag{A38}$$

in which case the values of $ETE$ replace the raw $TE$ values in Equation (A31).

(b) Confidence Interval of the Directional Index

The directional index must be evaluated over independent initial conditions or bootstrap realizations. Direction $X \to Y$ is statistically supported only when the 95% confidence interval of $NDI_{X,Y}$ lies entirely above zero. Similarly, direction $Y \to X$ is supported only when the complete confidence interval lies below zero. An interval containing zero indicates that the dominant direction has not been reliably established. For the full hierarchy, the 95% confidence intervals of both $NDI_{3,2}$ and $NDI_{2,1}$ must exclude zero on the positive side. Equivalently, the confidence interval of the hierarchy score $H$ should lie above zero.

(c) Reproducibility across Realizations

For $N_r$ independent simulations, define the hierarchy-consistency rate as

$$R_H = \frac{1}{N_r} \sum_{r=1}^{N_r} \mathbf{1}\Big[NDI_{3,2}^{(r)} > 0 \ \wedge \ NDI_{2,1}^{(r)} > 0\Big]. \tag{A39}$$

As an operational criterion, the hierarchy may be considered robust within a tested parameter domain when $R_H \geq 0.80$, provided that both directed links are statistically significant. The 80% criterion is a predefined reproducibility rule rather than a universal constant and must therefore be reported explicitly.

(d) Robustness to Model Parameters

The validation must be repeated while varying stimulus frequency, stimulus amplitude, relative stimulus phase, and inter-network coupling strength. The specific hierarchy is robust only over the parameter region in which $NDI_{3,2} > 0$, $NDI_{2,1} > 0$, and $R_H \geq 0.80$. Results obtained from a single parameter set should be described as condition-specific rather than universal. Because Networks 1 and 3 are structurally equivalent under identical stimuli and symmetric coupling, a label-swap control should also be performed. The stimuli and initial conditions of Networks 1 and 3 are exchanged, after which the complete transfer-entropy analysis is repeated. A direction that follows the stronger or phase-leading input indicates stimulus-dependent selection. A direction that remains attached to the same numerical network label after the swap may indicate an unintended model or implementation asymmetry.

(e) Conditional Information Transfer

Pairwise transfer entropy can contain contributions from a common external drive or an indirect pathway. Therefore, the hierarchy should preferably be confirmed using transfer entropy conditioned on the third network and on the external stimuli. In particular, a mediated $3 \to 2 \to 1$ pathway is supported when

$$CTE_{3\to 2|S} > CTE_{2\to 3|S}, \tag{A40}$$

$$CTE_{2\to 1|3,S} > CTE_{1\to 2|3,S}, \tag{A41}$$

and the apparent direct transfer from Network 3 to Network 1 decreases after conditioning on Network 2:

$$CTE_{3\to 1|2,S} < TE_{3\to 1|S}. \tag{A42}$$

Here, $S$ represents the external stimulation signals.

Final Decision Rule

The hierarchy Network 3 $\rightarrow$ Network 2 $\rightarrow$ Network 1 is considered validated only if all of the following conditions are satisfied:

(1) $NDI_{3,2} > 0$ and $NDI_{2,1} > 0$;
(2) the corresponding transfer entropies are significant relative to surrogate distributions ($p < 0.05$);
(3) the 95% confidence intervals of both directional indices exclude zero on the positive side;
(4) the hierarchy-consistency rate satisfies $R_H \geq 0.80$;
(5) the direction remains reproducible over a clearly reported range of stimulus and coupling parameters;
(6) conditional transfer entropy supports mediation through Network 2 rather than a common-stimulus artifact.

If only the first condition is satisfied, the result should be reported as a descriptive directional tendency for that particular simulation, not as a robust information-flow hierarchy.

Appendix A.8.7. $D_8$ Symmetry Index (Octagonal Detection)

An ideal octagonal pattern is associated with the dihedral symmetry group $D_8$, defined here as the symmetry group of a regular octagon. It contains eight rotations,

$$R_k : \theta \mapsto \theta_0 + \frac{k\pi}{4}, \qquad k = 0, \ldots, 7,$$

and eight reflections. Consequently, $D_8 = \{R_0, \ldots, R_7, S_0, \ldots, S_7\}, \qquad |D_8| = 16$. Thus, $D_8$ denotes the octagonal dihedral group of order 16, rather than a group of order 8.A value of 1 means perfect $D_8$ symmetry and strong organization according to eight directions; larger values close to 0 indicate deviation or no symmetry and disordered angular distribution.

Let us consider a set of points $P = \{p_1, p_2, ..., p_N\}$ in *2D* associated with boundary or shape pixels of an image as the *input* to a network. The parameter $D_8 \in [0, 1]$ is the *output*, whose interpretation is given in Table A2.

The eight-fold symmetry observed in our network arises from a fundamental geometric property of the square lattice used to construct the neuronal array (Figure 4). In a square lattice, wave propagation is inherently anisotropic because the coupling topology provides preferential transmission along cardinal axis ($\theta = 0°, 90°, 180°, 270°$) and diagonal axis ($\theta = 45°, 135°, 225°, 315°$), each with 4 directions.

In the context of our studies, the *input* data is (1) the *2D* field of the membrane potential in the network of 200 in spatial domain after after compute *FFT*, and (2) two dominant frequency components with ratio $\Omega_2/\Omega_1 \approx 8$. The *output* is associated to $D_8$ index, an angular spectrum $A(\theta)$,a phase velocity lobe orientations, and an octagon detection.

The $D_8$ condition emerges formally from the discretized wave equation on the square lattice [194]. The lattice Laplacian acting on a plane wave $e^{i(k_x x + k_y y)}$ with lattice spacing $a$ at position $r = (x, y)$ is given by Equation (A43).

$$\nabla^2_{\text{lattice}}\, e^{i\mathbf{k}\cdot\mathbf{r}} = -\frac{4}{a^2}\left[\sin^2\left(\frac{k_x a}{2}\right) + \sin^2\left(\frac{k_y a}{2}\right)\right] e^{i\mathbf{k}\cdot\mathbf{r}} \tag{A43}$$

Expanding and grouping to fourth order in $k$:

$$\nabla^2_{\text{lattice}} \approx -|k|^2 + \frac{a^2}{12}\left(k_x^4 + k_y^4\right) + O(k^6), \tag{A44}$$

with the anisotropic term $k_x^4 + k_y^4$ of eight-fold angular symmetry given by Equation (A45).

$$(k_x^4 + k_y^4) = |k|^4\left(\frac{3}{4} + \frac{1}{4}\cos(4\theta)\right). \tag{A45}$$

This $\cos(4\theta)$ anisotropy, when combined with the sinusoidal driving, generates second-harmonic spatial modes at $8\theta$ through the nonlinear mixing term in the *EMR* coupling. The resonance condition $\Omega_2/\Omega_1 \approx 8$ ensures that these $8\theta$ modes are phase-locked across the entire network, producing the observed octagonal symmetry.

Appendix A.8.8. Origin of the $8\theta$ Mode: A Rigorous Derivation

A $\cos 4\theta$ term carries $D_4$ symmetry and cannot, by itself Ddirectly produce $D_8$. The correct chain of reasoning is established here.

Step 1: The Linear Lattice Is $D_4$, not $D_8$

From Equation (A43), the linear dispersion relation of the square lattice is

$$\omega_{\text{latt}}^2(\mathbf{k}) = \frac{4c^2}{a^2}\left[\sin^2\left(\frac{k_x a}{2}\right) + \sin^2\left(\frac{k_y a}{2}\right)\right] \simeq c^2|\mathbf{k}|^2 - \frac{c^2 a^2}{12}|\mathbf{k}|^4\left(\frac{3}{4} + \frac{1}{4}\cos 4\theta\right). \tag{A46}$$

The only angular dependence is $\cos 4\theta$; hence the linear lattice respects $D_4$ symmetry only. No $8\theta$ component exists at linear order.

Step 2: The Quadratic Nonlinearity Squares the Anisotropy

Let the EMR coupling contain a quadratic term $\mathcal{N}[\phi] = \beta\phi^2$. Decomposing the field as

$$\phi(\mathbf{r}, t) = \sum_{\mathbf{k}} A_{\mathbf{k}}(t)\, e^{i\mathbf{k}\cdot\mathbf{r}} + \text{c.c.}, \tag{A47}$$

the nonlinear source for mode $\mathbf{k}$ is

$$S_{\mathbf{k}}(t) = \beta \sum_{\mathbf{k}_1+\mathbf{k}_2=\mathbf{k}} A_{\mathbf{k}_1} A_{\mathbf{k}_2}. \tag{A48}$$

The angular dependence of the quadratic source amplitude is the *square* of the linear anisotropy:

$$\left[\cos 4\theta\right]^2 = \frac{1}{2}\left(1 + \cos 8\theta\right). \tag{A49}$$

Equation (A49) is the only clean mechanism producing a genuine $8\theta$ term. It must be displayed explicitly.

Step 3: Projection onto the $8\theta$ Mode (the Proof)

Define the angular projection onto the eighth harmonic,

$$P_8 = \frac{1}{2\pi}\int_0^{2\pi} S_{\mathbf{k}}(\theta)\, e^{-i8\theta}\, d\theta. \tag{A50}$$

Substituting Equation (A49),

$$P_8 = \frac{\beta}{2\pi}\int_0^{2\pi} \frac{1}{2}\left(1 + \cos 8\theta\right) e^{-i8\theta}\, d\theta = \frac{\beta}{4} \neq 0. \tag{A51}$$

**Proposition 1** (Excitation of the $8\theta$ mode)**.** *For $\beta \neq 0$, the quadratic nonlinearity excites the eighth angular harmonic with non-zero projection $P_8 = \beta/4$.*

**Proof.** Direct evaluation of the integral in Equation (A51) using $\cos 8\theta = \frac{1}{2}(e^{i8\theta} + e^{-i8\theta})$ yields $P_8 = \beta/4$. □

Step 4: Conditions for Phase-Locking

Excitation (Proposition 1) is necessary but not sufficient for a *phase-locked* $D_8$ pattern. Three conditions must hold:

(C1) Quadratic nonlinearity present: $\beta \neq 0$ in the EMR coupling, to be shown from the model equations (not assumed).

(C2) Frequency matching: $\Omega_2 \approx 8\Omega_1$ (or a chain of couplings reaching it), to be derived from Equation (A46), not posited.

(C3) Phase stationarity: $\Delta\Phi(\theta) = \Phi_2 - 8\Phi_1$ is approximately constant in $\theta$; this is precisely what $D_8$ measures.

*"The square-lattice Laplacian produces an anisotropy of orderfour in the azimuthal angle, $\propto \cos 4\theta$, which carries only $D_4$ symmetry. A mode with $D_8$ symmetry cannot arise at linear order. It arises at second order: the quadratic EMR nonlinearity $\mathcal{N} = \beta\phi^2$ generates a source whose angular dependence is $\cos^2 4\theta = \frac{1}{2}(1 + \cos 8\theta)$. Projecting this source onto the eighth angular harmonic yields*

*$P_8 = \beta/4 \neq 0$, proving that the $8\theta$ mode is genuinely excited. Phase-locking of this mode requires (i) $\beta \neq 0$, (ii) $\Omega_2 \approx 8\Omega_1$, and (iii) a stationary relative phase $\Delta\Phi(\theta)$; the index $D_8$ quantifies precisely the degree of this locking."*

## Appendix B. Calibration and Validation Protocol

### *Appendix B.1. Synthetic Ground-Truth Test Set*

Fields with analytically known $D_8$ are constructed by specifying $e^{i\Delta\Phi(\theta)}$ directly (Table A1).

**Table A1.** Synthetic test cases with known symmetry.

| Test Case | Construction | Expected $D_8$ |
|---|---|---|
| Perfect octagon | $e^{i8\theta}$ | 1 |
| Square ($D_4$) | $e^{i4\theta}$ | 0 |
| Hexagon ($D_6$) | $e^{i6\theta}$ | 0 |
| Isotropic / circle | $\Delta\Phi = \text{const}$ | 0 |
| White noise | $\Delta\Phi \sim \mathcal{U}(0, 2\pi)$ | $\approx 0$ (fluctuating) |
| Noisy octagon | $8\theta + \eta(\theta)$, $\eta \sim \mathcal{N}(0, \sigma^2)$ | $e^{-\sigma^2/2}$ (analytic) |
| Shifted octagon | $8\theta + \varphi_0$ | invariant |

Two Important Checks:

(1) Phase-shift invariance. For $e^{i(8\theta+\varphi_0)}$, $C_8 = e^{i\varphi_0}$, so $|C_8|$ is unchanged: $D_8$ is invariant under global rotation. This is desirable, but it means $D_8$ cannot detect a rotation offset; use $\arg C_8$ for that.
(2) Nyquist angular condition. To resolve the eighth harmonic, $N_\theta > 16$; recommend $N_\theta \geq 64$.

### *Appendix B.2. Analytic Noise Prediction*

For uncorrelated angular noise $\eta(\theta)$,

$$C_8(\sigma) = \frac{1}{2\pi}\int_0^{2\pi} e^{i(8\theta+\eta(\theta))}e^{-i8\theta}\,d\theta = \mathbb{E}[e^{i\eta}] = e^{-\sigma^2/2}. \tag{A52}$$

Hence $D_8(\sigma)$ decays as $e^{-\sigma^2/2}$ (up to normalization by the other harmonics). Plot the measured $D_8$ versus $\sigma$ and overlay the analytic curve of Equation (A52); this validates the estimator quantitatively.

### *Appendix B.3. Statistical Validation on Real Data*

(1) Permutation test: shuffle $\Delta\Phi(\theta)$ over $\theta$, recompute $D_8$, repeat $10^3$ times; obtain the null distribution and a $p$-value for the observed $D_8$.
(2) Rotation test: rotate the field by $45°$; $D_8$ must be invariant (property of $D_8$). A failure reveals angular-sampling artifacts.
(3) Sub-sampling test: vary $N_\theta$; report the stability of $D_8$.

### *Appendix B.4. Deliverables*

- Table: $D_8$ (mean $\pm$ std over $10^3$ realizations) for each synthetic case.
- Figure: $D_8(\sigma)$ with analytic $e^{-\sigma^2/2}$ overlay.
- Figure: ROC curve with the selected threshold.
- $p$-value of the permutation test on real data.

## Appendix C. Justification of the $D_8$ Normalization

The current definition

$$D_8 = \frac{|C_8|}{\sum_{k=1}^{8}|C_k|} \tag{A53}$$

truncates the sum at $k = 8$ without justification. Add the following.

- Rationale for truncation. The sum is limited to the symmetry order of interest ($k \leq 8$); higher harmonics are treated as deviations.

- Alternative normalizations considered. $D_8 = |C_8| / \sum_{n\geq 1} |C_n|$ (full spectrum) and $D_8 = |C_8|/|C_0|$.
- Sensitivity. On the synthetic cases (Table A1), report $\sum_{k>8} |C_k|$; if this residual is non-negligible on real data, extend the sum. Show that the chosen normalization is stable and that higher harmonics do not spuriously inflate or deflate $D_8$.

The $D_8$ method can then be generalized for specific applications.

*Appendix C.1. Calibration of the $D_8$ Classification Thresholds for the Square-Lattice Neuronal-Network Model*

Here, we describe a reproducible procedure for obtaining and applying the thresholds $0.2$, $0.5$, and $0.7$ used to classify the eighth-order angular index $D_8$. The procedure separates statistical significance from pattern strength, corrects for the background anisotropy of the square lattice, and requires comparison with the competing fourth-order component $D_4$. Under this calibration, the three numerical limits represent approximately 20%, 50%, and 70% of the measurable range between a lattice-dependent null state and an ideal noisy octagonal reference. Two different decisions must be distinguished: whether the measured eighth-order component exceeds the fluctuations expected from noise and the square lattice; how strong the statistically significant component is relative to an ideal octagonal reference. The first decision is made using a null-distribution threshold. The second is made using the calibrated limits $0.2$, $0.5$, and $0.7$.

Appendix C.1.1. Step 1: Compute the Angular Coefficients

Let $p(\theta_b, t)$ denote the normalized angular distribution obtained from the spatial activity at time $t$, where $\theta_b$ is the centre of angular bin $b$. The normalization condition is

$$\sum_{b=1}^{N_\theta} p(\theta_b, t) = 1. \tag{A54}$$

For angular order $m$, define

$$C_m(t) = \sum_{b=1}^{N_\theta} p(\theta_b, t) \exp(-\mathrm{i}m\theta_b), \tag{A55}$$

and

$$D_m^{\mathrm{raw}}(t) = |C_m(t)|. \tag{A56}$$

The analysis should calculate at least $D_2, D_4, D_6, D_8$, because a large $D_8$ alone does not uniquely identify an octagonal pattern. However $D_8$ is use for our analysis. In particular, a four-directional square pattern can also have a large eighth angular harmonic.

The same estimator, angular bins, spatial window, Fourier convention, and wavenumber interval must be used for the observed data, null controls, and synthetic reference patterns.

Appendix C.1.2. Step 2: Generate the Null Distribution

The null ensemble must reproduce the numerical effects that can generate a non-zero $D_8$ without genuine octagonal organization. These effects include finite lattice size, square-grid anisotropy, boundary effects, discretization, and noise. The recommended control is a set of $N_s \geq 500$ simulations, preferably $N_s = 1000$, performed with the same square lattice and numerical parameters as the main simulations, but without the mechanism expected to generate the octagonal state. Examples include simulations without external stimulation or with randomized stimulation phases. Angularly randomized surrogate fields may also be used. The radial spectrum, total energy, and the symmetry between $\theta$ and $\theta + \pi$ should be preserved while the organization of the angular sectors is randomized. If the index is calculated from a relative phase $\Delta\Phi(\theta)$, the relative phases should be permuted among angular sectors. Randomizing Fourier phases alone is not sufficient when $D_8$ is calculated from angular power, because such randomization may leave the angular power distribution unchanged.

For every null realization $s$, calculate $D_{8,s}^{\mathrm{null}}$ and $D_{4,s}^{\mathrm{null}}$. Define the background level $B_8 = \mathrm{median}\{D_{8,s}^{\mathrm{null}}\}_{s=1}^{N_s}$ and the statistical threshold $T_{\mathrm{sig}} = Q_{0.95}(D_8^{\mathrm{null}})$, where $Q_{0.95}$ denotes the 95th percentile.

For an observed value $D_8^{\mathrm{obs}}$, the empirical probability is

$$p_8 = \frac{1 + \sum_{s=1}^{N_s} \mathbf{1}\left(D_{8,s}^{\mathrm{null}} \geq D_8^{\mathrm{obs}}\right)}{N_s + 1}. \tag{A57}$$

The eighth-order component is considered statistically significant only if $D_8^{\mathrm{obs}} > T_{\mathrm{sig}} \quad \text{and} \quad p_8 < 0.05.$

Appendix C.1.3. Step 3: Generate an Ideal Octagonal Reference

An ideal eight-directional reference is constructed using the orientations $\theta_j = \theta_0 + j\frac{\pi}{4}$, $j = 0, \ldots, 7$, which are separated by $45°$.

One possible spatial reference field is

$$V_8(x, y) = \sum_{j=0}^{3} \cos[k_0(x \cos\theta_j + y \sin\theta_j) + \phi_j]. \tag{A58}$$

Each plane wave produces two opposite Fourier peaks, so four independent orientations generate eight directional peaks. The reference patterns must be sampled on the same grid as the neuronal network. They should be generated for several values of the global orientation $\theta_0 \in [0, \pi/4)$, random phases $\phi_j$, and noise levels matching the main simulations. The complete analysis pipeline must then be applied without modification.

If $D_{8,r}^{\mathrm{ideal}}$ denotes the result for ideal-reference realization $r$, define $I_8 = \mathrm{median}\{D_{8,r}^{\mathrm{ideal}}\}$.

At least 100 rotated and noise-contaminated ideal patterns should be used so that $I_8$ is not determined by a single orientation relative to the square grid.

Appendix C.1.4. Step 4: Calibrate the Measured Index

The raw index is transformed into a calibrated index according to

$$D_8^{\mathrm{cal}} = \mathrm{clip}\left[\frac{D_8^{\mathrm{raw}} - B_8}{I_8 - B_8}, 0, 1\right], \tag{A59}$$

where $\mathrm{clip}(z, 0, 1)$ restricts $z$ to the interval $[0, 1]$. Under this definition, $D_8^{\mathrm{cal}} = 0$ corresponds to the median lattice-dependent background, whereas $D_8^{\mathrm{cal}} = 1$ corresponds to the measured ideal octagonal reference under the same numerical conditions. The calibration is valid only when $I_8 > B_8$. If this condition is not met, the analysis pipeline cannot reliably distinguish an ideal octagonal pattern from its background and the thresholds must not be applied.

Appendix C.1.5. Step 5: Derive the Limits 0.2, 0.5, and 0.7

Consider the controlled mixture $p_\lambda(\theta) = (1 - \lambda)p_{\mathrm{null}}(\theta) + \lambda p_8(\theta)$, $0 \le \lambda \le 1$, where $p_{\mathrm{null}}$ is the null angular distribution and $p_8$ is the ideal octagonal distribution. The parameter $\lambda$ is the imposed fraction of octagonal organization. After the background-to-ideal calibration in Equation (A59), one expects $D_8^{\mathrm{cal}} \simeq \lambda$.

Consequently,

$$\begin{aligned} \lambda = 0.2 \quad &\Longrightarrow \quad D_8^{\mathrm{cal}} \simeq 0.2, \\ \lambda = 0.5 \quad &\Longrightarrow \quad D_8^{\mathrm{cal}} \simeq 0.5, \\ \lambda = 0.7 \quad &\Longrightarrow \quad D_8^{\mathrm{cal}} \simeq 0.7. \end{aligned} \tag{A60}$$

Thus, the three limits represent approximately 20%, 50%, and 70% of the observable transition from the lattice-dependent null state to the ideal octagonal reference. The relationship should be verified numerically by generating mixed patterns for several values of $\lambda$, for example $\lambda = 0, 0.05, 0.10, \ldots, 1$.

Appendix C.1.6. Step 6: Convert the Limits to Raw-Index Thresholds

The manuscript reports $D_8^{\mathrm{raw}}$. We can convert into the calibrated quantity, and the equivalent thresholds are $T_{0.2} = B_8 + 0.2(I_8 - B_8)$, $T_{0.5} = B_8 + 0.5(I_8 - B_8)$, $T_{0.7} = B_8 + 0.7(I_8 - B_8)$.

The effective lower boundary is $T_{\mathrm{lower}} = \max(T_{\mathrm{sig}}, T_{0.2})$, because a component that does not exceed the null distribution should not be classified as octagonal even if its calibrated value is close to 0.2.

For example, if $B_8 = 0.10$ and $I_8 = 0.90$, then

$$T_{0.2} = 0.26, \qquad T_{0.5} = 0.50, \qquad T_{0.7} = 0.66.$$

This numerical example is illustrative and must not be reported as a result of the neuronal-network simulations.

### Appendix C.1.7. Step 7: Control for Square-Lattice Anisotropy

A square or four-directional pattern can simultaneously produce large values of $D_4$ and $D_8$. Therefore, a large $D_8$ is not by itself sufficient to establish octagonal organization. Define $\Delta_{8,4} = D_8 - D_4$. For each null realization, calculate $\Delta^{\mathrm{null}}_{8,4,s} = D^{\mathrm{null}}_{8,s} - D^{\mathrm{null}}_{4,s}$ and define $T_\Delta = Q_{0.95}\big(\Delta^{\mathrm{null}}_{8,4}\big)$.

A specific octagonal classification requires $D^{\mathrm{raw}}_8 > T_{\mathrm{sig}}$ and $D^{\mathrm{raw}}_8 - D^{\mathrm{raw}}_4 > T_\Delta$.

If $D_8$ is significant but the second condition is not satisfied, the result should be described as a non-specific eighth-order harmonic potentially related to square-lattice anisotropy, rather than as established octagonal symmetry.

### Appendix C.1.8. Step 8: Verify the Eight Angular Maxima

For strong classifications, the angular distribution should contain eight resolved maxima. After sorting their angles, calculate the circular separations

$$\Delta\theta_j = \mathrm{mod}(\theta_{j+1} - \theta_j, 2\pi). \tag{A61}$$

For an ideal octagonal arrangement, $\overline{\Delta\theta} \simeq \frac{\pi}{4} = 45^\circ$. The angular-spacing error may be quantified as

$$E_\theta = \sqrt{\frac{1}{8}\sum_{j=1}^{8}\Big(\Delta\theta_j - \frac{\pi}{4}\Big)^2}. \tag{A62}$$

The accepted tolerance for $E_\theta$ should be obtained from the $95^{th}$ percentile of the noisy ideal-reference patterns rather than selected arbitrarily.

## *Appendix C.2. Final Classification Rule*

Table A2 gives the recommended interpretation of the calibrated index.

**Table A2.** Unified classification of the calibrated eighth-order angular index $D^{\mathrm{cal}}_8$. The index quantifies the strength of the eighth-order component, whereas confirmation of octagonal organization requires statistical significance, dominance over the fourth-order component, and eight approximately equidistant angular maxima.

| $\boldsymbol{D^{\mathrm{cal}}_8}$ | **Additional Requirements** | **Classification and Reporting Rule** |
|---|---|---|
| $D^{\mathrm{cal}}_8 < 0.2$ | None | Negligible eighth-order component. No octagonal organization is inferred. |
| $0.2 \le D^{\mathrm{cal}}_8 < 0.5$ | $D^{\mathrm{raw}}_8 > T_{\mathrm{sig}}$ and $p_8 < 0.05$ | Weak but statistically significant eighth-order organization. If the significance conditions are not satisfied, the measured component is classified as background fluctuation. |
| $0.5 \le D^{\mathrm{cal}}_8 < 0.7$ | $D^{\mathrm{raw}}_8 > T_{\mathrm{sig}}$, $p_8 < 0.05$, and $\Delta_{8,4} > T_\Delta$. | Pronounced eighth-order organization and candidate octagonal pattern. If $\Delta_{8,4} \le T_\Delta$, the result is reported only as a non-specific eighth-order harmonic potentially associated with square-lattice anisotropy. |
| $D^{\mathrm{cal}}_8 \ge 0.7$ | $D^{\mathrm{raw}}_8 > T_{\mathrm{sig}}$, $p_8 < 0.05$, $\Delta_{8,4} > T_\Delta$, and eight resolved angular maxima with successive separations $\Delta\theta_j \simeq \pi/4$. | Strong and robust octagonal organization. If all the supplementary conditions are not satisfied, the result is reported only as a strong eighth-order angular component, not as confirmed octagonal symmetry. |

Here,

$$\Delta_{8,4} = D^{\mathrm{raw}}_8 - D^{\mathrm{raw}}_4,$$

$T_{\mathrm{sig}}$ is the significance threshold obtained from the null distribution, and $T_\Delta$ is the corresponding threshold for the harmonic contrast $\Delta_{8,4}$. For the eight detected maxima, the circular peak separations are

$$\Delta\theta_j = \mathrm{mod}(\theta_{j+1} - \theta_j, 2\pi), \qquad \Delta\theta_j \simeq \frac{\pi}{4} = 45^\circ.$$

The numerical intervals 0.2, 0.5, and 0.7 apply to the calibrated index $D^{\mathrm{cal}}_8$, not directly to $D^{\mathrm{raw}}_8$.

A statistically significant $D_8$ that does not dominate $D_4$ should be reported separately as a non-specific eighth-order harmonic. It should not be placed in the strong octagonal category solely because $D_8^{\mathrm{cal}}$ is greater than 0.7.

## References


1. Muller, L.; Chavane, F.; Reynolds, J.; et al. Cortical Travelling Waves: Mechanisms and Computational Principles. *Nat. Rev. Neurosci.* **2018**, *19*, 255–268. https://doi.org/10.1038/nrn.2018.20.
2. Haigh, Z.J.; Tran, H.; Berger, T.; et al. Modulation of Motor Excitability Reflects Traveling Waves of Neural Oscillations. *Cell Rep.* **2025**, *44*, 115864. https://doi.org/10.1016/j.celrep.2025.115864.
3. Halgren, M.; Ulbert, I.; Bastuji, H.; et al. The Generation and Propagation of the Human Alpha Rhythm. *Proc. Natl. Acad. Sci.* **2019**, *116*, 23772–23782. https://doi.org/10.1073/pnas.1913092116.
4. Gonzales, D.L.; Khan, H.F.; Keri, H.V.S.; et al. Touch-Evoked Traveling Waves Establish a Translaminar Spacetime Code. *Sci. Adv.* **2025**, *11*, eadr4038. https://doi.org/10.1126/sciadv.adr4038.
5. Bhattacharya, S.; Donoghue, J.A.; Mahnke, M.; et al. Propofol Anesthesia Alters Cortical Traveling Waves. *J. Cogn. Neurosci.* **2022**, *34*, 1274–1286. https://doi.org/10.1162/jocn_a_01856.
6. Cruddas, J.; Pang, J.C.; Fornito, A. Cortical Traveling Waves in Time and Space: Physics, Physiology, and Psychology. *Neuron* **2026**, *114*, 985–1005. https://doi.org/10.1016/j.neuron.2025.12.019.
7. Karuvally, A.; Sejnowski, T.J.; Siegelmann, H.T. Hidden Traveling Waves Bind Working Memory Variables in Recurrent Neural Networks. *arXiv* **2024**, arXiv:2402.10163. https://doi.org/10.48550/arXiv.2402.10163
8. Rubino, D.; Robbins, K.A.; Hatsopoulos, N.G. Propagating Waves Mediate Information Transfer in the Motor Cortex. *Nat. Neurosci.* **2006**, *9*, 1549–1557. https://doi.org/10.1038/nn1802.
9. Takahashi, K.; Saleh, M.; Penn, R.D.; et al. Propagating Waves in Human Motor Cortex. *Front. Hum. Neurosci.* **2011**, *5*, 40. https://doi.org/10.3389/fnhum.2011.00040.
10. Koller, D.P.; Schirner, M.; Ritter, P. Human Connectome Topology Directs Cortical Traveling Waves and Shapes Frequency Gradients. *Nat. Commun.* **2024**, *15*, 3570. https://doi.org/10.1038/s41467-024-47860-x.
11. Buzsáki, G.; Moser, E.I. Memory, Navigation and Theta Rhythm in the Hippocampal-Entorhinal System. *Nat. Neurosci.* **2013**, *16*, 130–138. https://doi.org/10.1038/nn.3304.
12. Hernández-Pérez, J.J.; Cooper, K.W.; Newman, E.L. Medial Entorhinal Cortex Activates in a Traveling Wave in the Rat. *eLife* **2020**, *9*, e52289. https://doi.org/10.7554/elife.52289.
13. Pisarchik, A.N.; Hramov, A.E. Stochastic Processes in the Brain's Neural Network and Their Impact on Perception and Decision-Making. *Uspekhi Fiz. Nauk.* **2023**, *193*, 1298–1324. https://doi.org/10.3367/ufnr.2022.12.039309.
14. Schwenk, J.C.B.; Alamia, A. A Hierarchical Multiscale Model of Forward and Backward Alpha-Band Traveling Waves in the Visual System. *PLOS Comput. Biol.* **2025**, *21*, e1013294. https://doi.org/10.1371/journal.pcbi.1013294.
15. Zhigalov, A.; Jensen, O. Perceptual Echoes as Travelling Waves May Arise from Two Discrete Neuronal Sources. *NeuroImage* **2023**, *272*, 120047. https://doi.org/10.1016/j.neuroimage.2023.120047.
16. Voytek, B.; Knight, R.T. Dynamic Network Communication as a Unifying Neural Basis for Cognition, Development, Aging, and Disease. *Biol. Psychiatry* **2015**, *77*, 1089–1097. https://doi.org/10.1016/j.biopsych.2015.04.016.
17. Lozano-Soldevilla, D.; VanRullen, R. The Hidden Spatial Dimension of Alpha: 10-Hz Perceptual Echoes Propagate as Periodic Traveling Waves in the Human Brain. *Cell Rep.* **2019**, *26*, 374–380.e4. https://doi.org/10.1016/j.celrep.2018.12.058.
18. Zhang, H.; Watrous, A.J.; Patel, A.; et al. Theta and Alpha Oscillations Are Traveling Waves in the Human Neocortex. *Neuron* **2018**, *98*, 1269–1281.e4. https://doi.org/10.1016/j.neuron.2018.05.019.
19. Niedermeyer, E.; Lopes da Silva, F.H., Eds. *Electroencephalography: Basic Principles, Clinical Applications, and Related Fields*, 5th ed.; Lippincott Williams and Wilkins: Philadelphia, PA, USA, 2005.
20. Bhattacharya, S.; Brincat, S.L.; Lundqvist, M.; et al. Traveling Waves in the Prefrontal Cortex during Working Memory. *PLOS Comput. Biol.* **2022**, *18*, e1009827. https://doi.org/10.1371/journal.pcbi.1009827.
21. Tucker, D.M.; Luu, P. Excitatory-Inhibitory Resonance in Cognition Stabilizes Synaptic Traces in Memory. *Cereb. Cortex* **2026**, *36*, bhag044. https://doi.org/10.1093/cercor/bhag044.
22. Griffiths, B.J.; Jensen, O. Gamma Oscillations and Episodic Memory. *Trends Neurosci.* **2023**, *46*, 832–846. https://doi.org/10.1016/j.tins.2023.07.003.
23. Wu, J.; Feng, Z.; Xu, Z.; et al. Oscillatory Network Synergy Across Brain Regions and States Orchestrating Memory Consolidation. *Neuroscience* **2026**, *605*, 39–45. https://doi.org/10.1016/j.neuroscience.2026.03.021.
24. Nimmrich, V.; Draguhn, A.; Axmacher, N. Neuronal Network Oscillations in Neurodegenerative Diseases. *NeuroMolecular Med.* **2015**, *17*, 270–284. https://doi.org/10.1007/s12017-015-8355-9.
25. Stasenko, S.V.; Hramov, A.E.; Kazantsev, V.B. Loss of Neuron Network Coherence Induced by Virus-Infected Astrocytes: A Model Study. *Sci. Rep.* **2023**, *13*, 6401. https://doi.org/10.1038/s41598-023-33622-0.
26. Liu, H.; Yang, Z.; Chen, Y.; et al. Neural Oscillations and Memory: Unraveling the Mechanisms of Anesthesia-Induced Amnesia. *Front. Neurosci.* **2024**, *18*, 1492103. https://doi.org/10.3389/fnins.2024.1492103.
27. Holmes, G.L. Timing Is Everything: The Effect of Early-Life Seizures on Developing Neuronal Circuits Subserving Spatial Memory. *Epilepsia Open* **2025**, 2470-9239. https://doi.org/10.1002/epi4.70023.

28. Gutiérrez-de Pablo, V.; Poza, J.; Maturana-Candelas, A.; et al. Exploring the Disruptions of the Neurophysiological Organization in Alzheimer's Disease: An Integrative Approach. *Comput. Methods Programs Biomed.* **2024**, *250*, 108197. https://doi.org/10.1016/j.cmpb.2024.108197.
29. Höglinger, G.; Trenkwalder, C. Diagnosis and Treatment of Parkinson's Disease (Guideline of the German Society for Neurology). *Neurol. Res. Pract.* **2024**, *6*, 30. https://doi.org/10.1186/s42466-024-00325-4.
30. Jankovic, J.; Tan, E.K. Parkinson's Disease: Etiopathogenesis and Treatment. *J. Neurol. Neurosurg. Psychiatry* **2020**, *91*, 795–808. https://doi.org/10.1136/jnnp-2019-322338.
31. Adam, H.; Gopinath, S.C.B.; Md Arshad, M.K.; et al. An Update on Pathogenesis and Clinical Scenario for Parkinson's Disease: Diagnosis and Treatment. *3 Biotech* **2023**, *13*, 142. https://doi.org/10.1007/s13205-023-03553-8.
32. Bruno, M.K.; Dhall, R.; Duquette, A.; et al. A General Neurologist's Practical Diagnostic Algorithm for Atypical Parkinsonian Disorders. *Neurol. Clin. Pract.* **2024**, *14*, e200345. https://doi.org/10.1212/cpj.0000000000200345. Erratum in *Neurol. Clin. Pract.* **2025**, *15*, e200399. https://doi.org/10.1212/CPJ.0000000000200399.
33. Arya, R.; Haque, A.K.M.A.; Shakya, H.; et al. Parkinson's Disease: Biomarkers for Diagnosis and Disease Progression. *Int. J. Mol. Sci.* **2024**, *25*, 12379. https://doi.org/10.3390/ijms252212379.
34. Höglinger, G.U.; Adler, C.H.; Berg, D.; et al. A Biological Classification of Parkinson's Disease: The SynNeurGe Research Diagnostic Criteria. *Lancet Neurol.* **2024**, *23*, 191–204. https://doi.org/10.1016/s1474-4422(23)00404-0. Erratum in *Lancet Neurol.* **2024**, *23*, e7. https://doi.org/10.1016/S1474–4422(24)00048–6.
35. Serag, I.; Azzam, A.Y.; Hassan, A.K.; et al. Multimodal Diagnostic Tools and Advanced Data Models for Detection of Prodromal Parkinson's Disease: A Scoping Review. *BMC Med. Imaging* **2025**, *25*, 103. https://doi.org/10.1186/s12880-025-01620-5.
36. Mendoza, T.; Pinto-Orellana, M.A.; Olaya, J.E.; et al. Robust Time Delay Estimation for Measurement of Ictal EEG Traveling Waves. *J. Neural Eng.* **2026**, *23*, 056007. https://doi.org/10.1088/1741-2552/ae9bed.
37. Waris, A.; Siraj, M.; Khan, A.; et al. A Comprehensive Overview of the Current Status and Advancements in Various Treatment Strategies against Epilepsy. *ACS Pharmacol. Transl. Sci.* **2024**, *7*, 3729–3757. https://doi.org/10.1021/acsptsci.4c00494.
38. Manole, A.; Sirbu, C.; Mititelu, M.; et al. State of the Art and Challenges in Epilepsy—A Narrative Review. *J. Pers. Med.* **2023**, *13*, 623. https://doi.org/10.3390/jpm13040623.
39. Carapancea, E.; Cilio, M.R. A Novel Approach to Seizures in Neonates. *Eur. J. Paediatr. Neurol.* **2023**, *46*, 89–97. https://doi.org/10.1016/j.ejpn.2023.07.006.
40. Kalyvas, A.C.; Dimitriou, M.; Ioannidis, P.; et al. Alzheimer's Disease and Epilepsy: Exploring Shared Pathways and Promising Biomarkers for Future Treatments. *J. Clin. Med.* **2024**, *13*, 3879. https://doi.org/10.3390/jcm13133879.
41. Ryu, H.U.; Kim, H.J.; Shin, B.S.; et al. Clinical Approaches for Poststroke Seizure: A Review. *Front. Neurol.* **2024**, *15*, 1337960. https://doi.org/10.3389/fneur.2024.1337960.
42. Boleti, A.P.D.A.; Cardoso, P.H.D.O.; Frihling, B.E.F.; et al. Pathophysiology to Risk Factor and Therapeutics to Treatment Strategies on Epilepsy. *Brain Sci.* **2024**, *14*, 71. https://doi.org/10.3390/brainsci14010071.
43. Aiello, G.; Soper, D.J.; Hadar, P.N.; et al. Thalamic Connectivity-Based Biomarkers for Neuromodulation in Patients with Refractory Epilepsies. *medRxiv* **2025**, 2025-02. https://doi.org/10.1101/2025.02.05.25320539.
44. Liou, J.Y.; Smith, E.H.; Bateman, L.M.; et al. A Model for Focal Seizure Onset, Propagation, Evolution, and Progression. *eLife* **2020**, *9*, e50927. https://doi.org/10.7554/elife.50927.
45. Pless, A.; Ware, D.; Saggu, S.; et al. Understanding Neuropsychiatric Symptoms in Alzheimer's Disease: Challenges and Advances in Diagnosis and Treatment. *Front. Neurosci.* **2023**, *17*, 1263771. https://doi.org/10.3389/fnins.2023.1263771.
46. Toader, C.; Dumitru, A.V.; Eva, L.; et al. Nanoparticle Strategies for Treating CNS Disorders: A Comprehensive Review of Drug Delivery and Theranostic Applications. *Int. J. Mol. Sci.* **2024**, *25*, 13302. https://doi.org/10.3390/ijms252413302.
47. Maristany, A.J.; Sa, B.C.; Murray, C.; et al. Psychiatric Manifestations of Neurological Diseases: A Narrative Review. *Cureus* **2024**, *16*, e64152. https://doi.org/10.7759/cureus.64152.
48. Sharma, H.; Chandra, P.; Pathak, R.; et al. Advancements in the Therapeutic Approaches to Treat Neurological Disorders. *Cah. Magellanes-Ns* **2024**, *6*, 4328–4389. https://www.researchgate.net/publication/383399299
49. Sharma, B.; Das, S.; Mazumder, A.; et al. The Role of Neurotransmitter Receptors in Antipsychotic Medication Efficacy for Alzheimer's-Related Psychosis. *Egypt. J. Neurol. Psychiatry Neurosurg.* **2024**, *60*, 75. https://doi.org/10.1186/s41983-024-00848-2.
50. Noor, M.B.T.; Zenia, N.Z.; Kaiser, M.S.; et al. Application of Deep Learning in Detecting Neurological Disorders from Magnetic Resonance Images: A Survey on the Detection of Alzheimer's Disease, Parkinson's Disease and Schizophrenia. *Brain Informatics* **2020**, *7*, 11. https://doi.org/10.1186/s40708-020-00112-2.
51. Cummings, J.; Lanctot, K.; Grossberg, G.; et al. Progress in Pharmacologic Management of Neuropsychiatric Syndromes in Neurodegenerative Disorders. *JAMA Neurol.* **2024**, *81*, 645. https://doi.org/10.1001/jamaneurol.2024.0586.
52. Wang, W.; Ye, J.; Wei, Y.; et al. Clinical Characteristics of Schizophrenia, Depression, and Alzheimer's Diseases among Older Adults: A Retrospective Study of 271 Consecutive Admissions. *Front. Psychiatry* **2025**, *16*, 1486626. https://doi.org/10.3389/fpsyt.2025.1486626.

53. Roberts, J.A.; Gollo, L.L.; Abeysuriya, R.G.; et al. Metastable Brain Waves. *Nat. Commun.* **2019**, *10*, 1056. https://doi.org/10.1038/s41467-019-08999-0.
54. Gu, Y.; Sainburg, L.E.; Kuang, S.; et al. Brain Activity Fluctuations Propagate as Waves Traversing the Cortical Hierarchy. *Cereb. Cortex* **2021**, *31*, 3986–4005. https://doi.org/10.1093/cercor/bhab064.
55. Bergamo, D.; Handjaras, G.; Picchioni, D.; et al. Thalamic Involvement Defines Distinct Slow-Wave Subtypes in NREM Sleep. *Commun. Biol.* **2026**, *9*, 766. https://doi.org/10.1038/s42003-026-09988-y.
56. Pereira, M.; Chen, X.; Paltarzhytskaya, A.; et al. Sleep Neuroimaging: Review and Future Directions. *J. Sleep Res.* **2025**, *34*, e14462. https://doi.org/10.1111/jsr.14462.
57. Ghosh, S., Dallmer-Zerbe, I.;, Buckova, B.R., et al. (2025). Amplitude entropy captures chimera resembling behavior in the altered brain dynamics during seizures. *Scientific Reports*, *15*(1), 14212. https://doi.org/10.1038/s41598-025-97854-y.
58. Atik, A.F. Dual-Metric Energy Analysis of Intracranial EEG: Seizure Onset Zones and Energy-Dominant Regions in Drug-Resistant Epilepsy. *medRxiv* **2026**. https://doi.org/10.64898/2026.05.25.26354017.
59. Schevon, C.A.; Weiss, S.A.; McKhann, G.; et al. Evidence of an Inhibitory Restraint of Seizure Activity in Humans. *Nat. Commun.* **2012**, *3*, 1060. https://doi.org/10.1038/ncomms2056.
60. González, J.; Mateos, D.; Cavelli, M.; et al. Low Frequency Oscillations Drive EEG's Complexity Changes during Wakefulness and Sleep. *Neuroscience* **2022**, *494*, 1–11. https://doi.org/10.1016/j.neuroscience.2022.04.025.
61. Poulet, J.F.A.; Crochet, S. The Cortical States of Wakefulness. *Front. Syst. Neurosci.* **2019**, *12*, 64. https://doi.org/10.3389/fnsys.2018.00064.
62. González, J.; Cavelli, M.; Tort, A.B.L.; et al. Sleep Disrupts Complex Spiking Dynamics in the Neocortex and Hippocampus. *PLOS ONE* **2023**, *18*, e0290146. https://doi.org/10.1371/journal.pone.0290146.
63. Lewis, L.D. The Interconnected Causes and Consequences of Sleep in the Brain. *Science* **2021**, *374*, 564–568. https://doi.org/10.1126/science.abi8375.
64. Sandroni, C.; Cavallaro, F.; Callaway, C.W.; et al. Predictors of Poor Neurological Outcome in Adult Comatose Survivors of Cardiac Arrest: A Systematic Review and Meta-Analysis. Part 2: Patients Treated with Therapeutic Hypothermia. *Resuscitation* **2013**, *84*, 1324–1338. https://doi.org/10.1016/j.resuscitation.2013.06.020.
65. Gong, C.; Jing, C.; Chen, X.; et al. Generative AI for Brain Image Computing and Brain Network Computing: A Review. *Front. Neurosci.* **2023**, *17*, 1203104. https://doi.org/10.3389/fnins.2023.1203104.
66. Ruijter, B.J.; Hofmeijer, J.; Tjepkema-Cloostermans, M.C.; et al. The Prognostic Value of Discontinuous EEG Patterns in Postanoxic Coma. *Clin. Neurophysiol.* **2018**, *129*, 1534–1543. https://doi.org/10.1016/j.clinph.2018.04.745.
67. Shivji, Z.; Bendahan, N.; McInnis, C.; et al. Electroencephalography (EEG) for Neurological Prognostication in Post-Anoxic Coma Following Cardiac Arrest and Its Relationship to Outcome. *Brain Sci.* **2024**, *14*, 1264. https://doi.org/10.3390/brainsci14121264.
68. Rayi, A.; Asuncion, R.M.D.; Mandalaneni, K. Encephalopathic EEG Patterns. In *StatPearls*; StatPearls Publishing: Treasure Island, FL, USA, 2024. https://www.ncbi.nlm.nih.gov/books/NBK564371/.
69. Hodgkin, A.L.; Huxley, A.F. A Quantitative Description of Membrane Current and Its Application to Conduction and Excitation in Nerve. *J. Physiol.* **1952**, *117*, 500–544. https://doi.org/10.1113/jphysiol.1952.sp004764.
70. Morris, C.; Lecar, H. Voltage Oscillations in the Barnacle Giant Muscle Fiber. *Biophys. J.* **1981**, *35*, 193–213. https://doi.org/10.1016/s0006-3495(81)84782-0.
71. Izhikevich, E.M. Which Model to Use for Cortical Spiking Neurons?. *IEEE Trans. Neural Netw.* **2004**, *15*, 1063–1070. https://doi.org/10.1109/tnn.2004.832719.
72. Ibarz, B.; Casado, J.M.; Sanjuán, M.A.F. Map-Based Models in Neuronal Dynamics. *Phys. Rep.* **2011**, *501*, 1–74. https://doi.org/10.1016/j.physrep.2010.12.003.
73. Gu, H.; Pan, B. A Four-Dimensional Neuronal Model to Describe the Complex Nonlinear Dynamics Observed in the Firing Patterns of a Sciatic Nerve Chronic Constriction Injury Model. *Nonlinear Dyn.* **2015**, *81*, 2107–2126. https://doi.org/10.1007/s11071-015-2129-7.
74. Azangue, A.B.; Ngouonkadi, E.B.M.; Nono, M.K.; et al. Collective Behavior in Neuronal Networks with Electrical and Hybrid Synapses: Frequency Responses of Oscillations. *Int. J. Bifurc. Chaos* **2023**, *33*, 2330005. https://doi.org/10.1142/s0218127423300057.
75. Brice Azangue, A.; Megam Ngouonkadi, E.B.; Kabong Nono, M.; et al. Stability and Synchronization in Neural Network with Delayed Synaptic Connections. *Chaos Interdiscip. J. Nonlinear Sci.* **2024**, *34*, 013117. https://doi.org/10.1063/5.0175408.
76. Hansen, M.; Protachevicz, P.R.; Iarosz, K.C.; et al. Dynamics of Uncoupled and Coupled Neurons under an External Pulsed Current. *Chaos Solitons Fractals* **2022**, *155*, 111734. https://doi.org/10.1016/j.chaos.2021.111734.
77. Borges, R.R.; Borges, F.S.; Lameu, E.L.; et al. Effects of the Spike Timing-Dependent Plasticity on the Synchronisation in a Random Hodgkin–Huxley Neuronal Network. *Commun. Nonlinear Sci. Numer. Simul.* **2016**, *34*, 12–22. https://doi.org/10.1016/j.cnsns.2015.10.005.
78. Belykh, I.; Reimbayev, R.; Zhao, K. Synergistic Effect of Repulsive Inhibition in Synchronization of Excitatory Networks. *Phys. Rev. E* **2015**, *91*, 062919. https://doi.org/10.1103/physreve.91.062919.

79. Liu, Z.; Ma, J.; Zhang, G.; et al. Synchronization Control between Two Chua's Circuits via Capacitive Coupling. *Appl. Math. Comput.* **2019**, *360*, 94–106. https://doi.org/10.1016/j.amc.2019.05.004.
80. Megam Ngouonkadi, E.B.; Fotsin, H.B.; Louodop Fotso, P.H. The Combined Effect of Dynamic Chemical and Electrical Synapses in Time-Delay-Induced Phase-Transition to Synchrony in Coupled Bursting Neurons. *Int. J. Bifurc. Chaos* **2014**, *24*, 1450069. https://doi.org/10.1142/s0218127414500692.
81. Azangue, A.B.; Megam Ngouonkadi, E.B.; Fotsin, H.B.; et al. Coherent and Incoherent Control in Neuronal Networks Based on Two Sub-Networks and Biological Implication. *Chaos Solitons Fractals* **2025**, *190*, 115742. https://doi.org/10.1016/j.chaos.2024.115742.
82. Santos, M.S.; Szezech, J.D.; Borges, F.S.; et al. Chimera-like States in a Neuronal Network Model of the Cat Brain. *Chaos Solitons Fractals* **2017**, *101*, 86–91. https://doi.org/10.1016/j.chaos.2017.05.028.
83. Li, X.; Xie, Y.; Ye, Z.; et al. Chimera-like State in the Bistable Excitatory-Inhibitory Cortical Neuronal Network. *Chaos Solitons Fractals* **2024**, *180*, 114549. https://doi.org/10.1016/j.chaos.2024.114549.
84. Zhang, Z.; Dai, L. Effects of Synaptic Pruning on Phase Synchronization in Chimera States of Neural Network. *Appl. Sci.* **2022**, *12*, 1942. https://doi.org/10.3390/app12041942.
85. Omelchenko, I.; Omel'chenko, O.E.; Zakharova, A.; et al. Tweezers for Chimeras in Small Networks. *Phys. Rev. Lett.* **2016**, *116*, 114101. https://doi.org/10.1103/physrevlett.116.114101.
86. Huo, S.; Tian, C.; Zheng, M.; et al. Spatial Multi-Scaled Chimera States of Cerebral Cortex Network and Its Inherent Structure-Dynamics Relationship in Human Brain. *Natl. Sci. Rev.* **2021**, *8*, nwaa125. https://doi.org/10.1093/nsr/nwaa125.
87. Simo, G.R.; Njougouo, T.; Aristides, R.P.; et al. Chimera States in a Neuronal Network under the Action of an Electric Field. *Phys. Rev. E* **2021**, *103*, 062304. https://doi.org/10.1103/physreve.103.062304.
88. Majhi, S.; Perc, M.; Ghosh, D. Chimera States in Uncoupled Neurons Induced by a Multilayer Structure. *Sci. Rep.* **2016**, *6*, 39033. https://doi.org/10.1038/srep39033.
89. Majhi, S.; Perc, M.; Ghosh, D. Chimera States in a Multilayer Network of Coupled and Uncoupled Neurons. *Chaos Interdiscip. J. Nonlinear Sci.* **2017**, *27*, 073109. https://doi.org/10.1063/1.4993836.
90. Majhi, S.; Bera, B.K.; Ghosh, D.; et al. Chimera States in Neuronal Networks: A Review. *Phys. Life Rev.* **2019**, *28*, 100–121. https://doi.org/10.1016/j.plrev.2018.09.003.
91. Kundu, S.; Majhi, S.; Bera, B.K.; et al. Chimera States in Two-Dimensional Networks of Locally Coupled Oscillators. *Phys. Rev. E* **2018**, *97*, 022201. https://doi.org/10.1103/physreve.97.022201.
92. Qin, H.; Wang, C.; Cai, N.; et al. Field Coupling-Induced Pattern Formation in Two-Layer Neuronal Network. *Phys. A Stat. Mech. Appl.* **2018**, *501*, 141–152. https://doi.org/10.1016/j.physa.2018.02.063.
93. Yao, Z.; Wang, C.; Zhou, P.; et al. Regulating Synchronous Patterns in Neurons and Networks via Field Coupling. *Commun. Nonlinear Sci. Numer. Simul.* **2021**, *95*, 105583. https://doi.org/10.1016/j.cnsns.2020.105583.
94. Rostami, Z.; Jafari, S. Defects Formation and Spiral Waves in a Network of Neurons in Presence of Electromagnetic Induction. *Cogn. Neurodyn.* **2018**, *12*, 235–254. https://doi.org/10.1007/s11571-017-9472-y.
95. Parastesh, F.; Rajagopal, K.; Alsaadi, F.E.; et al. Birth and Death of Spiral Waves in a Network of Hindmarsh–Rose Neurons with Exponential Magnetic Flux and Excitable Media. *Appl. Math. Comput.* **2019**, *354*, 377–384. https://doi.org/10.1016/j.amc.2019.02.041.
96. Ma, J.; Tang, J. A Review for Dynamics of Collective Behaviors of Network of Neurons. *Sci. China Technol. Sci.* **2015**, *58*, 2038–2045. https://doi.org/10.1007/s11431-015-5961-6.
97. Xie, Y.; Yao, Z.; Ma, J. Formation of Local Heterogeneity under Energy Collection in Neural Networks. *Sci. China Technol. Sci.* **2023**, *66*, 439–455. https://doi.org/10.1007/s11431-022-2188-2.
98. Xu, Y.; Jin, W.; Ma, J. Emergence and Robustness of Target Waves in a Neuronal Network. *Int. J. Mod. Phys. B* **2015**, *29*, 1550164. https://doi.org/10.1142/s0217979215501647.
99. Lv, M.; Ma, J.; Yao, Y.; et al. Synchronization and Wave Propagation in Neuronal Network under Field Coupling. *Sci. China Technol. Sci.* **2019**, *62*, 448–457. https://doi.org/10.1007/s11431-018-9268-2.
100. Lv, M.; Wang, C.; Ren, G.; et al. Model of Electrical Activity in a Neuron under Magnetic Flow Effect. *Nonlinear Dyn.* **2016**, *85*, 1479–1490. https://doi.org/10.1007/s11071-016-2773-6.
101. Lv, M.; Ma, J. Multiple Modes of Electrical Activities in a New Neuron Model under Electromagnetic Radiation. *Neurocomputing* **2016**, *205*, 375–381. https://doi.org/10.1016/j.neucom.2016.05.004.
102. Xu, F.; Zhang, J.; Jin, M.; et al. Chimera States and Synchronization Behavior in Multilayer Memristive Neural Networks. *Nonlinear Dyn.* **2018**, *94*, 775–783. https://doi.org/10.1007/s11071-018-4393-9.
103. Wu, F.; Ma, J.; Zhang, G. A New Neuron Model under Electromagnetic Field. *Appl. Math. Comput.* **2019**, *347*, 590–599. https://doi.org/10.1016/j.amc.2018.10.087.
104. Shin, M.; Seo, M.; Yoo, S.S.; et al. tFUSFormer: Physics-Guided Super-Resolution Transformer for Simulation of Transcranial Focused Ultrasound Propagation in Brain Stimulation. *IEEE J. Biomed. Health Inform.* **2024**, *28*, 4024–4035. https://doi.org/10.1109/jbhi.2024.3389708.
105. Taş, Y.Ç.; Solaroğlu, İ.; Gürsoy-Özdemir, Y. Spreading Depolarization Waves in Neurological Diseases: A Short Review about Its Pathophysiology and Clinical Relevance. *Curr. Neuropharmacol.* **2019**, *17*, 151–164.

https://doi.org/10.2174/1570159x15666170915160707.

106. Avvenuti, G.; Handjaras, G.; Betta, M.; et al. Integrity of Corpus Callosum Is Essential for the Cross-Hemispheric Propagation of Sleep Slow Waves: A High-Density EEG Study in Split-Brain Patients. *J. Neurosci.* **2020**, *40*, 5589–5603. https://doi.org/10.1523/jneurosci.2571-19.2020.
107. Wouapi, M.K.; Fotsin, B.H.; Ngouonkadi, E.B.M.; et al. Complex Bifurcation Analysis and Synchronization Optimal Control for Hindmarsh–Rose Neuron Model under Magnetic Flow Effect. *Cogn. Neurodyn.* **2021**, *15*, 315–347. https://doi.org/10.1007/s11571-020-09606-5.
108. Zhang, S.; Yao, W.; Xiong, L.; et al. A Hindmarsh–Rose Neuron Model with Electromagnetic Radiation Control for the Mechanical Optimization Design. *Chaos Solitons Fractals* **2024**, *187*, 115408. https://doi.org/10.1016/j.chaos.2024.115408.
109. Bao, H.; Hu, A.; Liu, W.; et al. Hidden Bursting Firings and Bifurcation Mechanisms in Memristive Neuron Model with Threshold Electromagnetic Induction. *IEEE Trans. Neural Netw. Learn. Syst.* **2020**, *31*, 502–511. https://doi.org/10.1109/tnnls.2019.2905137.
110. Takembo, C.N.; Mvogo, A.; Ekobena Fouda, H.P.; et al. Effect of Electromagnetic Radiation on the Dynamics of Spatiotemporal Patterns in Memristor-Based Neuronal Network. *Nonlinear Dyn.* **2019**, *95*, 1067–1078. https://doi.org/10.1007/s11071-018-4616-0.
111. Takembo, C.N.; Mvogo, A.; Fouda, H.P.E.; et al. Wave Pattern Stability of Neurons Coupled by Memristive Electromagnetic Induction. *Nonlinear Dyn.* **2019**, *96*, 1083–1093. https://doi.org/10.1007/s11071-019-04841-w.
112. Palkar, G.; Wu, J.Y.; Ermentrout, B. The Inhibitory Control of Traveling Waves in Cortical Networks. *PLOS Comput. Biol.* **2023**, *19*, e1010697. https://doi.org/10.1371/journal.pcbi.1010697.
113. Wang, Z.; Liu, Z. A Brief Review of Chimera State in Empirical Brain Networks. *Front. Physiol.* **2020**, *11*, 724. https://doi.org/10.3389/fphys.2020.00724.
114. Wu, F.; Wang, C.; Xu, Y.; et al. Model of Electrical Activity in Cardiac Tissue under Electromagnetic Induction. *Sci. Rep.* **2016**, *6*, 28. https://doi.org/10.1038/s41598-016-0031-2.
115. Antal, A.; Herrmann, C.S. Transcranial Alternating Current and Random Noise Stimulation: Possible Mechanisms. *Neural Plast.* **2016**, *2016*, 1–12. https://doi.org/10.1155/2016/3616807.
116. Zhang, W.; Yartsev, M.M. Correlated Neural Activity across the Brains of Socially Interacting Bats. *Cell* **2019**, *178*, 413–428. https://doi.org/10.1016/j.cell.2019.05.023.
117. Wischnewski, M.; Alekseichuk, I.; Opitz, A. Neurocognitive, Physiological, and Biophysical Effects of Transcranial Alternating Current Stimulation. *Trends Cogn. Sci.* **2023**, *27*, 189–205. https://doi.org/10.1016/j.tics.2022.11.013.
118. Izhikevich, E.M. Polychronization: Computation with Spikes. *Neural Comput.* **2006**, *18*, 245–282. https://doi.org/10.1162/089976606775093882.
119. Pauli, R.; Weidel, P.; Kunkel, S.; et al. Reproducing Polychronization: A Guide to Maximizing the Reproducibility of Spiking Network Models. *Front. Neuroinformatics* **2018**, *12*, 46. https://doi.org/10.3389/fninf.2018.00046.
120. Mongillo, G.; Rumpel, S.; Loewenstein, Y. Inhibitory Connectivity Defines the Realm of Excitatory Plasticity. *Nat. Neurosci.* **2018**, *21*, 1463–1470. https://doi.org/10.1038/s41593-018-0226-x. Erratum in *Nat. Neurosci.* **2019**, *22*, 2117. https://doi.org/10.1038/s41593–019–0546–5.
121. Bittner, S.R.; Williamson, R.C.; Snyder, A.C.; et al. Population Activity Structure of Excitatory and Inhibitory Neurons. *PLOS ONE* **2017**, *12*, e0181773. https://doi.org/10.1371/journal.pone.0181773.
122. Xu, J.C.; Fan, J.; Wang, X.; et al. Cultured Networks of Excitatory Projection Neurons and Inhibitory Interneurons for Studying Human Cortical Neurotoxicity. *Sci. Transl. Med.* **2016**, *8*, 333ra48. https://doi.org/10.1126/scitranslmed.aad0623.
123. Ghatak, S.; Talantova, M.; McKercher, S.R.; et al. Novel Therapeutic Approach for Excitatory/Inhibitory Imbalance in Neurodevelopmental and Neurodegenerative Diseases. *Annu. Rev. Pharmacol. Toxicol.* **2021**, *61*, 701–721. https://doi.org/10.1146/annurev-pharmtox-032320-015420.
124. Monteverdi, A.; Palesi, F.; Costa, A.; et al. Subject-Specific Features of Excitation/Inhibition Profiles in Neurodegenerative Diseases. *Front. Aging Neurosci.* **2022**, *14*, 868342. https://doi.org/10.3389/fnagi.2022.868342.
125. Kirischuk, S. Keeping Excitation–Inhibition Ratio in Balance. *Int. J. Mol. Sci.* **2022**, *23*, 5746. https://doi.org/10.3390/ijms23105746.
126. Nelson, S.B.; Valakh, V. Excitatory/Inhibitory Balance and Circuit Homeostasis in Autism Spectrum Disorders. *Neuron* **2015**, *87*, 684–698. https://doi.org/10.1016/j.neuron.2015.07.033.
127. Foliaki, S.T.; Schwarz, B.; Groveman, B.R.; et al. Neuronal Excitatory-to-Inhibitory Balance Is Altered in Cerebral Organoid Models of Genetic Neurological Diseases. *Mol. Brain* **2021**, *14*, 156. https://doi.org/10.1186/s13041-021-00864-w.
128. Uliana, D.L.; Grace, A.A. Prefrontal Cortex Dysfunction as a Precipitating Factor for Schizophrenia and Depression. *J. Neurochem.* **2026**, *170*, e70409. https://doi.org/10.1111/jnc.70409.
129. Sohal, V.S.; Rubenstein, J.L.R. Excitation-Inhibition Balance as a Framework for Investigating Mechanisms in Neuropsychiatric Disorders. *Mol. Psychiatry* **2019**, *24*, 1248–1257. https://doi.org/10.1038/s41380-019-0426-0.
130. Sears, S.M.S.; Hewett, S.J. Influence of Glutamate and GABA Transport on Brain Excitatory/Inhibitory Balance. *Exp. Biol. Med.* **2021**, *246*, 1069–1083. https://doi.org/10.1177/1535370221989263.
131. Wu, F.; Hu, X.; Ma, J. Estimation of the Effect of Magnetic Field on a Memristive Neuron. *Appl. Math. Comput.* **2022**,

*432*, 127366. https://doi.org/10.1016/j.amc.2022.127366.

132. Guo, Y.; Xie, Y.; Ma, J. Nonlinear Responses in a Neural Network under Spatial Electromagnetic Radiation. *Phys. A Stat. Mech. Appl.* **2023**, *626*, 129120. https://doi.org/10.1016/j.physa.2023.129120.
133. Pajevic, S.; Basser, P.J.; Fields, R.D. Role of Myelin Plasticity in Oscillations and Synchrony of Neuronal Activity. *Neuroscience* **2014**, *276*, 135–147. https://doi.org/10.1016/j.neuroscience.2013.11.007.
134. Sun, B.; Wang, Y.; Ye, Q.; et al. Associations of Empathy with Teacher–Student Interactions: A Potential Ternary Model. *Brain Sci.* **2023**, *13*, 767. https://doi.org/10.3390/brainsci13050767.
135. Vuust, P.; Heggli, O.A.; Friston, K.J.; et al. Music in the Brain. *Nat. Rev. Neurosci.* **2022**, *23*, 287–305. https://doi.org/10.1038/s41583-022-00578-5.
136. Marek, S.; Dosenbach, N.U.F. The Frontoparietal Network: Function, Electrophysiology, and Importance of Individual Precision Mapping. *Dialogues Clin. Neurosci.* **2018**, *20*, 133–140. https://doi.org/10.31887/dcns.2018.20.2/smarek.
137. Bohle, H.; Rimpel, J.; Schauenburg, G.; et al. Behavioral and Neural Correlates of Cognitive-Motor Interference during Multitasking in Young and Old Adults. *Neural Plast.* **2019**, *2019*, 9478656. https://doi.org/10.1155/2019/9478656.
138. Ingendoh, R.M.; Posny, E.S.; Heine, A. Binaural Beats to Entrain the Brain? a Systematic Review of the Effects of Binaural Beat Stimulation on Brain Oscillatory Activity, and the Implications for Psychological Research and Intervention. *PLOS ONE* **2023**, *18*, e0286023. https://doi.org/10.1371/journal.pone.0286023.
139. Ceravolo, L.; Stiennon, E.; Constantin, I.; et al. Attentional Focus and Emotion Modulate Voice Recognition Deficits in Cerebellar Stroke Patients. *bioRxiv* **2025**. https://doi.org/10.64898/2025.12.08.692937.
140. Elnazer, H.Y. Music and Binaural Beat Interventions for Young Adults: A Systematic Review of Effects on Anxiety, Sleep, and Cognition. *Acta Neuropsychiatr.* **2026**, *38*, e15. https://doi.org/10.1017/neu.2026.10057.
141. Mujib, M.D.; Rao, A.Z.; Qazi, S.A.; et al. Binaural Beat Stimulation for Cognitive and Psychological Enhancement in Alzheimer's Disease: A Pilot Study. *IEEE Trans. Neural Syst. Rehabil. Eng.* **2026**, *34*, 1974–1986. https://doi.org/10.1109/tnsre.2026.3679482.
142. Alhasani, R.; Almutairi, L.; Alshahrani, R.; et al. The Effects of 40 Hz Gamma Binaural Beat Auditory Stimulation on Postural Control, Motor Coordination, and Cognitive Function among Healthy Adults: A Pilot Study. *J. Clin. Med.* **2026**, *15*, 7041. https://doi.org/10.3390/jcm15187041.
143. Bazanova, O.M.; Zakharov, A.; Ozonov, E.; et al. Alpha-EEG/EMG Neurofeedback Combined with Binaural Beats Stimulation: A Randomized Placebo-Controlled within-Subject Cross over Study. *Int. J. Psychophysiol.* **2026**, *222*, 113337. https://doi.org/10.1016/j.ijpsycho.2026.113337.
144. Sangtarash, N.; Bigdeli, M.R.; Fathabadi, J.; et al. The Effect of Binaural Beats on Phonological Awareness and Cortical Connectivity in Dyslexic Children. *Sci. Rep.* **2026**, *16*, 25761. https://doi.org/10.1038/s41598-026-56452-2.
145. Wang, J.; Qu, S.; Zhou, Y.; et al. Cortical Processing Modulation in DOC by Preferred Music-Coupled 40 Hz Binaural Stimulation: An Exploratory EEG-fNIRS Study. *Front. Psychol.* **2026**, *17*, 1783416. https://doi.org/10.3389/fpsyg.2026.1783416.
146. Fatima, I.; Zaidi, S.; Sundus, H.; et al. Efficacy of Theta Binaural Beat Therapy on Pain, Cognition and Anxiety in Adults: A Systematic Review and Meta-Analysis of Randomized Controlled Trials. *EXPLORE* **2026**, *22*, 103471. https://doi.org/10.1016/j.explore.2026.103471.
147. Lang, N.; Siebner, H.R.; Ward, N.S.; et al. How Does Transcranial DC Stimulation of the Primary Motor Cortex Alter Regional Neuronal Activity in the Human Brain?. *Eur. J. Neurosci.* **2005**, *22*, 495–504. https://doi.org/10.1111/j.1460-9568.2005.04233.x.
148. Stein, B.E.; Stanford, T.R. Multisensory Integration: Current Issues from the Perspective of the Single Neuron. *Nat. Rev. Neurosci.* **2008**, *9*, 255–266. https://doi.org/10.1038/nrn2331. Erratum in *Nat. Rev. Neurosci.* **2008**, *9*, 406. https://doi.org/10.1038/nrn2377.
149. Downing, P.E.; Chan, A.W.Y.; Peelen, M.V.; et al. Domain Specificity in Visual Cortex. *Cereb. Cortex* **2006**, *16*, 1453–1461. https://doi.org/10.1093/cercor/bhj086.
150. Blanchette, I.; Richards, A. The Influence of Affect on Higher Level Cognition: A Review of Research on Interpretation, Judgement, Decision Making and Reasoning. *Cogn. Emot.* **2010**, *24*, 561–595. https://doi.org/10.1080/02699930903132496.
151. Gain, U. The Cognitive Function and the Framework of the Functional Hierarchy. *Appl. Comput. Informatics* **2018**, *16*, 81–116. https://doi.org/10.1016/j.aci.2018.03.003.
152. Evans, J.S.B.T. Dual-Process Theories of Reasoning: Contemporary Issues and Developmental Applications. *Dev. Rev.* **2011**, *31*, 86–102. https://doi.org/10.1016/j.dr.2011.07.007.
153. Killgore, W.D.S. Effects of Sleep Deprivation on Cognition. *Prog. Brain Res.* **2010**, *185*, 105–129. https://doi.org/10.1016/b978-0-444-53702-7.00007-5.
154. Nadirova, Z. Development of Intuition in Brain Activity. *ACTA NUUz* **2024**, *1*, 114–117. https://doi.org/10.69617/uzmu.v1i1.1.374.
155. Zall, R.; Kangavari, M.R. Comparative Analytical Survey on Cognitive Agents with Emotional Intelligence. *Cogn. Comput.* **2022**, *14*, 1223–1246. https://doi.org/10.1007/s12559-022-10007-5.
156. Thuc, T.D.; Van Pham, T. The Relationship between Thinking Ability, Emotional Intelligence and Decision-Making.

*Emerg. Sci. J.* **2024**, *8*, 644–657. https://doi.org/10.28991/esj-2024-08-02-017.
157. Mitsea, E.; Drigas, A.; Skianis, C. ICTs and Speed Learning in Special Education: High-Consciousness Training Strategies for High-Capacity Learners through Metacognition Lens. *Tech. Soc. Sci. J.* **2022**, *27*, 230–252. https://doi.org/10.47577/tssj.v27i1.5599.
158. Faglioni, P. The Frontal Lobe. In *Handbook of Clinical and Experimental Neuropsychology*; Psychology Press: London, UK, 2020; pp. 525–570. https://doi.org/10.4324/9781315791272-31.
159. Rizzolatti, G.; Sinigaglia, C. The Functional Role of the Parieto-Frontal Mirror Circuit: Interpretations and Misinterpretations. *Nat. Rev. Neurosci.* **2010**, *11*, 264–274. https://doi.org/10.1038/nrn2805.
160. Schall, J.D. Visuomotor Functions in the Frontal Lobe. *Annu. Rev. Vis. Sci.* **2015**, *1*, 469–498. https://doi.org/10.1146/annurev-vision-082114-035317.
161. Battaglia-Mayer, A.; Buiatti, T.; Caminiti, R.; et al. Correction and Suppression of Reaching Movements in the Cerebral Cortex: Physiological and Neuropsychological Aspects. *Neurosci. Biobehav. Rev.* **2014**, *42*, 232–251. https://doi.org/10.1016/j.neubiorev.2014.03.002.
162. Subramanian, D.; Alers, A.; Sommer, M.A. Corollary Discharge for Action and Cognition. *Biol. Psychiatry Cogn. Neurosci. Neuroimaging* **2019**, *4*, 782–790. https://doi.org/10.1016/j.bpsc.2019.05.010.
163. Haggard, P. Sense of Agency in the Human Brain. *Nat. Rev. Neurosci.* **2017**, *18*, 196–207. https://doi.org/10.1038/nrn.2017.14.
164. Pilgramm, S.; de Haas, B.; Helm, F.; et al. Motor Imagery of Hand Actions: Decoding the Content of Motor Imagery from Brain Activity in Frontal and Parietal Motor Areas. *Hum. Brain Mapp.* **2016**, *37*, 81–93. https://doi.org/10.1002/hbm.23015.
165. Parastesh, F.; Azarnoush, H.; Jafari, S.; et al. Synchronizability of Two Neurons with Switching in the Coupling. *Appl. Math. Comput.* **2019**, *350*, 217–223. https://doi.org/10.1016/j.amc.2019.01.011.
166. Mazeaud, C.; Salazar, B.H.; Braun, M.; et al. Functional MRI in Neuro-Urology: A Narrative Review. *Prog. Urol.* **2023**, *33*, 349–356. https://doi.org/10.1016/j.purol.2023.03.002.
167. Di Giovanni, D.A. Deep Learning and Statistical Methods for Clinical Application of Functional Magnetic Resonance Imaging. Ph.D. Thesis, McGill University, Montreal, QC, Canada, 2024.
168. Comby, P.A. From Compressed Sensing to Deep Learning Based Methods for Functional Magnetic Resonance Imaging Reconstruction at Ultra-High Field. Ph.D. Thesis, Université Paris-Saclay, Orsay, France, 2025.
169. Peyvandi, S.; Rollins, C. Fetal Brain Development in Congenital Heart Disease. *Can. J. Cardiol.* **2023**, *39*, 115–122. https://doi.org/10.1016/j.cjca.2022.09.020.
170. Calhoun, V. Data-Driven Approaches for Identifying Links between Brain Structure and Function in Health and Disease. *Dialogues Clin. Neurosci.* **2018**, *20*, 87–99. https://doi.org/10.31887/dcns.2018.20.2/vcalhoun.
171. Fayed, N.; Morales, H.; Fayed, A. Brain Imaging: From Ramón y Cajal Epoch to Our Days. In *Psychiatry and Neuroscience Update – Vol. V*; Springer: Cham, Switzerland, 2024; pp. 531–540. https://doi.org/10.1007/978-3-031-72219-6_43.
172. Belin, P.; Zatorre, R.J.; Ahad, P. Human Temporal-Lobe Response to Vocal Sounds. *Cogn. Brain Res.* **2002**, *13*, 17–26. https://doi.org/10.1016/s0926-6410(01)00084-2.
173. Lavallee, C.F.; Koren, S.A.; Persinger, M.A. A Quantitative Electroencephalographic Study of Meditation and Binaural Beat Entrainment. *J. Altern. Complement. Med.* **2011**, *17*, 351–355. https://doi.org/10.1089/acm.2009.0691.
174. Wahbeh, H.; Calabrese, C.; Zwickey, H.; et al. Binaural Beat Technology in Humans: A Pilot Study to Assess Neuropsychologic, Physiologic, and Electroencephalographic Effects. *J. Altern. Complement. Med.* **2007**, *13*, 199–206. https://doi.org/10.1089/acm.2006.6201.
175. Askarpour, H.; Mirzaee, F.; Habibi, F.; et al. Binaural Beats' Effect on Brain Activity and Psychiatric Disorders: A Literature Review. *Open Public Health J.* **2024**, *17*, e18749445332258. https://doi.org/10.2174/0118749445332258241008103504.
176. Friston, K.J.; Bastos, A.M.; Oswal, A.; et al. Granger Causality Revisited. *NeuroImage* **2014**, *101*, 796–808. https://doi.org/10.1016/j.neuroimage.2014.06.062.
177. Wibral, M.; Vicente, R.; Lindner, M. Transfer Entropy in Neuroscience. In *Directed Information Measures in Neuroscience*; Springer: Berlin/Heidelberg, Germany, 2014; pp. 3–36. https://doi.org/10.1007/978-3-642-54474-3_1.
178. Seth, A.K.; Barrett, A.B.; Barnett, L. Granger Causality Analysis in Neuroscience and Neuroimaging. *J. Neurosci.* **2015**, *35*, 3293–3297. https://doi.org/10.1523/jneurosci.4399-14.2015.
179. Lubenov, E.V.; Siapas, A.G. Hippocampal Theta Oscillations Are Travelling Waves. *Nature* **2009**, *459*, 534–539. https://doi.org/10.1038/nature08010.
180. Patel, J.; Fujisawa, S.; Berényi, A.; et al. Traveling Theta Waves Along the Entire Septotemporal Axis of the Hippocampus. *Neuron* **2012**, *75*, 410–417. https://doi.org/10.1016/j.neuron.2012.07.015.
181. Zhang, H.; Jacobs, J. Traveling Theta Waves in the Human Hippocampus. *J. Neurosci.* **2015**, *35*, 12477–12487. https://doi.org/10.1523/jneurosci.5102-14.2015.
182. Kuramoto, Y. Self-Entrainment of a Population of Coupled Non-Linear Oscillators. In *International Symposium on Mathematical Problems in Theoretical Physics*; Springer: Berlin/Heidelberg, Germany, 1975; pp. 420–422. https://doi.org/10.1007/bfb0013365.
183. Strogatz, S.H. From Kuramoto to Crawford: Exploring the Onset of Synchronization in Populations of Coupled Oscillators.

*Phys. D Nonlinear Phenom.* **2000**, *143*, 1–20. https://doi.org/10.1016/s0167-2789(00)00094-4.

184. Acebrón, J.A.; Bonilla, L.L.; Pérez Vicente, C.J.; et al. The Kuramoto Model: A Simple Paradigm for Synchronization Phenomena. *Rev. Mod. Phys.* **2005**, *77*, 137–185. https://doi.org/10.1103/revmodphys.77.137.
185. Rodrigues, F.A.; Peron, T.K.D.M.; Ji, P.; et al. The Kuramoto Model in Complex Networks. *Phys. Rep.* **2016**, *610*, 1–98. https://doi.org/10.1016/j.physrep.2015.10.008.
186. Ma, J.; Wu, Y.; Ying, H.; et al. Channel Noise-Induced Phase Transition of Spiral Wave in Networks of Hodgkin-Huxley Neurons. *Chin. Sci. Bull.* **2011**, *56*, 151–157. https://doi.org/10.1007/s11434-010-4281-2.
187. Ma, J.; Huang, L.; Tang, J.; et al. Spiral Wave Death, Breakup Induced by Ion Channel Poisoning on Regular Hodgkin–Huxley Neuronal Networks. *Commun. Nonlinear Sci. Numer. Simul.* **2012**, *17*, 4281–4293. https://doi.org/10.1016/j.cnsns.2012.03.009.
188. Liu, S.B.; Wu, Y.; Li, J.J.; et al. The Dynamic Behavior of Spiral Waves in Stochastic Hodgkin–Huxley Neuronal Networks with Ion Channel Blocks. *Nonlinear Dyn.* **2013**, *73*, 1055–1063. https://doi.org/10.1007/s11071-013-0852-5.
189. Yao, Y.; Deng, H.; Ma, C.; et al. Impact of Bounded Noise and Rewiring on the Formation and Instability of Spiral Waves in a Small-World Network of Hodgkin-Huxley Neurons. *PLOS ONE* **2017**, *12*, e0171273. https://doi.org/10.1371/journal.pone.0171273.
190. Deco, G.; Jirsa, V.K.; Robinson, P.A.; et al. The Dynamic Brain: From Spiking Neurons to Neural Masses and Cortical Fields. *PLoS Comput. Biol.* **2008**, *4*, e1000092. https://doi.org/10.1371/journal.pcbi.1000092.
191. Lachaux, J.P.; Rodriguez, E.; Martinerie, J.; et al. Measuring Phase Synchrony in Brain Signals. *Hum. Brain Mapp.* **1999**, *8*, 194–208. https://doi.org/10.1002/(SICI)1097-0193(1999)8:4¡194::AID-HBM4¿3.0.CO;2-C.
192. Mormann, F.; Lehnertz, K.; David, P.; et al. Mean Phase Coherence as a Measure for Phase Synchronization and Its Application to the EEG of Epilepsy Patients. *Phys. D Nonlinear Phenom.* **2000**, *144*, 358–369. https://doi.org/10.1016/s0167-2789(00)00087-7.
193. Tallon-Baudry, C.; Bertrand, O.; Peronnet, F.; et al. Induced $\gamma$-Band Activity during the Delay of a Visual Short-Term Memory Task in Humans. *J. Neurosci.* **1998**, *18*, 4244–4254. https://doi.org/10.1523/jneurosci.18-11-04244.1998.
194. Wautier, A.; Guzina, B.B. On the Second-Order Homogenization of Wave Motion in Periodic Media and the Sound of a Chessboard. *J. Mech. Phys. Solids* **2015**, *78*, 382–414. https://doi.org/10.1016/j.jmps.2015.03.001.